

PhD in
Physics and Astronomy

CYCLE XXXV

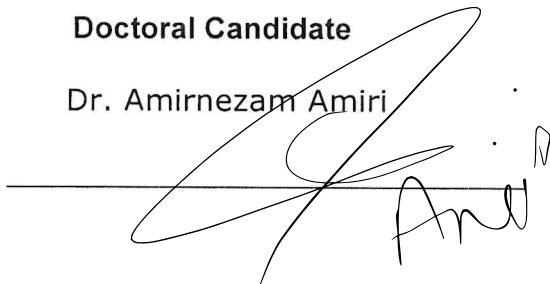
COORDINATOR Prof. Giovanni Modugno

**A new approach to photoionization modelling
and
the physical conditions of HII regions and Star Forming Galaxies**

Academic Discipline (SSD) FIS/05

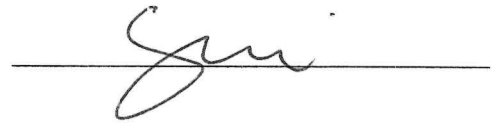
Doctoral Candidate

Dr. Amirnezam Amiri

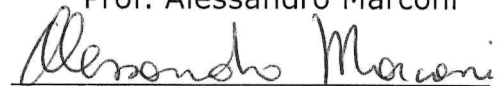
A handwritten signature in black ink, appearing to read 'Amiri', written over a horizontal line.

Supervisors

Dr. Giovanni Cresci

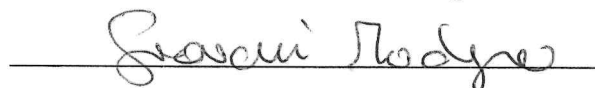
A handwritten signature in black ink, appearing to read 'Giacca', written over a horizontal line.

Prof. Alessandro Marconi

A handwritten signature in black ink, appearing to read 'Alessandro Marconi', written over a horizontal line.

Coordinator

Prof. Giovanni Modugno

A handwritten signature in black ink, appearing to read 'Giacca Modugno', written over a horizontal line.

Years 2019/2022

*Dedicated to
The Nature*

4

Everything that is made beautiful and fair and lovely is made for the eye of one who sees.

Rumi (A 13th-century Persian poet)

Declaration

5

I hereby state no previous dissertation I have submitted for a degree, diploma, or other qualification at any other university considerably resembles this one. I also state that parts of my thesis has already been, or is being simultaneously submitted, for scientific journals, in the below:

1. AZAR: A new approach to photoionization modelling I : towards percent accuracy in reproducing observed emission lines and the physical properties of the ionised medium; A.Marconi, A.Amiri et al (submitted to A&A-2023)

2. AZAR: A new approach to photoionization modelling II : A new, multi-cloud method to accurately model emission lines in starforming galaxies A.Amiri, A.Marconi et al (submitted to A&A-2023)

Metallicity is one of the most prominent physical quantities in the study of galaxy evolution and specifically of star forming regions. There are two main methods to determine gas phase metallicity: empirical and theoretical approaches.

The empirical method measures abundances using the information directly inferred from the emission lines in spectra. There are different ways to determine metallicity in the framework of the empirical method. The most commonly used one, called direct method, includes measurement of temperature-sensitive line ratios such as $[\text{OIII}]\lambda 4363/5007$, $[\text{NII}]\lambda 5755/6584$, and $[\text{SII}]\lambda 6312/9532$. The lines at the numerator of the ratio are called auroral lines, and are used to directly measure the electron temperature (T_e) of the nebular gas. However, when these weak auroral lines are not available, a method involving the ratios of strong emission lines must instead be used as an indirect metallicity indicator. In this case, the strong line ratios are calibrated against metallicity using direct measurements or theoretical models.

The theoretical method uses multi-parametric photoionization models to reproduce the observed emission lines. These photoionisation codes are useful tools commonly used by the astronomical community to model the properties of gas irradiated by an ionizing source (e.g., in planetary nebulae, HII regions, and AGNs), which take into account the different spectral components involved. These codes solve numerically the ionization and thermal structures of an ionized cloud and output the nebular continuum and emission line spectra. Over the past decades, a wide range of studies has been developed to establish computational models of single-component ionized gas to reproduce the emission lines in galaxies. Single-zone models reproduce the ionization, caused by a continuum source, of a single, ionization-bounded, gas cloud of hydrogen with number density N_H . The investigations that utilize a single cloud to analyse the expected spectral changes with variations in gas abundances or spectral energy distribution (SED) may derive misleading results.

In this thesis, we will use a novel approach, where we treat the spectrum emerging from a galaxy or an HII region not as the product of a single emitting gas cloud, but as a combination of the emission of multiple clouds with different properties such as density and ionisation. In this way, it is possible to significantly improve the agreement between observations and simulated data. The spectrum predicted by these models depends on global integration, over gas density at a specific location, and over radius. Results depend weakly on the density distribution and they slightly depend on the radial distribution. This is in contrast to single-cloud models, which often are described by an ionization parameter and whose predicted spectrum has a strong dependence on this parameter. The locally optimally emitting clouds model (where locally means that each line could be formed efficiently only at a specific location in the density–flux plane and optimally that we consider only emission from a cloud with an optimal flux and density for each line) fit the observed spectrum with fewer free parameters than do single-cloud models. The locally optimally emitting clouds approach is a more physical model because, unless galaxy clouds have a remarkably restricted range of properties, we will observe the a variety of emitting clouds for most lines. The emission line spectrum from clouds distributed in gas density and radius is much less sensitive to changes in the gas abundances and SED than that emitted by a single cloud.

Single cloud model-based studies have tried to use a wide range of physical parameters to reproduce complex emission lines observed in galaxies but they were not fully successful. In comparison with observations, single-based models predict too weak high ionization lines and too low predicted electronic temperature, which can generally infer from line ratio

$[\text{OIII}]\lambda 4363/[\text{OIII}]\lambda 5007$.

In this thesis, we develop a new, more realistic approach based on the use of multiple components of photoionised gas to reproduce all observable emission lines simultaneously. To improve the agreement between the models predictions and the observations, we consider the fact that a star-forming galaxy is a collection of HII regions (or a HII region is a combination of different properties from different scales inside it). These regions have a wide range of properties. The galaxy's emission lines are a combination of the emission of all these different regions. The model uses a set of the different gas clouds with different properties and combine them to reproduce all observed emission lines for one system.

The organization of this thesis is as follows. In chapter1, we focus on gas-phase metallicity as a key parameter to determine the evolution of Gas in star-forming galaxy and HII regions. Also, we introduce both empirical and theoretical approaches to measure chemical properties of galaxies. In chapter2, we provide explanations of model spectra based on photoionisation simulations with CLOUDY.

In chapter3, we describe a new novel, multi-cloud method, to model accurately the chemical properties of galaxies. We discuss how previous studies in the last 20-years tried to use a wide range of physical parameters to reproduce complex emission lines observed in HII regions and star-forming galaxies but all attempts have not been successful so far to comprehensively predict all observable emission lines and gas-phase metallicity. We tested our method using different samples of HII regions with high quality line flux measurements.

In chapter4, we present the reference sample we used to test the method on star forming galaxy spectra. This sample is based on SDSS stacked galaxy spectra, in order to detect faint emission lines, such as auroral line, that are not generally observable at high S/N in single galaxies.

In chapter5 to show the performance of our new method, we demonstrate how our novel multiple clouds approach can reproduce the observed line fluxes on multiple species and ionisation states with an accuracy better than 10%. Moreover, we re-calibrate the new strong calibration relationship according to the new multi-cloud model, we present the relation between ionisation and metallicity, nitrogen and sulfur abundances, the relation between temperatures in different low and high ionisation parts. Additionally, we show which is the impact of excluding T_e sensitive line ratios from the inputs of the model, especially at high metallicity

Finally, in section 6, we summarize our main results and discuss some future applications to investigate them by using our new method.

Acknowledgments

The greatest thanks to My mother, my aunts, and my grandmother-the people who were giving me their unwavering love, support, and encouragement.

I am deeply and truly indebted to so many people that there is no way to acknowledge them all, or even any of them properly. This thesis would not be possible without the active supervision and endless supports of my advisors Alessandro Marconi and Giovanni Cresci who have taught me a lot during these years. This thesis is indeed a result of infinite loops of interactions with them, my failures and mistakes, and successful moments.

I am deeply grateful to Filippo Mannucci, who played a decisive role in my understanding and growing during these years. The lessons he taught me have influenced a lot on my research strategies. A large part of what is written in this thesis would have never been there without his guidance and assistance.

I would like to express my deepest appreciation to Francesco Belfiore, who always supported and nurtured me with his helpful advice and kind guidance to find answers and understand them, deeply. For challenging me to develop my own view, for his willingness to share his knowledge and experiences with me in each scientific step. For his always positive and encouraging attitude in difficult times.

I am infinitely thankful to Mirko Curti for teaching me how to deal with auroral lines, metallicity and high redshift galaxies, for his fruitful discussions and valuable advice during this time and including me in his researches.

I also had great pleasure of discussing with Roberto Maiolino, Abraham Loeb, Johan Knappen, Rien Weigaert, Giafranco De Zotti, Giacomo Venturi, Neven Tomicic, Matilde Mingozi, Alice Concas, Habib Khosroshahi, Saeed Tavasoli, Shahram Khosravi, Tahere Pourmirjafari and I would like to thank them for their ideas and discussions.

My cousin, Mahdi, who challenged me to understand society's physics. Thanks to my best friend Khakpoor to help me pass over rainy days and Khoram for fruitful scientific discussion.

My lovely friends in Florence, Seyma, Giulia, George, Maria, Layal, Stefano, Lucy, Essna, Cosimo, Lorenzo, and Martina, for being this much amazing, supportive, and kind to me. I would like to extend my sincere thanks to San Marco's family, for their kindness, support, and love.

Last but not least, I am particularly grateful to my cosmology circle friends. Exactly, we started to study galaxy formation and evolution, since 10 years ago.

Contents

1	Introduction	1
1.1	Galaxy formation and evolution	1
1.2	Baryonic cycle	4
1.3	Stellar nucleosynthesis	5
1.4	Interstellar Medium (ISM) and starforming galaxies	9
1.4.1	HII regions and starforming galaxies	9
1.5	Ionisation properties	11
1.6	Dust	12
1.7	Metallicity in galaxy evolution	14
1.7.1	Empirical method	18
1.7.2	Theoretical method	21
2	Photoionisation simulations	23
2.1	CLOUDY	23
2.1.1	Assumptions	25
2.1.2	Example of Model creation	29
3	A new multiple cloud approach to determine metallicity	31
3.1	Single cloud models	32
3.2	New multiple cloud models	33
3.2.1	An example of a model fit	36
3.2.2	Comparison with constant-pressure single-cloud models	39
3.2.3	The sample by of HII regions by Zurita et al.	40
3.2.4	The sample by Berg et al.	44
3.2.5	Gas and stellar metallicities in the Milky Way	46
4	Observation and flux measurements	49
4.1	The Sloan Digital Sky Survey	49
4.2	Sample Selection	49
4.2.1	Stacked galaxies	50
4.2.2	Single galaxies	52
4.3	Stellar Continuum Subtraction and Line Flux Measurement	53
5	Multi-cloud application on starforming galaxies	69
5.1	A new, multi-cloud method to accurately model emission lines in starforming galaxies	69
5.1.1	Flux comparisons	71

5.1.2	Electron Temperatures and Density	71
5.1.3	Ionic Abundances Determination	73
5.1.4	Calibrations of strong-line metallicity indicators	75
5.1.5	Ionisation properties	77
5.1.6	Model Metallicity deviation from T_e	80
5.1.7	Lacking of Auroral lines on model constrain	82
6	Summary and Conclusions	85
6.1	Future developments	87
6.1.1	T_e metallicities and calibration of the strong-line method at high redshift	87
6.1.2	Active Galactic Nuclei	87

Chapter 1

Introduction

In this chapter, I describe the essential astrophysical structures which lead us to understand galaxy evolution. We will focus on HII regions and star-forming galaxies and we will show how stellar evolution can provide heavy elements. We will focus on the physical conditions of the gas in this complex environments and show how metallicity and gas physical properties help us to understand fundamentals of galaxy evolution.

1.1 Galaxy formation and evolution

In currently popular cosmologies we usually consider a Universe consisting of three main components. In addition to the baryonic matter, the protons, neutrons and electrons that build up the observable Universe, astronomers have found various indications for the presence of dark matter and dark energy. Although the nature of both dark matter and dark energy is not fully understood, we believe that they are responsible for more than 95 percent of the energy density of the Universe. The most popular model is the Λ CDM model, a flat Universe in which ~ 75 percent of the energy density is due to a cosmological constant, ~ 21 percent is due to cold dark matter (CDM), and $\sim 4\%$ is the baryonic matter which stars and galaxies are made from.

Initial Conditions

According to the standard model of cosmology, if the distribution of matter in the Universe were completely uniform and homogeneous, we would not expect to see any kind of structure and it would not be possible to explain observed structures. In order to explain the presence of structures, in particular galaxies, we need deviations from complete homogeneity.

In very early Universe, when it is extremely dense and quantum effects should be considered, classical and general relativistic interpretation of cosmology face very difficult challenges. The standard cosmology has a number of serious problems when applied to the early Universe. To solve these problems, we need an extension of the standard cosmology, namely beyond standard cosmology, which involves quantum processes. One general consequence of such an extension is the generation of density perturbations by quantum fluctuations at very early times. It is believed that these perturbations are responsible for the formation of the structures observed in our Universe.

Inflation is a popular extension to Λ CDM which posits that the Universe went through a

phase of rapid, exponential expansion driven by the vacuum energy of quantum fields. In most inflationary theories, quantum fluctuations in this vacuum energy can produce density perturbations which could be the origin of the observed large-scale structure. Inflation thus suggests a good explanation for the origin of the initial perturbations. Our knowledge of the very early Universe however is far from complete, and it is unable to predict the initial conditions for structure formation entirely from first principles. Technically, initial conditions are specified by a set of parameters that are constrained by observations, such as the pattern of fluctuations in the microwave background or the present-day abundance of galaxy clusters.

Gravity and Structure Formation

The Universe exhibits tiny density fluctuations from homogeneity that were seeded during inflation at extremely early times ($t \sim 10^{-36} - 10^{-32}$ s). Following the growth in the radiation dominated era, during the early phase of the matter dominated era and prior to gravity overriding cosmic expansion in the densest areas, where dark matter collapses into self-gravitating halos, the density contrast grows linearly with the cosmic scale factor. In this instance, dark matter halo centers are where galaxies develop. The power spectrum of the primordial density fluctuations entirely determines the mass distribution and spatial correlation of dark matter halos, which are represented by the halo mass functions and correlation functions.

Cooling

A key component of galaxy evolution is the physics of cooling. As dark matter collapses, gas accretes onto the halo and is heated by accretion shocks to the halo virial temperature. Before falling towards the center of the halo and becoming stars, the gas must cool. The bremsstrahlung (free-free, $> 10^6$ K), metal-line cooling ($10^5 - 10^6$ K), atomic cooling (H and He, 10^4 to 10^5 K), fine-structure lines ([CII] and [OI]), molecular, and dust cooling ($< 10^4$ K) are some of the most significant cooling mechanisms. There are also other physical processes involved related to heating, including Compton heating, photoionization and photoelectric heating, cosmic ray heating, and shocks (such as supernova ejection, outflows, accretion shocks). These processes lead to the circumgalactic medium (CGM) multi-phase nature, where hot ionized gas, warm neutral gas, and cold molecular gas coexist in equilibrium state. In regions with higher densities, cooling is typically more effective. The shocked gas in virialized halos may be sufficiently dense after nonlinearity in gravitational collapse for cooling to take place. The gas does not reach hydrostatic equilibrium if cooling times are short enough; instead, it accretes directly onto the core protogalaxy. The denser inner parts of the atmosphere may nevertheless lose pressure support and flow towards the central object even if cooling is slow enough for a hydrostatic atmosphere to form. Cooling has the overall result of separating baryonic matter from dark matter, which then builds up as cold, dense gas in a protogalaxy in the core of the dark matter halo.

Galactic Star formation

The gas in a dark matter halo eventually gains control over the dark matter's gravity as it cools and moves within. After that, it collapses under the force of its own gravity, and when

effective cooling is present, this collapse intensifies. Collapse raises the gas's density and temperature, which typically speeds up the cooling process while slowing down the collapse process. A visible galaxy could be created as a result of the gas cloud fragmenting into small, high-density centres during such a rapid collapse. Observations frequently allow us to discriminate between two different star formation scenarios: quiet star formation in rotationally supported gas disks and starbursts. The latter are restricted to relatively limited regions (generally the nucleus) of galaxies and are identified by the significantly higher star-formation rates. Strong dynamical interactions or instabilities seem to be what causes starbursts, which call for the accumulation of a lot of gas in a limited volume.

Chemical properties

In astrophysics, the word metals refers to all chemical elements heavier than helium. The term metallicity then refers to the mass proportion of a baryonic component (such as hot gas, cold gas, or stars) in metals. During the first three minutes of the Universe (the period of primordial nucleosynthesis), nuclear reactions resulted in a medium composed mainly of hydrogen ($\sim 75\%$ of the total) and helium ($\sim 25\%$), with a very small amount of metals mostly in the form of lithium. All other metals were created later in the universe as a result of nuclear reactions in stars. The ISM is enriched with newly synthesized metals when stars release material through stellar winds or supernova explosions. It is crucial to understand how galaxies evolve their gas and star chemical compositions for a number of reasons. First, a stellar population's luminosity and its color depend on the metallicity of the stars as well as its age and initial mass function (IMF). Secondly, the cooling efficiency of gas is strongly depended on its metallicity. The most metal-enriched gas cools more quickly than the metal-poor gas. Finally, small particles of heavy elements known as dust grains, which are mixed with the interstellar gas in galaxies, can absorb significant amounts of the starlight and re-radiate it in infrared wavelengths.

Black hole formation and its critical role on galaxy evolution

A super-massive black hole mass $10^6 M_{\odot}$) is found in the center of almost every galaxy. According to more detailed studies (e.g (McConnell, Ma, 2013)), the Black Hole mass closely correlates with the bulge mass and central velocity dispersion in nearby galaxies, pointing to either co-evolution or feedback control between Central super-massive black hole and their host galaxies (e.g. (Fabian, 2012)). However, it is likely that the least known physical processes in galaxy formation and evolution are the formation, growth, and feedback of super massive black holes. The Black Hole seeds are thought to develop either through the direct collapse of a gas cloud (large seeds with mass $> 10^4 M_{\odot}$) or through the supernova explosion of Population III (Pop III) stars (light seeds around $100 M_{\odot}$). Some of these seed Black Holes must experience dynamical friction to fall into the galactic center and must experience accretion and merging to increase in mass by several orders of magnitude. The host galaxy is greatly impacted by the enormous energy released by Black Hole accretion. The most frequently mentioned Black Hole feedback mechanisms include radiation pressure, heating from relativistic jets, and accretion disk winds (line-driven winds launched from the accretion disk with an initial velocity $30,000 \text{ km/s}^{-1}$). At high accretion rates, the first two mentioned points are referred to as quasar-mode feedback, which push powerful outflows and controls star formation. At low accretion rates, the jet heating is also referred to as

radio-mode feedback, which is primarily used to keep huge galaxies from quenching. Since we don't basically know any of these processes, models of galaxy formation must use data from observations.

1.2 Baryonic cycle

Understanding the formation and evolution of galaxies totally depends on being able to trace the migration of baryons between galaxies and the circumgalactic medium. The complex process known as the baryon cycle encompasses all the ways in which gas is continuously treated in over-densities. Gas entering galactic potentials, collapsing into and being processed by stars, being ejected due to feedback from stars and/or AGN, and even mixing due to cooling. The Interstellar Medium (ISM), the Circumgalactic Medium (CGM), and the extended environment are the three places in which multi-phase gas flows inside and between. The Circumgalactic Medium, which extends up to roughly a galaxy's virial radius, is a loosely defined gaseous halo. The CGM is the region where gas from the intergalactic medium enters and where metals that have been ejected from the galactic disc by galactic winds caused by supernovae with intense star formation activity are recycled (Fig.1.1). The majority of the material is still bounded and returns as a galactic fountain, replenishing the ISM with metals (Fraternali, 2017). The percentage of material that is ejected from the galaxy by galactic winds, the percentage of metals recycled back into the ISM, and the normal time frames for these processes are all parts of baryonic cycle whose physical mechanisms are mainly open questions. Cool, clumpy, collisionally ionized ($T \sim 10^4$ to $\sim 10^{5.5}$ K), low density gas under the influence of the CGM has velocities below the galaxy escape velocity. It is a multi-phase medium made up of layers or clouds of cool gas inside the R_{vir} mixed with hot ionized gas, which can be traced by emission lines such as [OVI]. While the hot gas remains constant over time, it progressively transforms into diffuse and hot ($T 10^6$ K) Warm-Hot Intergalactic Medium (WHIM), which is extending to the 1 Mpc from the galaxy and is visible in X-ray (Tumlinson et al., 2017). Furthermore, the majority of the metal and hydrogen emission lines are in the UV, making it difficult to observe them and frequently necessitating the employment of space UV observatories. With the so-called down-the-barrel method (e.g (Martin, 2005)), we can utilise the light from the host galaxy to track the absorption lines from its own CGM in order to investigate the absorption signatures in the spectra of distant luminous sources. The CGM, which the quasar absorption was able to trace, has been found around a variety of galaxies, including quasars, star-forming galaxies at various redshifts, and also around quiescent objects.

The nature of the quenching processes preventing that material from being accreted onto the galaxy is questioned by the existence of the cold medium near quiescent objects (Tumlinson et al., 2017). The distribution of newly created metals and the regulation of star formation processes are all governed by the local cycle of baryons between the ISM and CGM. In order to maintain star formation, galaxies cannot evolve independently; instead, they must accrete gas from the intergalactic medium to replenish their ISM gas reservoirs. Galactic winds are generated by star formation and AGN activity, which causes metal-rich material to be thrown back to the CGM and possibly completely removed from the system. This affects the ISM gas reservoirs and may stop further accretion, which starts quenching. This gas cycle is crucial to the processes guiding galaxy evolution and star formation. The questions of how galaxies support star formation, how much matter is accreted through the

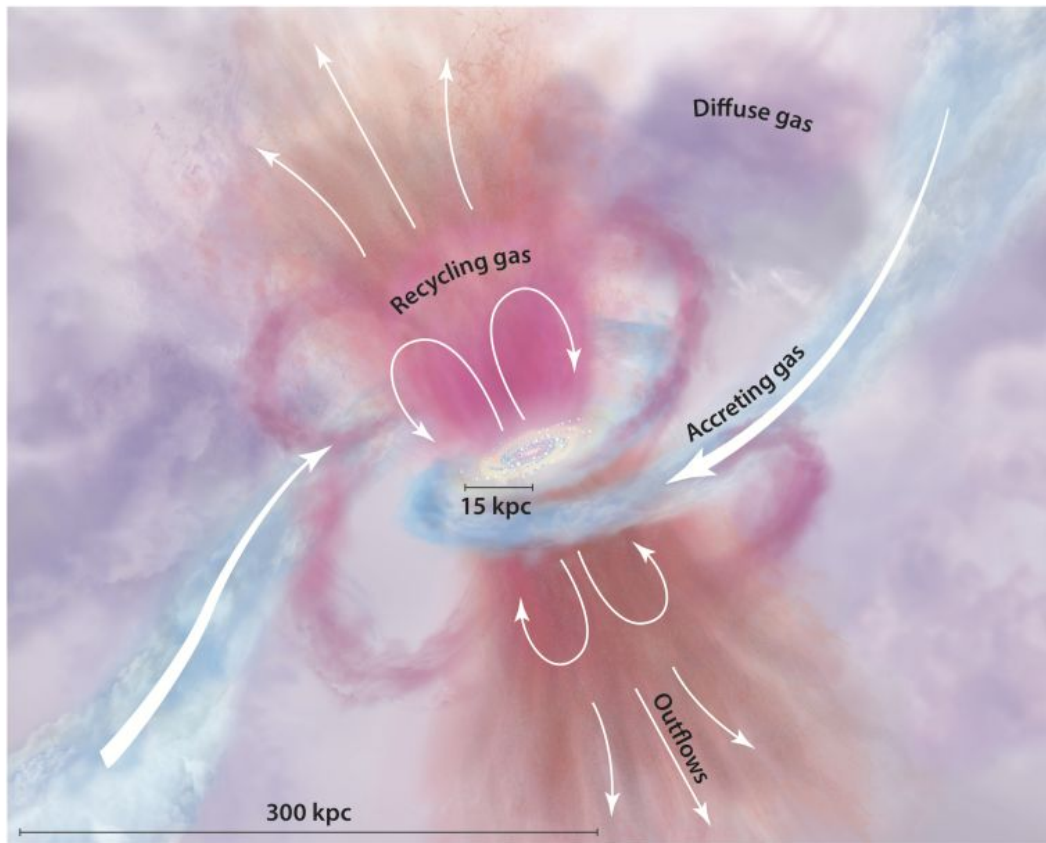


Figure 1.1. A schematic of the Circumgalactic Medium. The blue represents metal-poor gas inflowing from the IGM and accreted through the CGM onto the galaxy. The star-formation enriched material (orange, pink) is expelled from the galaxy in the form of galactic winds, part of which falls back onto into the ISM as galactic fountains. The purple colour of the surrounding medium represents the mixed diffuse gas filling the CGM (demonstration from Tumlinson et al., 2017 (Tumlinson et al., 2017))

CGM, how much matter is expelled in the form of the galactic winds, and what role these outflows play in the quenching transition may all be efficiently addressed by studies of the CGM and knowing the details of the recycling of baryons.

1.3 Stellar nucleosynthesis

Chemical elements and their isotopes are produced as a result of nuclear reactions that have previously occurred shortly after the Big Bang, then in stars and the interstellar medium, where they are continuously taking place. Theoretical, experimental, and observational research are all used to study these processes. In addition to laboratory studies of nuclear and particle physics, Cosmochemical studies of elemental and isotopic abundances in the Earth and meteorites, and astronomical observations of the physical characteristics and chemical make-up of stars, galaxies, and the interstellar medium are all taken into consideration.

A couple of few seconds after Big Bang, when thermal energy was below the threshold needed to turn protons into neutrons and vice versa, the process of nucleosynthesis in the

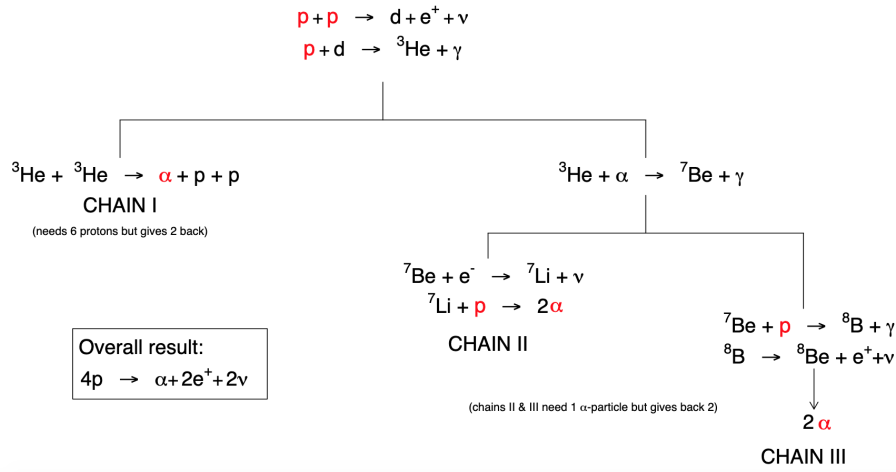
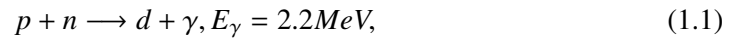


Figure 1.2. The various pp chains mechanisms for combining four protons into one α -particle . Keep in mind that each chain has a distinct energy positive output that drives the star luminosity as it gathers enough α -particle to develop mass and ignite the following stages (Thompson, Nunes, 2009).

universe began. At lower energy levels, light nuclei can spontaneously form. The deuterium (d), produced by the fusion of a proton and a neutron, is the first byproduct of primordial nucleosynthesis (PN), combination of exclusively many protons or many neutrons being unbound. It might be created at this level using the extremely exothermic reaction:



Following this time in early universe, some clouds produced by the early processes of nucleosynthesis developed into more organized spherical self-gravitating masses made primarily of Hydrogen gas with a small amount of He. A nuclear reaction consequence can be activated if the mass is such that the temperature can increase beyond 10^7 K and the density can increase above 100 g/cm^{-3} . It begins with the so-called proton-proton (pp) mechanism, which ultimately results in the creation of an α -particle (${}^4\text{He}$) from four protons. In Fig1.2, the three different reaction mechanisms that carry out this conversion are depicted in more detail. Each one is started by:



Operating through the incredibly slow weak interaction mechanism, which explains why the earliest stage of a star's life takes millions of years. Its cross section is actually so small that it has never been physically measured. This maintains star's luminosity during its evolutionary phase (known as Chains I and II) and until the star has gathered enough helium (and hence mass) to ignite the next stage. This is because helium nuclei will have sufficient energy to overcome the Coulomb barrier and fuse.

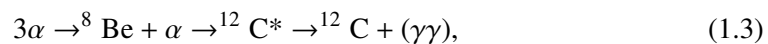
At this point, at the conclusion of the pp mechanism, stars with an initial mass less than $\sim 1.5 M_\odot$ will diverge from the main sequence. The star contracts when the pp H-burning stops, and its internal temperature does increase.

The collapsing star's initial mass, however, prevents it from converting gravitational potential energy into heat sufficient to ignite He burning. Additionally, the electron degeneracy pressure, which results from particle densities pushing electrons to ever-higher energy levels and preventing them from moving to lower levels to release gravitational potential energy, is insufficient to prevent the collapse. The Chandrasekhar limit is the name given to this mass threshold. Stars eventually become a sphere of electron degenerate matter below this. The carbon, nitrogen, and oxygen (CNO) cycles provide an alternative to hydrogen burning, but they only exist because those three components were present in the progenitor star. The CNO cycle only arose in later generations of stars that are produced from a mixture of PNH and ashes from supernovae of this initial period of stars because the early Universe was of low metallicity, i.e., did not contain much elements above ${}^4\text{He}$ (Kelly et al., 2014). The first massive stars would progress from the end of the pp-chains to helium burning due to the almost complete lack of metallicity in the immediately after the PN Universe. These stars fall under population II and population III star categories. Their explosion caused the interstellar medium to become more metallic, which is why, for instance, our Sun, which lacks the mass to initiate fusion other than the helium conversion mechanisms, has a high surface metallicity. The CNO cycles become available for the production of a α -particle from four protons in younger stars because they include carbon, nitrogen, and oxygen. A star must have a progenitor mass more than $1.5 M_{\odot}$, or a temperature lower than ~ 0.03 Giga K, for such cycles to be started. A ${}^4\text{He}$ nucleus is produced here through a series of reactions between protons and the CNO species, as shown in Fig.1.3.

The optimal cross sections of the CNO reactions occur at these temperatures, which are also significantly greater at that stage than the cross sections of the pp-chain reactions. To generate helium, these cycles accelerate dramatically. The abundance of neon in the star is another significant effect of the CNO cycles.

In population I stars, there are additional channels available for the conversion of four protons into an α -particle due to the interstellar medium enrichment in heavy nuclei. These require bigger initial masses because it takes more energy to ignite the first heavy nucleus and initiate proton fusion. Wolf-Rayet stars are common locations for such cycles. When a star runs out of hydrogen, it contracts even more as a result of gravitational pull. If the star has a mass of 0.4 solar masses, the temperature in the core rises to 0.1 Giga K, which ignites the burning of helium. It restores hydrodynamic equilibrium. The triple- α reaction reaction is primarily responsible for the first primary product in this burning phase, which is ${}^{12}\text{C}$.

Although Beryllium-8 (${}^8\text{Be}$) is only unbound by 92 keV, this translates to a lifespan of 10^{16} seconds until it decays back into two α -particle due to the ground state width of 5 eV. As a result, there is a chance that two α -particle might combine to form ${}^8\text{Be}$ and that a third α -particle could combine with this ensemble to form ${}^{12}\text{C}$:



Only the Hoyle state, a resonant O+ state in ${}^{12}\text{C}$ at 7.7 MeV, makes this process possible. Its width is sufficient for it to reach the ground state before the three α -particles split apart. In contrast to the other decay, which results in the emission of two γ -rays, the probable E0 decay from the Hoyle state to the ground state could result in the production of electron-positron pairs. The star develops into a Red Giant as it now consists of a C/O core and two outer layers of Hydrogen and Helium, with the latter layer being the deeper. If the progenitor mass is greater than $\sim 2.5(M_{\odot})$, the core material burns.

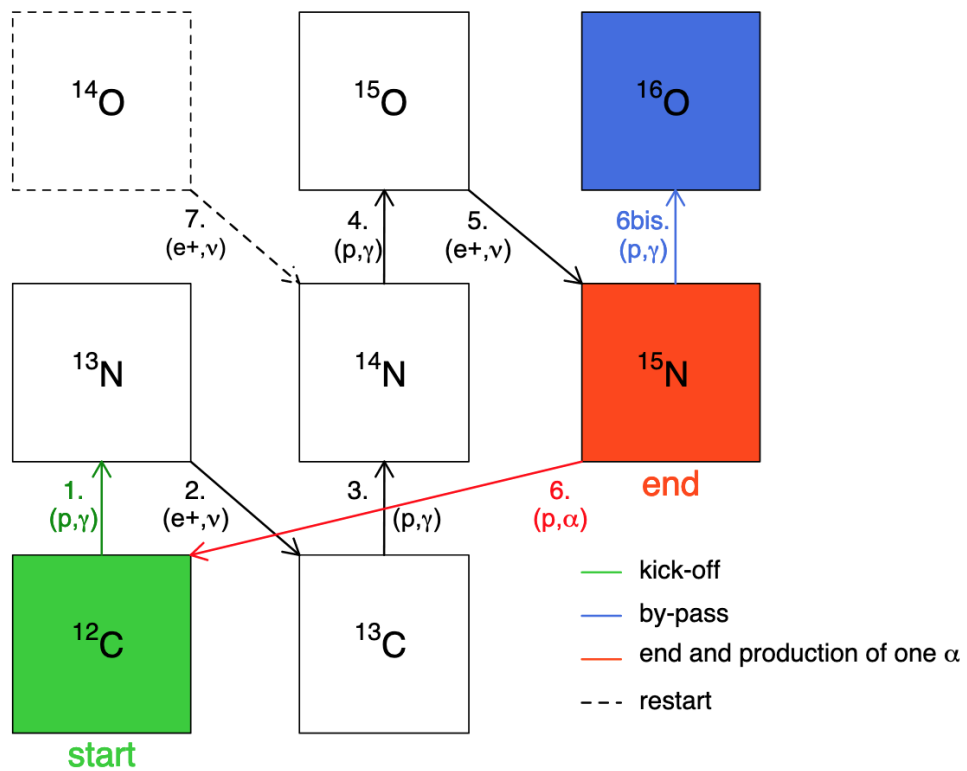


Figure 1.3. The CNO cycle results in the production of a α -particle; other cycles may follow suit if the star contains heavier seeds, such as ^{16}O . Since this CNO cycle can be bypassed, a α -particle may still be produced as a result.

When a star reaches the super giant stage and has a mass of about $M_{\star} \geq 2.5M_{\odot}$, the gravitational contraction of the core elevates the temperature to the point where carbon burning begins. The last (mass) frontier is $8 M_{\odot}$, from which stars will finish burning all further elements. Since the carbon burning byproducts will likewise fill the inert core, that is where the difference lies. Using an explosion based on core collapse, stars with greater mass can produce heavier metals like iron (Fe).

1.4 Interstellar Medium (ISM) and starforming galaxies

The interstellar medium, which fills interstellar space, is a diluted mixture of charged particles, atoms, molecules, and dust grains. Understanding its physical characteristics and dynamical impacts is crucial in many aspects of astronomy and astrophysics. These processes are all closely related to the physics of the interstellar medium, including galaxy formation and evolution, star formation, cosmic nucleosynthesis, chemical abundance, and growth of dust grains that serve as the basic building blocks of planets. Unfortunately, despite its significance, little is known about its structure and evolution. The interstellar medium is highly turbulent, has several chemical phases, and exhibits complex detail on all resolvable spatial and temporal scales, according to observations. The interstellar medium interpretation truly needs a multi-scale and multi-physics approach. In this section, I introduce the essential ISM properties to better understand the interstellar medium and its connection to HII regions and starforming galaxies.

1.4.1 HII regions and starforming galaxies

When cool gas clouds, or gas that is not supported by the kinetic energy of its component particles, start to collapse under the force of their own gravity, star formation occurs. The pressure from the parent galaxy's motion through the intergalactic medium, a collision with another nebula, a shock front from a nearby supernova, or even nothing at all could cause this collapse to happen.

With enough mass, the smaller fragments that are created as the cloud breaks apart will keep collapsing back on themselves. Gas will start to develop into a protostar and protoplanetary disk at the center of these shards. The protostar will eventually accumulate enough gas through accretion to have the mass enough to produce the high temperatures and pressures required in its core to start fusing hydrogen into helium, and a star will be born.

When massive and young stars ionize neighboring gas clouds with high energetic radiation (UV wavelength), emission nebulae called HII regions are formed. They have temperatures of about 10000 K and are mostly made of hydrogen, hence the name (astronomers use the terms HII for ionized hydrogen and HI for neutral hydrogen). There are hot stars in locations where stars are developing that have effective temperatures so high that they can ionize atomic hydrogen by producing photons with wavelengths shorter than $\text{Ly}\alpha$ (Dijkstra, Jeason-Daniel, 2013). It is then possible to ionize the gas nearby these bright stars.

HII regions consist of gas in equilibrium between photoionization and the inverse process which is known as recombination. Ions capture free electrons during recombination. Astronomers refer to singly ionized hydrogen as the HII region. the number of recombinations rate (number of recombinations per unit volume per unit time) is:

$$r = n_p n_e \langle \sigma_V \rangle = r = n_p n_e \alpha_T, \quad (1.4)$$

where the cross section, σ , has been averaged across a range of velocities. The number density of free protons in this equation is n_p , while the number density of free electrons is n_e . For a gas composed primarily of hydrogen to be neutral, there must be an equal amount of free protons and electrons $n_p \sim n_e$. We can assume that the gas is completely ionized within a radius r_{strom} . An ionization source that produces ionizing photons at a rate of Q^* is located in the middle (photons per second). Inferring Q for a star:

$$Q^* = \int_{h\nu=13.6\text{eV}}^{\infty} (L_\nu/h\nu) d\nu, \quad (1.5)$$

The minimum energy required to produce ionized neutral hydrogen is 13.6 eV. For an O5V star $Q^* \sim 10^{49} s^{-1}$. Since we assume that every ionizing photon is absorbed, the ionization rate over the sphere is equal to Q^* . The recombination rate over the sphere, integrated is:

$$\int r dV = (4\pi/3) r_{strom}^3 \alpha_T (n_e/n_H)^2 n_H^2 \quad (1.6)$$

When the recombination rate is balanced against the ionization rate with the assumption that the medium is fully ionized ($x=n_e/n_H=1$), the following result is obtained:

$$r_{strom} = (3 \times Q^* / 4\pi \alpha_T n_H^2)^{1/3} \quad (1.7)$$

One should not only balance ionization inside the HII region but also heating and cooling. The absorption of UV photons leads to heating. The balance between the two processes is achieved at an equilibrium temperature that is typically $\sim 10^4\text{K}$. At this temperature $\alpha_T \sim 2.6 \times 10^{13} \text{cm}^3 \text{s}^{-1}$.

A Strömgren sphere's radius (Strömgren, 1939) at $n_H \approx 10^4 \text{cm}^{-3}$ density is a small portion of a parsec. The Thompson scattering causes this to be significantly smaller than the mean free path ($\sigma_T = 6.8 \times 10^{-25} \text{cm}^2$). During recombination, optical and infrared photons have a propensity to easily elude detection (unless the system is young and very optically thick).

An ion won't always be in its ground state after recently recombining. It will eventually reach the ground state by emission lines of decay (like Balmer series transitions, for example). While the $\text{Ly}\alpha$ photons are absorbed and re-emitted, the lower energy emission lines will escape. As a result, the ionizing photons' energy will mainly be released again in the form of photons that can leave the ionized gas. A sizable portion of the total energy received is frequently released as $\text{H}\alpha$. HII regions have extremely abundant emission lines in their UV, visible, and IR spectra. These lines are primarily collisionally excited lines of metal ions and recombination lines of hydrogen and helium.

In conclusion, three processes govern the main physics of HII regions:

Photoionization Equilibrium

The equilibrium between recombination and photoionization: this establishes both the nebula's structure and the spatial distribution of the ionic states of the constituent elements in the ionized zone.

Thermal Balance between heating and cooling

Photoelectrons with thermal energy of a few eV that are ejected from Hydrogen and Helium are the primary source of heating. Most HII regions cool primarily as a result of metal ion excitation by electron-ion impact, followed by the emission of forbidden lines from low-lying fine structure levels. These cooling lines are responsible for the distinctive spectra of HII regions.

Hydrodynamics

Shocks, ionization and photodissociation fronts, as well as outflows and winds from embedded stars.

1.5 Ionisation properties

Ionisation parameter controls the ionization state (Tarter et al., 1969), and it is independent to other parameters (Dopita et al., 2000). The dimensionless ionization parameter (in log scale) covers a wide numeric intervals roughly between -3.2 to -2.9, for both nearby HII regions and starforming galaxies (Dopita et al., 2000; Moustakas et al., 2010; Poetrodjojo et al., 2019). The ionization parameter (U) is potentially beneficial as a tool to measure radiation pressure feedback from different sources. Different mechanisms have been investigated to analyze U , such as radiation pressure confinement, expanding wind bubbles, elements ionisation, and the effects of dust (e.g (Yeh, Matzner, 2012)).

It is very important, from the observational point of view, to find emission lines which can be used to estimate the ionisation parameter and calibrate them. Notwithstanding the importance of the ionization parameter in knowing the physical properties of ionizing sources and their influence on the surrounding ISM, few ionization parameter calibrations have been performed. The ionization parameter is normally measured by comparing two emission-lines from the same atomic species which are in different ionization states. Many different species can be utilized to estimate the ionization parameter including carbon, sulphur, nitrogen, and oxygen.

In the optical bands, there are two important strong-line ionization parameter diagrams. First of all O32, based on the $[OIII] \lambda 5007 / [OII] \lambda \lambda 3727, 29$ ratio (Aller, 1942; Kewley, Dopita, 2002a). This is an excitation diagnostic and its ratio has a strong dependence on the the gas-phase metallicity (Kewley, Dopita, 2002a) and it is strongly influenced by the ISM pressure in metal-rich galaxies, according to collisional de-excitation of [OII]. The second optical line ratios is related to sulfur. The S32 diagnostic is another important lines ratio to analyse ionisation parameter based on the $([SIII] \lambda 9069 + [SIII] \lambda 9531) / [SII] \lambda \lambda 6717, 31$ ratio, first proposed by (Kewley, Dopita, 2002a) and developed by (Morisset et al., 2016; Dors et al., 2011). This line ratio is very sensitive to ionization parameter. The S32 ratio is not sensitive to the ISM pressure. An essential caution with the use of the S32 ratio is that the [SII] lines have been underestimated by current photoionization models, particularly at very low metallicities. This underestimation can be ascribed to the stellar evolution models producing a radiation field that is harder than observations or the lack of knowledge on dielectric recombination coefficients of sulfur (Levesque et al., 2010; Izotov et al., 2009). Fig1.4 shows the most well-known relation between different optical line ratios and ionisation parameter (from figure 7 in (Kewley et al., 2019)).

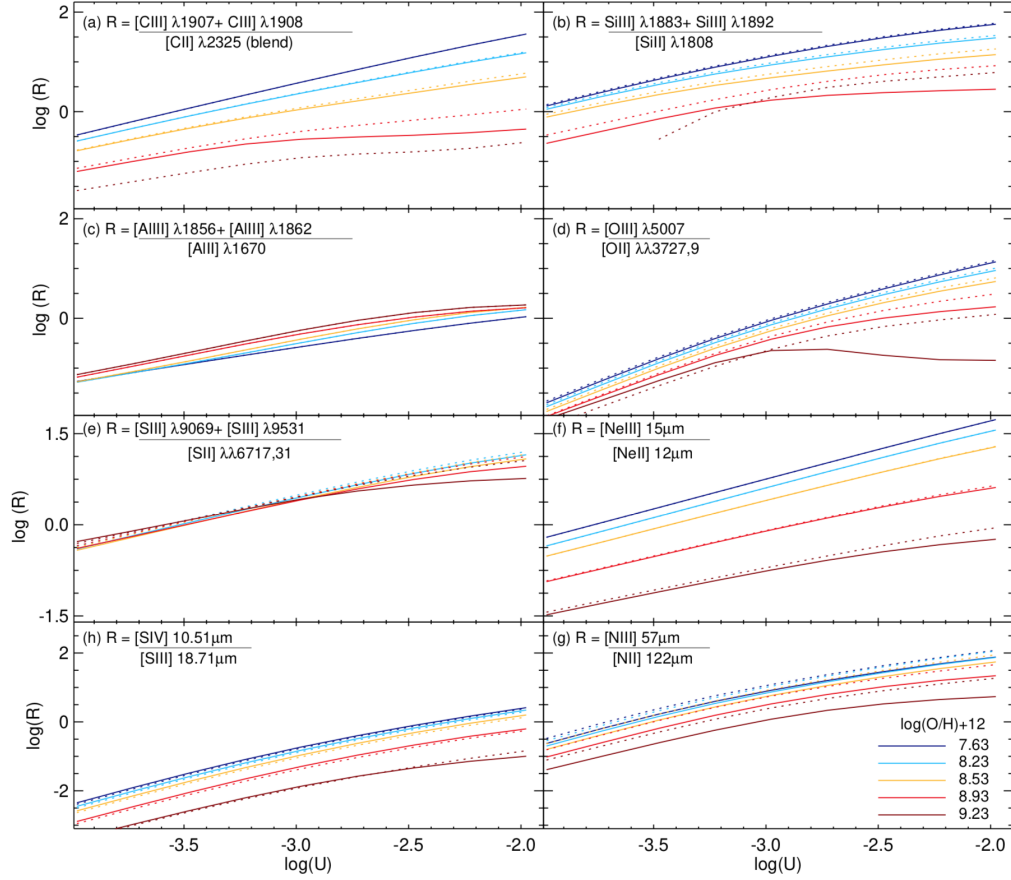


Figure 1.4. the most important ionization parameter diagnostic line ratios as a function of metallicity in the different gas-phase metallicity. Solid and dotted lines correspond to different ISM pressures between 5 and 7, respectively (Kewley et al., 2019).

The global ionization parameter in galaxies is usually anti-correlated with the gas-phase metallicity (Dopita, Evans, 1986). The cause of this anti-correlation between ionization parameter and metallicity is not clear now. (Dopita et al., 2006) suggested that the anti-correlation is caused by stellar atmospheres. At high metallicity, the stellar wind has a larger metal opacity, and absorbs a larger fraction of the ionizing photons, leaving less high energetic photons to ionize the circumjacent HII region. Metal-rich stellar atmospheres also scatter photons from the photosphere more efficiently than metal-poor atmospheres. This process permits luminous energy to be converted to mechanical energy more efficiently in the stellar wind region, reducing the number of ionizing photons incident on the HII region. By contrast, the recent studies describe a positive or constant relation between ionisation parameter and metallicity (see Fig.1.5).

1.6 Dust

Dust is another important components for studying the galaxy formation and evolution and it has a crucial role in many astrophysical aspects such as extinction (absorption and scattering) matter of radiation, an emission source in infrared wavelengths, a coolant and a heat source

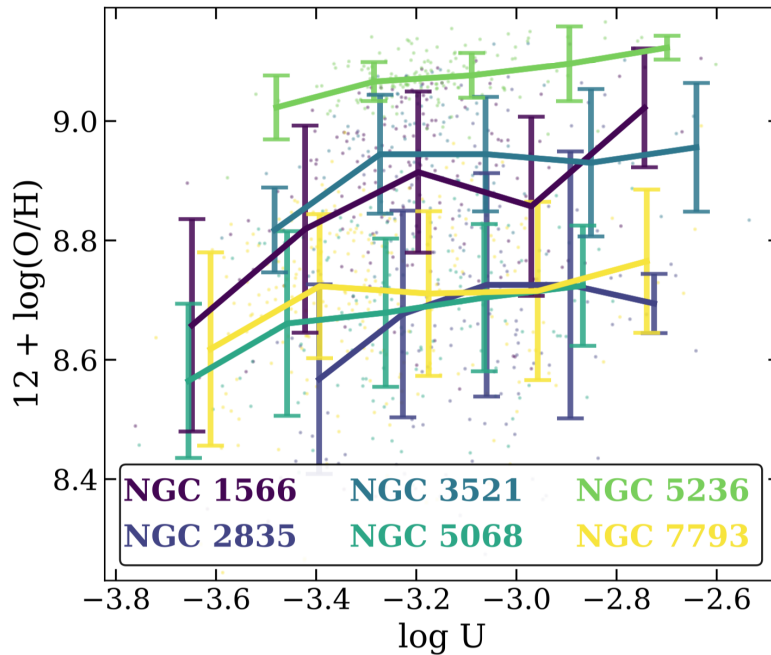


Figure 1.5. Gas-phase metallicity of different HII regions versus the ionization parameter, U , colored by each individual galaxy (Grasha et al., 2022). There is a correlated relation between ionisation parameter and metallicity.

in ISM and intergalactic medium (IGM), and a place for the creation of molecules. Through the formation of new stars, there is a correlation between dust abundance with galaxy growth. Dust grains are formed in rapidly-cooling gas of stellar outflows (stardust) (Draine, Salpeter, 1979; Yamamoto, Hasegawa, 1977). Sources of the stardust can be different sources like asymptotic giant branch (AGB) stars, supernovae, novae, Wolf-Rayet stars, red supergiants, and other physical mechanisms (e.g., (Gehrz, 1989)). For example, the central source of the star dust in the present Milky Way and the Magellanic Clouds is connected to AGB stars (Draine, 2009; Matsuura et al., 2015).

Supernovae (SNe) may also play a particular role on production of stardust ((Todini, Ferrara, 2001; Nozawa et al., 2011; Kozasa et al., 2009)). Stardust from SNe was particularly important in the early time of universe (higher red shifts) because the time for stars to evolve to the AGB phase (Morgan, Edmunds, 2003; Dwek, Cherchneff, 2011). *Additionally, the first stardust may have been crucial in transforming the mode of star formation from massive star dominated starlike (Schneider et al., 2006).*

Stardust grains are treated in ISM after being injected there. Protons that are moving thermally assault the grain in heated gas, causing it to splutter (Onaka, Kamijo, 1978; Draine, Salpeter, 1979). Moreover, SNes shock waves probably decrease dust grains by grain-grain collisional shattering as well as sputtering (e.g., (Dwek, Arendt, 1992; Nozawa et al., 2006; Silvia et al., 2010)). This kind of destruction process is widely confirmed and observational evidence of the destruction has been investigated in several studies with the Spitzer Space Telescope (Borkowski et al., 2006; Dwek, Cherchneff, 2011; Mouri, Taniguchi, 2000). In Fig1.6, in the case of dust production by SNe, astronomers used NASA's Spitzer Space

Telescope to create this infrared image of the spiral galaxy M74.

Another important and effective channel of dust formation is required to maintain dust content in galaxies. The most plausible mechanism is accretion growth in the ISM (e.g. (Draine, 1990)); in dense molecular clouds, atoms and molecules of some refractory elements collapse onto existing grains and may change from the gas phase to the solid phase (deposition phase). This type of growth is beneficial to clarify the observed depletion of some elements in the gas phase of the ISM relative to solar abundance (for one of these kinds of correlations: (Savage, Sembach, 1996)). Moreover, dust affects the shape of the IMF, through favouring the formation of low-mass stars by fostering cloud fragmentation in low-metallicity environments and inhibiting the formation of massive stars (Omukai et al., 2005).

At the end, dust comprises a source of complications for investigations about optical nebular diagnostics of the ISM, because of its obscuring effects. In the optical wavelength range, dust both attenuates light and provides variations in the shape of the spectrum, by absorbing mostly at bluer wavelengths and less at redder ones. At a particular wavelength, the extinction in magnitudes can be expressed as:

$$A = 2.5 \log(F^0/F) \quad (1.8)$$

where F^0 and F are the intrinsic and observed flux respectively. The parameterization of the wavelength dependence of A is usually described in terms of an extinction curve:

$$k = A/E(B - V) \quad (1.9)$$

where $E(B-V)$ is the color by difference in the B and V magnitudes. Extinction curves can be obtained for the Milky Way (Cardelli et al., 1989). The condition is complicated for extragalactic sources, due to the complex distribution and geometry of stars and dust (Calzetti et al., 2000)(see Fig.1.7). To apply reddening correction for emission lines fluxes, a usual procedure consist in comparing the observed ratio of two Balmer lines (generally $H\alpha$ and $H\beta$, the so-called Balmer decrement) with the one predicted theoretically ($H\alpha/H\beta = 2.87$ for case B recombination at 10000 K) and obtain, once a given extinction curve is assumed, the $E(B-V)$ from the equation:

$$F_{H\alpha}/F_{H\beta} = (F_{H\alpha}^0/F_{H\beta}^0)10^{-0.4E(B-V)(k_{H\alpha}-k_{H\beta})} \quad (1.10)$$

The Balmer decrement, however, is sensitive to modest extinction levels. For instance, regions of lower attenuation will dominate the observed flux and this could bias the inferred extinction towards lower values.

1.7 Metallicity in galaxy evolution

As element abundances and their variations throughout cosmic epochs offer unique information on the physical mechanisms driving the evolution of galaxies, metallicity is a key parameter to study galaxy evolution (see, e.g. (Maiolino, Mannucci, 2019a)).

In reality, the amount of metals in galaxies provides a measurement of the total star production as well as the percentage of metals lost through outflows and stripping. In particular, the quantity of metals gives a measure of the integrated star production in galaxies because all elements heavier than lithium are produced in stellar nuclei. A further indication



Figure 1.6. Dust in the spiral galaxy M74 appears red in this image from NASA's Spitzer Space Telescope. Data from Spitzer provided evidence that supernovae, act as dust factories, seeding galaxies with cosmic dust particles. The image is an infrared composite, in which 3.6 micron light is blue, 4.5 micron light is green, and 8 micron light is red (courtesy: *NASA/JPL – Caltech/STScI*)

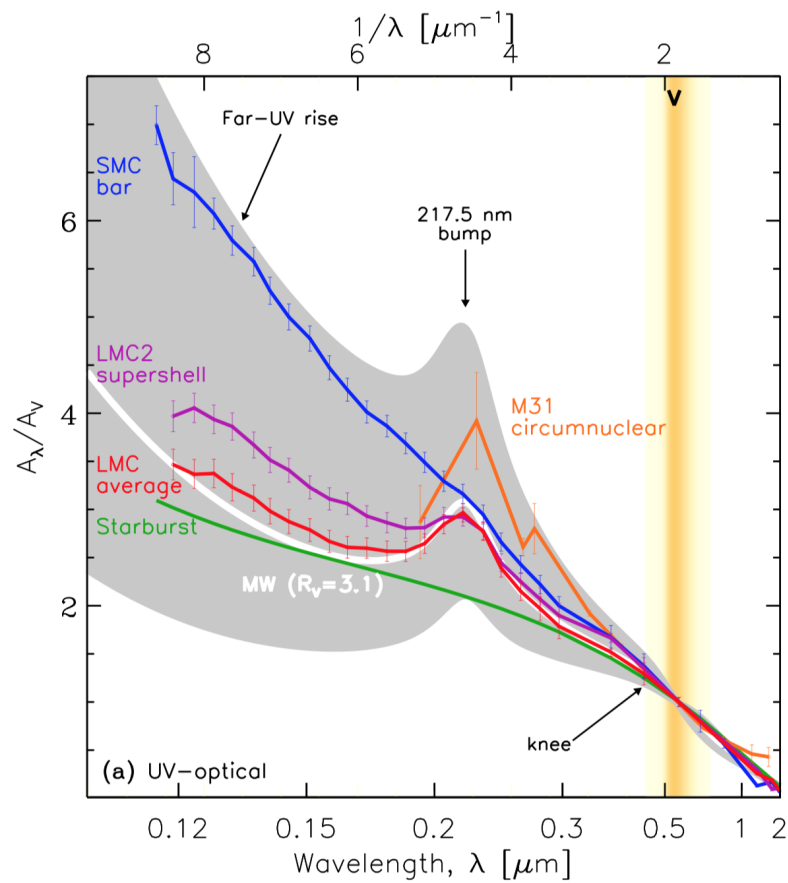


Figure 1.7. The Magellanic clouds extinction curve (Gordon et al., 2003) and a comparison to the Milky Way (in different R_V), demonstrating the attenuation curve of starburst galaxies (Calzetti et al., 2000) and situated around a nucleus of M31 (Dong et al., 2015)

that metallicity tracks gas inflows and outflows from galaxies is the existence of scaling relations between metallicity and galaxy characteristics, such as the mass metallicity and fundamental metallicity relations. The metallicity, or the proportion of metals to hydrogen and helium, is likewise susceptible to dilution brought on by the introduction of pristine gas. Because of this, learning about the metals present and the metallicity of galaxies is incredibly important for understanding the fundamental processes behind galaxy evolution. Additionally, because distinct populations of stars enrich various chemical elements over varying timescales, we can derive special restrictions on the history of star formation from the relative abundance of chemical elements.

In addition to providing information on other internal phenomena like galactic fountains, stellar migration, and radial gas inflows, the analysis of the metallicity and chemical abundances on spatially resolved scales (gradients) sheds light on the processes that have controlled the growth and assembly of galaxies. This makes the gas-phase metallicity, which is the relative abundance of all heavy metals in the ISM with respect to hydrogen, a fossil record of a galaxy's recent star formation activity. Being a relative measurement of the ISM hydrogen content, it is also sensitive to processes involving gas flows that may have an impact on the gas repository, such as inflows of pure gas that could dilute it or outflows that could eject a significant portion of enriched material into the intergalactic medium.

The main tracers of the chemical evolution of the ISM in our galaxy and extragalaxies are ionized nebulae, which are our major probes of the gas-phase abundances in regions of recent star formation.

Due to oxygen abundance and its role in some of the brightest emission lines found in nebular spectra, oxygen is the most abundant metal by mass in the ISM. As a result, its abundance is frequently taken as a gauge of the total metallicity and is expressed in units of $12 + \log(O/H)$, where O/H is the ratio of oxygen to hydrogen atoms. To estimate the amount of metals and specific chemical elements, various definitions are used. The mass of all metals in relation to the total mass of baryons (which are primarily made up of hydrogen and helium) is indicated by the metallicity (Z):

$$Z \equiv M_{metals}/M_{baryons} \quad (1.11)$$

The relative abundance of two generic chemical elements X and Y is generally expressed in terms of relative number densities N (solar value), with the below equation:

$$[X/Y] \equiv \log(N_X/N_Y) - \log(N_X/N_Y)_\odot \quad (1.12)$$

The following expression is also frequently used to convey the relative abundance of chemical components to hydrogen:

$$12 + \log(X/H) \equiv 12 + \log(N_X/N_H) \quad (1.13)$$

Where the value 12 was introduced so that any element, even the most rare, has a positive Solar values in Eq.1.13.

As a result, the metallicity is frequently stated as:

$$12 + \log(O/H) \equiv 12 + \log(N_O/N_H) \quad (1.14)$$

According to the review by Asplund et al (2009)(Asplund et al., 2009) the solar value for Eq.1.14 gives $12 + \log(O/H) = 8.69(\pm 0.05)$ based on three dimensional, time dependent

hydrodynamical model of the Solar atmosphere. The fundamental idea is that different studies should always be scaled to the same Solar reference value when we are comparing them. It must be clear that, given that the relative abundance of the chemical elements might vary significantly with respect to the solar value, utilizing the O/H abundance is simply a rough approximation of the gas's actual metallicity.

1.7.1 Empirical method

The Empirical method uses the information directly inferred from the emission lines in spectra. The metallicity of a galaxy can be measured from the integrated emission of stars, from warm ($\sim 10^4$ K), ionised interstellar medium, hot ($\sim 10^6$ K) ionised intracluster (ICM), circumgalactic medium (CGM), and from the absorption features caused by cold/warm ICM/CGM on the spectra of distant quasars and galaxies. The emission line spectrum of photoionized gas can provide information on the gas physical properties like metallicity, temperature, and density. In particular, the measurement of metallicity strongly depends on the density, temperature and ionization status of the ionised gas.

T_e metallicity method (Direct method)

The term Direct method refers to the use of temperature-sensitive auroral lines to measure metallicities. It is based on the electron temperature obtained from optically sensitive auroral lines. Particularly in the metal-rich galaxies, these emission lines are quite faint and typically cannot be seen. The main auroral lines to determine metallicity are [OIII] λ 4363, [OII] λ 7320,7330, [NII] λ 5755, and [SII] λ 4066.

In practice, assuming a uniform chemical composition and a certain ionization structure of the nebula, one can express the relative abundance of an element compared to hydrogen as:

$$N(X^i)/N(H^+) = (I_\lambda/I_{H\beta}) \times (\epsilon_{H\beta}(T_e, n_e)/\epsilon_\lambda(T_e, n_e)) \times icf \quad (1.15)$$

where I is the intensity of the transition responsible for the emission at particular wavelength, ϵ is the volumetric emissivity and T_e , n_e are the electron temperature and density representative of the emission; icf is the ionization correction factor. Inferring, for instance, the relative quantity of the doubly ionized oxygen relative to hydrogen can be obtained:

$$O^{2+}/H^+ \equiv (I([OIII]\lambda 5007)/I(H\beta))/\epsilon_{[OIII]}(T_e n_e)/\epsilon_{[H\beta]}(T_e n_e) \quad (1.16)$$

Since line ratios are independent of distance and do not require absolute calibration, they are typically measured instead of total line luminosities to describe the gas-metallicity value. For instance, because $H\beta$ is widely observed and typically not blended with other lines, it is common practice at optical wavelengths to evaluate line strengths relative to this line. Because the emissivities of collisionally excited lines, such as [OIII] λ 5007), and hydrogen recombination lines have highly distinct temperature dependence, their relative ratio also depends significantly on electron temperature.

Therefore, correct knowledge and assessment of both electron temperature and density are necessary for the application of this method. The electron temperature in the O^{2+} zone is determined using the [OIII] λ 4363 line and the neighboring [OIII] λ 4959,5007

lines ($T_e([\text{OIII}])$). Since $T_e([\text{OIII}])$ does not represent the typical electron temperature, it is additionally necessary to estimate the temperature in the invisible zones. A high-ionization (H^{2+} and He^+) zone and a low-ionization (H^{2+} , He) zone are typically considered to exist. Some authors use average electron temperatures of several atoms to estimate the electron temperature in each zone Lara-López et al. (2014). Typically, $T_e([\text{OII}])$ —the temperature in the O+ zone—is determined by fitting the relation between $T_e([\text{OII}])$ and $T_e([\text{OIII}])$ derived from photoionization models. It is necessary to take into account an electron density, which is computed using the [OII] or [SII] doublets based on photoionization models of simple atoms. Ionic abundances, or the abundances of each ion (such as O^+ and O^{2+}), are then calculated using the temperatures.

It is important to note that different line diagnostics, involving various ionic species, only trace the physical conditions in the region of the nebula in which they are emitted. For instance, [OIII] and [NII] emission probes various temperature zones within the nebula.

While [NII] emission originates from the low-ionization zone, which is also traced, for instance, by [SII] and [OII], [OIII] emission is mostly produced in the high-ionization zone. When there are few diagnostics available, the physical conditions of the other regions can be deduced either practically or theoretically from the theoretical relations suggested by photoionization models (Garnett, 1992; Pilyugin et al., 2006a). However, even when taking into account ionic species coming from the same zone, significant temperature variations have been found (e.g (Bresolin et al., 2005; Binette et al., 2012; Berg et al., 2016)

Strong line method

which discussed in 1.7.1

The auroral lines are usually many times weaker than $\text{H}\beta$ for a normal nebular conditions, and their emissivity is strongly temperature dependent.

Given the usual sensitivity of the existing astronomical instrumentation, auroral lines are also particularly challenging to detect in high-metallicity galaxies and are also more challenging to observe in high redshift galaxies. Utilizing the emission line ratios between a few strong nebular lines is one of the crucial ways to address the aforementioned problems because it is well known that these ratios rely on the oxygen abundance.

Given the extreme faintness of auroral lines, it has been suggested that these line ratios might be calibrated against the oxygen abundance and employed as metallicity indicators for galaxies in which the use of the T_e approach is not sufficiently accurate. Strong-line approaches are the common name for this type of calculation. For the first time, (Pagel et al., 1979) introduced the $([\text{OII}]\lambda 3727 + [\text{OIII}]\lambda\lambda 4959, 5007)/\text{H}\beta$ ratio (R23) to approximate the oxygen abundance. This method has been then revised and calibrated many times by several studies, particularly (Skillman et al., 1989), that refined the method also to account for variations in the ionization parameter (McGaugh, 1991). Many other metallicity indicators have also been suggested throughout the years, requiring different metal lines:

$[\text{OIII}]\lambda 5007/[\text{NII}]\lambda 6584$ (O3N2) and $[\text{NII}]\lambda 6584/\text{H}\alpha$ Alloin et al. (1979); Storch-Bergmann et al. (1994); Pettini, Pagel (2004),

$([\text{SIII}]\lambda 9069 + [\text{SII}]\lambda\lambda 6717, 6731)/\text{H}$ (Vílchez, Esteban, 1996),

$[\text{NII}]\lambda 6584/[\text{OII}]\lambda 3727(\text{N}2\text{O}2)$ (Kewley, Dopita, 2002a),

$[\text{ArIII}]\lambda 7135/[\text{OIII}]\lambda 5007$ (Ar3O3) by (Stasińska et al., 2006),

$[\text{NeIII}]\lambda 3869/[\text{OII}]\lambda 3727$ (Ne3O2) (Nagao et al., 2006a).

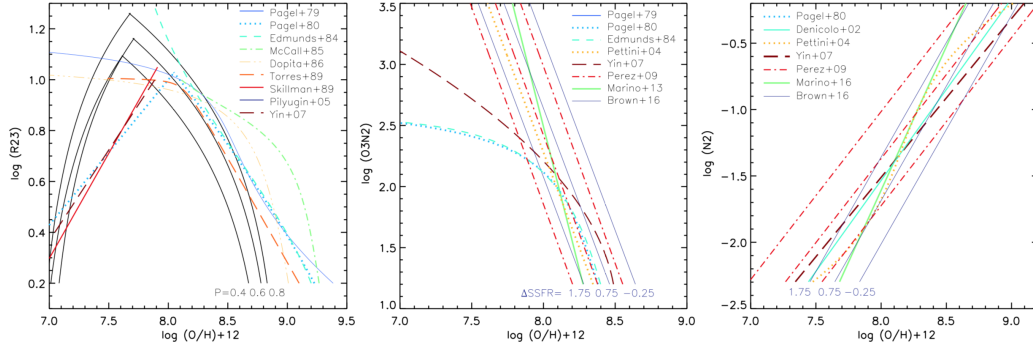


Figure 1.8. The set of strong-line metallicity diagnostics used in (Kewley et al., 2019). Empirical calibrations based on fits to T_e metallicities for samples of HII regions or galaxies. Empirical calibrations for the ratios of R23 (left) $[\text{OIII}]/\text{H}\beta/[\text{NII}]/\text{H}\alpha$ (middle), and $[\text{NII}]/\text{H}\alpha$ (right) are shown.

The use of nitrogen based indicators (either N2 or O3N2) turns out to work well since this ratios show to be correlated with O/H over the almost entire range of observed metallicities in giant HII regions, being N/O observed to increase with increasing O/H at high metallicities.

Some strong line ratios like O3O2 ($[\text{OIII}]\lambda 5007/[\text{OII}]\lambda 3727$) are strongly sensitive to the ionization state of the gas and their dependency on metallicity. This ratio shows an anti-correlation with ionization parameter, the behaviour to demonstrate the global anti-correlation for ionization parameter vs. oxygen abundance (Nagao et al., 2006a).

Calibrations of strong-line methods can be obtained in different ways: empirically based on samples of objects in which metallicity have been previously derived with the T_e method (Pettini, Pagel, 2004; Pilyugin, 2005; Marino et al., 2013), or theoretical aspect, in which the oxygen abundance dependence of different diagnostics follows the forecasts of detailed photoionization models (e.g (McGaugh, 1991; Kewley, Dopita, 2002a; Kobulnicky, Kewley, 2004a; Dopita et al., 2016)), or a combination of both empirical and theoretical ways (Maiolino et al., 2008).

An example of different kinds of calibrations are illustrated in Fig.1.8(Kewley et al., 2019). Obviously, the comparisons among metallicities estimated through different calibrations show large discrepancies with variations of the order of 0.3 to 0.6 dex (Moustakas et al., 2010; Kewley, Ellison, 2008)

In comparison to empirical calibrations based on the T_e method, the theoretical calibrations are well-established to anticipate bigger values for metallicities. These differences' causes are currently unknown. Strong-line diagnostics that are empirically calibrated have the drawback of occasionally disagreeing with the relationship between the emission line ratios and the ionization state of the gas. This is especially true for diagnostics that are calibrated against samples of HII regions with direct T_e abundances and do not take into account the dispersion and range in the calibration sample of ionization parameter (e.g (Kobulnicky, Kewley, 2004a; Blanc et al., 2015)). Another possible source of discrepancy is the potential underestimation of the chemical abundance by the T_e method in the presence of different physical conditions such as density and temperature fluctuations and temperature gradients in an ionized nebulae (for two detailed papers see Peimbert (1967); Stasińska et al. (2006)).

Recombination Line Method

When free electrons are captured by ions and descend from excited to lower levels emitting photons in the process, recombination lines (RLs) are produced. These lines are also specified as permitted lines since they typically satisfy all the selection rules for an electric dipole transition. Most of the bright RLs in emission spectra are from helium and hydrogen. Metals, such as carbon, nitrogen, and oxygen, also produce RLs but are much weaker due to their lower abundances with respect to hydrogen and helium. The emission coefficient of a recombination line, $j_{nm'}$, is given by:

$$j_{nm'} = \frac{h\nu_{nm'}}{4\pi} n(X^{+i}) n_e \alpha_{nm'}^{eff} \quad (1.17)$$

where $h\nu_{nm'}$ is the energy difference between the two levels and $\alpha_{nm'}^{eff}$ represents the effective recombination coefficient.

Some of the RLs that can be found in the spectra of ionized nebulae are: Hydrogen lines ($H\alpha$, $H\beta$, $H\gamma$), He λ 5875, He λ 4471, He λ 4686), [OI] λ 8446, [OI] λ 8447, [OII] λ 4639, [OIII] λ 3265, [CII] λ 4267, [CIII] λ 4647, [CIV] λ 4657, [NII] λ 4237, [NIII] λ 4379 and [NeII] λ 3694.

The main disadvantage of utilising recombination lines for deriving metallicities is that aside from hydrogen and helium, the recombination lines are very weak, and are only seen in nearby HII regions and planetary nebulae. In these regions, the recombination lines have been successfully used to measure carbon and oxygen abundances in some nearby extragalactic HII regions (Peimbert, Peimbert, 2013). In HII regions, recombination lines consistently give larger metallicities than Direct metallicity Peimbert et al. (1993); Mathis, Liu (1999).

1.7.2 Theoretical method

The theoretical method uses a comparative approach based on spectral properties calibrated from most precise observable emission lines inferred from prescription of detailed photoionisation models. In practice, given a set of observed emission lines, one builds a suite of photoionization models for different ionizing continua and gas physical properties (including metallicity) and find the ones which provide the best match to the observed emission lines, thus determining the gas metallicity among the other physical properties. Theoretical calibrations are calculated by mixing stellar population synthesis and photoionization models. (McGaugh, 1991) created the first theoretical metallicity calibrations using stellar evolution tracks to compute the ionizing radiation field corresponding to a zero-age burst. They calculated theoretical calibrations between line ratios and metallicity that take into account the relationship between radiation field and temperature. Theoretical calibrations were lately computed with updated photoionization models (e.g., Charlot, Longhetti (2001); Kewley, Dopita (2002b); Kobulnicky, Kewley (2004a); ?). One of the essential interests of theoretical calibrations is that a wide range of parameter space can be described, permitting one to understand the effects of galaxy properties. We should emphasize that the theoretical calibrations can not accurately describe a phenomena, as we should consider different probabilities such as model assumptions, which incorporate a plane parallel or spherical geometry, uncertain stellar atmosphere models, reliance on current atomic data, and simplified temperature and density structures.

Chapter 2

Photoionisation simulations

Photoionisation is one of the process through which an atom can be ionised by absorbing a photon. The energy beyond that required for the ionization is converted into kinetic energy of the ejected electron. Photoionization takes place when photons from an outside source ionize and irradiate gas: one star or a group of stars can act as the ionizing source. The two main processes that are associated with both equilibrium and non-equilibrium photoionization processes are cooling and heating of the gas.

Fig.2.1 shows the net cooling functions for primordial gas in ionization equilibrium at various densities and exposed to a UV radiation background with a particular intensity $J(\nu)$. The intensity adopted here is roughly that expected from the emission of quasars and young galaxies at redshift ~ 3 . As one can see, heating dominates over cooling from $T < 10^4$ K to 10^5 K, depending on the density of the gas.

With cooling, physical processes like Brmesstrahlung, recombination, and bound-bound transition produce continuum or line emission which subtract energy from the gas, while with heating energy is injected into the gas by photoionization and other physical processes.

Photoionised gas is observed in different objects such as HII region, star-forming galaxies, and Active Galactic Nuclei (AGN). The description of the photoionization process and commonly adopted procedure in the calculations of the radiation transfer through the gas clouds is described in this chapter where I discuss the assumptions and the parameters used in the photoionization simulations performed with the code CLOUDY.

2.1 CLOUDY

In this work, I have used the photoionisation modelling code CLOUDY¹ (Ferland et al., 2013) to generate synthetic spectra of HII regions. Cloudy is an open source microphysics and plasma simulation code. The goal of Cloudy is to simulate conditions in a non-equilibrium gas and to predict its spectrum, the elements ionization, the level populations and thermal state. Cloudy calculates the full radiative transfer through a gas cloud, so each individual HII region model has internal structure, with radial variations in ionization state and temperature, which in turn affect the location within the nebula where various emission lines are produced.

¹<https://trac.nublado.org/wiki/NewC17>

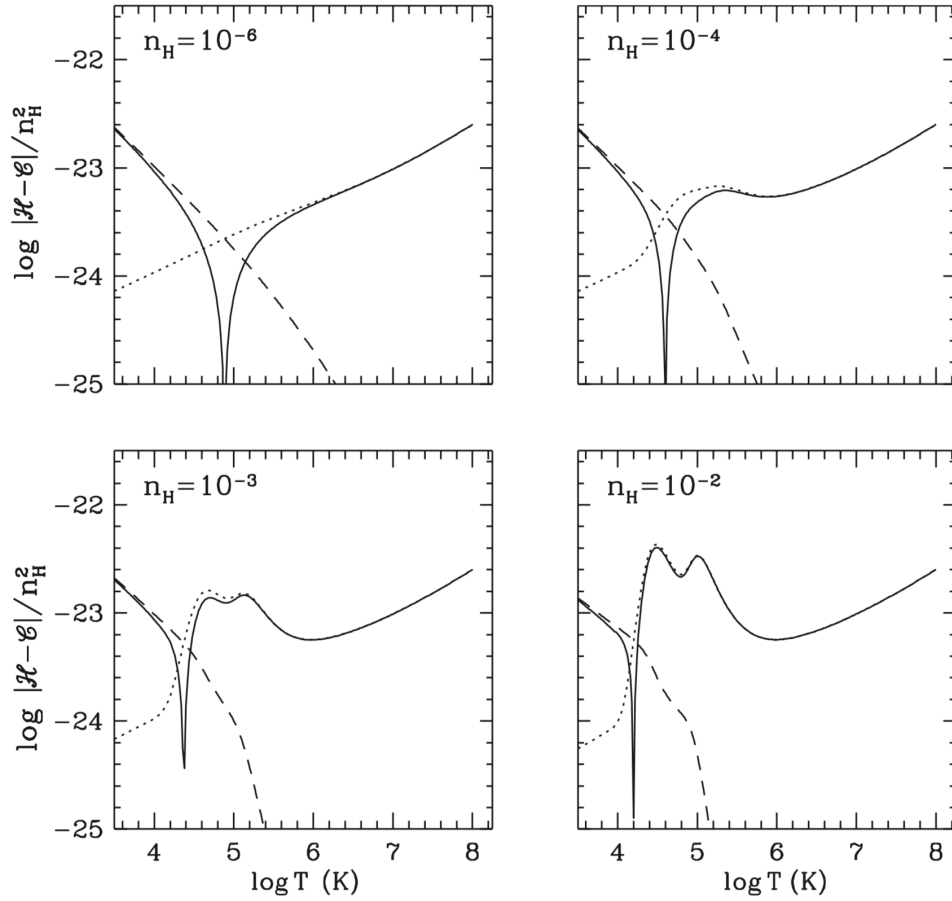


Figure 2.1. Net cooling rates as a function of temperature for a gas of primordial composition in ionization equilibrium with a UV radiation background of particular intensity $J(\nu)$. Results are shown for four different hydrogen number densities as indicated in each panel. The dotted line shows the cooling rate and the dashed line shows the rate of heating by photoionization. The solid curve shows the absolute value of the net cooling rate (in $\text{erg cm}^3 \text{s}^{-1}$) (Weinberg et al., 1997) and this new version of figure used from (Mo et al., 2010).

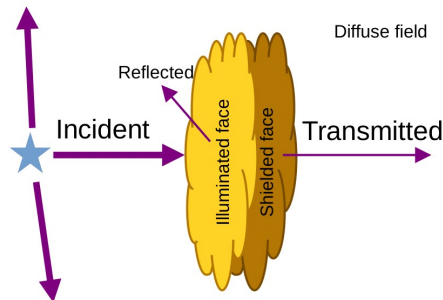
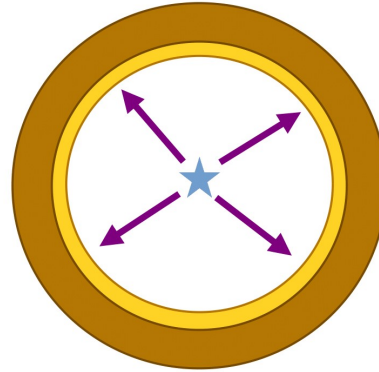
Open geometry**Closed geometry**

Figure 2.2. A cartoon picture to show open geometry (left part), which Several of the radiation fields that enter in the calculations, and close geometry (right part).

2.1.1 Assumptions

To run a Cloudy simulation, we need to provide several input parameters needed which we describe here. We then show a few examples to demonstrate our models' predictions.

Geometry

We use a one-dimensional spherical geometry. Cloudy considers the possibility of modelling both an open or closed geometry. In this work we assume an open geometry. An open geometry is one in which the covering factor of the gas ²is small. Fig.2.2 shows the different geometries. We assume that the central star produces a photoionizing flux that is isotropic as seen from the position of the star. This assumption implies that, if the nebula is ionization-bounded, the rate of photoionizations (and recombinations) produced in the nebula is independent of direction and is a constant for a given solid angle (as seen from the star).

Ionisation versus matter bounded

There are two limiting cases for the hydrogen-ionization structure of a cloud: Ionisation bounded and matter bounded. In the matter bounded case, the outer limit to the H⁺ region is determined by the outer edge of the cloud. In this case, the cloud is ionized throughout and is optically thin to the incident radiation field. In the radiation bounded situation, the outer limit to the H⁺ region is defined by a hydrogen ionization front. In this case the boundary of the cloud corresponds to the transition from ionized to neutral phase. In the following we will use ionisation bounded models.

Hydrogen gas density (n_H)

The density of the gas cloud is defined in terms of the hydrogen density. The total hydrogen density is defined as the sum of all protons in the atomic, ionic and molecular forms.

²The covering factor is the fraction of the radiation field emitted by the central object which actually strikes nebular gas.

The hydrogen density is given by:

$$n_H = n(H^0) + n(H^+) + 2n(H_2) + \sum_{other} n(H_{other})[cm^{-3}], \quad (2.1)$$

where $n(H_{other})$ represents Hydrogen in all other hydrogen-bearing molecules. We compute models for hydrogen densities of the ionized gas, spanning logarithmic values from 0 to 5 in steps of 1.0 dex corresponding roughly to the observed values of electron densities in extragalactic HII regions and star-forming galaxies (Castaneda et al., 1992).

Also, we computed both constant density and constant pressure models.

We used constant density throughout the gas cloud, considering that equ.2.1 is constant. In the case of constant pressure, as the model proceeds through consecutive zones of the cloud, it keeps the pressure constant while density can vary. (Byler et al., 2017) compared cloudy models with a constant density against models computed at constant pressure and found that the results do not change by more than a few percent, with the effect being more important in other plasma simulations codes such as mappings-III (Groves et al., 2004), which is a pressure-based photoionization code. Density is a fundamental parameter in Cloudy simulations whereas for Mappings-III is the pressure.

Ionisation parameter(U)

The ionization parameter (U) is defined as the ratio of ionizing photon density to hydrogen density:

$$U = \frac{Q(H)}{4\pi R_{in}^2 n_H c}, \quad (2.2)$$

where $Q(H)$ is the flux of ionizing photons striking the illuminated face of the cloud³, n_H is the hydrogen gas density, R_{in} is the inner radius of the cloud and c is speed of light. We computed models for values of $\log U$ in the range between -4.0 to 0.0, in steps of 0.5 dex.

Dust Grains

Grains (e.g. graphite, silicates) are a fundamental constituent of the ISM of galaxies where heavy elements produced by nucleosynthesis in the interior of stars can produce solid particles. The dust absorbs ionizing, UV and optical photons and re-emits the absorbed energy as IR photons. At high redshift, galaxies have young stellar population that produce and expel the dust grains thus enriching the Universe with higher dust quantities, which increase the dust to gas ratio with time (Dunne et al., 2003). We ran Cloudy simulation both with and without grains.

Cosmic Microwave Background (CMB)

The cosmic microwave background (CMB) may affect line emissivities across the spectrum (Chatzikos et al., 2013) even though these effects are more sensitive at longer wavelengths. As we will not consider wavelengths larger than 8000Å, we do not consider it in our CLOUDY simulations.

³in a Strömgren sphere, this would be a radius of the ionised sphere

Stellar population synthesis libraries

One of the key parameter in any consistent photoionization calculation of the irradiated medium is the broad band spectral energy distribution (SED) of the ionizing source. The shape of the SED affects the ionization and thermal structure of the photoionized gas. The incident radiation field is the external radiation field emitted by the central object that strikes the illuminated face of the cloud. It is specified in the commands that set up the calculation. The incident field is the only energy source for the cloud. The radiation field can be created using a black body, a power law, or other SEDs, such as built-in SEDs or user-defined SEDs. The spectral energy distribution (SED) of the incident radiation field should be chosen between low energy and high energy (Ryd). The low-energy region is essential for Compton cooling, photoionization from excited states of the elements, free-free heating, H- heating, and grain heating. The high-energy portion is crucial for secondary ionization, Compton heating, and pair production. Energies greater than 100 MeV are not generally important since the Klein - Nishina electron-scattering cross section ⁴ is negligible. An intensity of zero will be assumed for missing portions of the incident radiation field.

The shape of ionising radiation field produced by a star cluster depends on the age of the stellar population and on its metallicity. We used the Binary Population and Spectral Synthesis (BPASS) synthesis code (Eldridge, Stanway, 2012), which includes binary stars and has a range of values of both stellar ages and stellar metallicities. We consider a wide range of ages (3, 5, 8, 10, 20 Myrs) and logarithmic stellar metallicities (-3.6 , -2.6 , and -1.6). BPASS is based on a custom stellar evolution model code, first discussed in (Eldridge et al., 2008). The structure, temperature and luminosity of both individual stars and interacting binaries are followed through their evolutionary history, carefully accounting for the effects of mass and angular momentum transfer. The original BPASS prescription for spectral synthesis of stellar populations from individual stellar models was described in (Eldridge, Stanway, 2012). They began to investigate the affects of binary evolution on the emitted spectra of stellar populations in their BPASS models, showing that interacting binaries cause a population of stars to appear bluer at an older age than predicted by single-star models. At low metallicities interacting binary stars produce a modified ionizing photon output and may help to reproduce the observed high $[\text{OIII}]\lambda 5007/H\beta$ emission line ratios in the sub-solar, low- mass star-forming galaxies of the distant universe (Stanway et al., 2015) , as well as results seen in more local HII regions (Zhang et al., 2015). Fig.2.3 shows the incident radiation predicted by a stellar populations of different stellar metallicity Z_* at the different stellar ages.

Chemical Abundances

The chemical composition of the gas used in this study was adapted from the default CLOUDY chemical composition. The abundances command can be used to specify the abundances of all elements as a series of numbers. Abundances for all active elements must be specified. All the values used to scale the elements were given in log units and they are absolute values, i.e. they are directly related to hydrogen. Elements can be turned off with the *elements off* command. The composition can be specified for each element separately. We consider abundances GASS10 command by (Grevesse et al., 2010).

⁴The Klein–Nishina formula gives the differential cross section of photons scattered from a single free electron, calculated in the lowest order of quantum electrodynamics

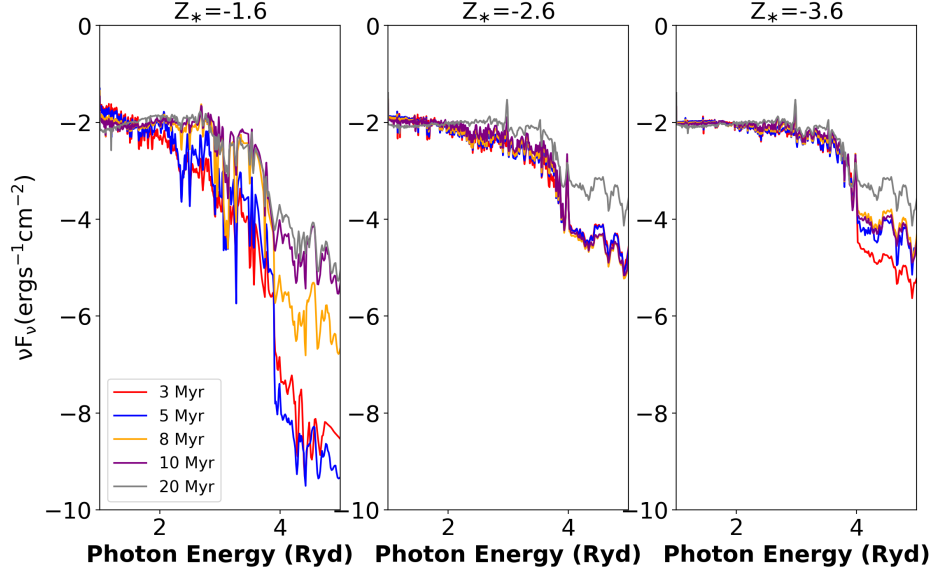


Figure 2.3. The total incident radiation predicted by different logarithmic stellar metallicity $Z_* = -1.6, -2.6,$ and -3.6 at the different stellar ages 3, 5, 8, 10, 20 Myr.

Several studies at metallicity $\log(O/H) + 12 \leq 8.3$ in HII regions of dwarf galaxies revealed that N/O is independent of O/H, implying a primary origin of nitrogen (Thuan et al., 1995). At even lower metallicity, for example the H II regions of blue compact dwarf galaxies, with $\log(O/H) + 12 \leq 7.6$, the scatter in the N/O values is very low. Since the scatter values is commonly attributed to the different production channels, the low observed scatter suggests that nitrogen production mainly occurs in massive stars (Izotov, Thuan, 1999a). With decreasing metallicity, it is expected that massive stars produce less nitrogen and the low-metallicity plateau reflects the assumption of this primary production by massive stars (e.g. (Vincenzo et al., 2016)). At higher metallicities the secondary production of nitrogen increases as the metallicity increases, increasing also the nitrogen abundance. To take into account such effects we used an the analytic function from SDSSIV-MaNGA sample (Belfiore et al., 2015) which can be related to that of oxygen through the expression:

$$N/O = -1.5, \text{ for } 12 + \log(O/H) < 8.3, \quad (2.3)$$

and

$$N/O = -1.5 + (0.7/0.5) * (12 + \log(O/H) - 8.3), \text{ for } 12 + \log(O/H) > 8.3. \quad (2.4)$$

Stopping Criteria

Our calculations were stopped when an effective temperature of 3000 K was reached. UV and optical emission lines from ionized gas are generally formed in a gas with higher temperature, so this choice of stopping criterion does not affect the resulting line emission.

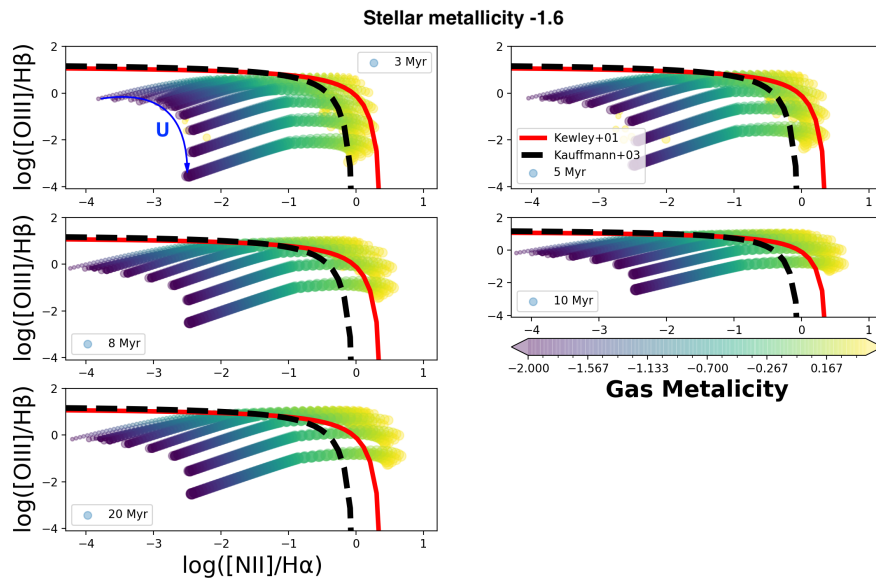


Figure 2.4. The BPT diagnostic diagram (Baldwin et al., 1981) in a specific stellar metallicity, and a wide range of stellar ages. It is color coded with gas-phase metallicity (Z). The blue arrow shows the variation of ionisation parameter (U). The solid red line and the dashed black line show the theoretical and observational separations between starforming galaxies and active galactic nuclei according to the (Kewley et al., 2001) and (Kauffmann et al., 2003) criteria, respectively.

PyCloudy

PyCloudy (Morisset, 2013) is a python library used to manage Cloudy inputs and outputs. It allows to define structures to run a Cloudy model and extract the results afterwards. It is extremely useful to compute grids of models, running Cloudy in parallel.

2.1.2 Example of Model creation

Fig.2.4 shows the distribution of our simulated models in the $[\text{OIII}]\lambda 5007/\text{H}\beta$ versus $[\text{NII}]\lambda 6567/\text{H}\alpha$ BPT diagram (Baldwin et al., 1981) together with the boundary lines between star-forming galaxies and active galactic nuclei defined by (Kewley et al., 2001). The demarcation line by (Kewley et al., 2001), solid red line, is a theoretical upper limit on the location of star-forming galaxies in this diagram, obtained using a combination of photoionization and stellar population synthesis models. (Kauffmann et al., 2003) (dotted black line) have revised the boundary line on the basis of the observational evidence that star-forming galaxies and active galactic nuclei are distributed along two separated sequences. It yields a conservative star-forming galaxy selection.

The emission lines of different species probe different zones of a nebula because they have different ionization potentials and different critical densities. Fig2.5 shows the oxygen ionisation fractions in different ionic species for a typical model. Higher ionisation species, such as O^{++} trace regions of high ionization, close to the ionizing source. The O emission lines trace the outer edge of the nebula, where the gas is only partially ionized. These emission lines, such as $[\text{OI}]\lambda 6300$, can directly introduce a kind of transition in Ionised

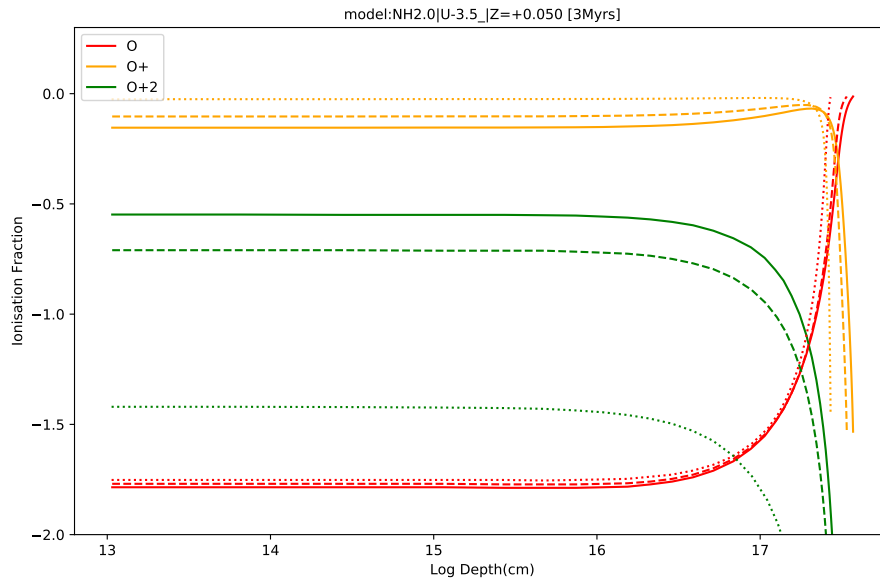


Figure 2.5. Example models of the ionization structure in Cloudy output for constant pressure with $n_H = 2$, $U = -3.5$, and gas phase metallicity $12 + \log(O/H) = 9.1$. Coloured curves correspond to the ionization fractions of commonly observed emission-lines of oxygen families as a function of depth (log scale). Solid, dashed, and dotted lines demonstrate $-3.$, $-2.$, and -1.6 stellar metallicity, respectively.

bounded situation. Ionisation fraction as a function of radius (depth) in clouds provide intensive information about ionisation state of different elements.

Chapter 3

A new multiple cloud approach to determine metallicity

There are broadly two kind of approaches in photoionization modelling of starforming galaxies and HII regions. One is based on single cloud, constant pressure models as in the work by Dopita, Kewley and collaborators with the code MAPPINGS. The other is based on the combination of different single cloud constant density models through an assumed weighting function: this is for instance the case of the so-called LOC models by Baldwin, Ferland and collaborators with the code CLOUDY or the case of the models by Netzer and collaborators with the code ION. The former approach is extensively used in the analysis of galaxy spectra and in the determination of abundances, while the latter approaches are mostly used in the analysis of the emission lines from the Broad Line Regions of Active Galactic Nuclei. These models are successful in reproducing the general emission line properties of the populations of galaxies and AGN but they struggle in reproducing the emission line spectra of single objects: in general the models fail to reproduce the observed wide range of excitation which is manifested by the existence of strong emission lines from different ionization stages like $[\text{OIII}]\lambda 5007$, $[\text{OII}]\lambda 3727$ and $[\text{OI}]\lambda 6300$. Here we present a new approach at photoionization modelling which builds upon a grid of single clouds but, at variance with LOC models, combines the single models with a weighting function which is determined from the observations, not assumed *a-priori*.

We present a new approach to modelling emission lines from photoionized gas which allows to reproduce observed line ratios from a wide range of ionization and with an accuracy to better than 10%, and whose main application is the accurate determination of gas metallicity. As in previous works, our approach is based on the weighted combination of multiple single cloud photoionization models but novelty of our approach is in the computation of the weights which are free parameters of the fit and are therefore set by the observations.

We show that a critical point for our modelling is to allow for different abundances for elements like N and S than those used in the photoionisation calculations: not accounting for those abundance variations can significantly affect the quality of the fit and the estimated gas metallicity. We will also show that our approach provide a significant improvement compared to the single cloud, constant pressure models commonly used in the literature. We have applied our model to the HII regions from the samples by Zurita et al. (2021) and from the CHAOS project. Using spectra of HII regions where between 10 and 20 emission lines

(including several auroral lines) are detected with high signal to noise we will show that all lines are reproduced by the model to better than 10%. In particular the model is able to reproduce also the simultaneously [OI], [OII], [OIII] and [SII], [SIII] emission lines which, to our knowledge, is an unprecedented result.

Finally, we have shown that the gas metallicities estimated with our models in HII regions of the Milky Way are in better agreement with the stellar metallicities than the estimates based on the T_e -method. Overall, our method provide a new accurate tool to estimate the metallicity and the physical conditions of the ionized gas. It can be applied in many different science cases and wherever there are emission lines from photoionized gas.

3.1 Single cloud models

More in details, a single cloud model is described by a slab of gas in plane-parallel or spherical symmetry ionised by a central source. A single cloud model therefore is defined by:

- the spectrum of the ionizing continuum;
- the ionization parameter $U = Q(\text{H})/(4\pi r_{in}^2 c n_H)$ where $Q(\text{H})$ is the rate of ionizing photons, r_{in} is the radial distance of the illuminated face of the cloud from the ionizing source and n_H is the density of Hydrogen atoms;
- the abundances of all the elements;
- the hydrogen density n_H at the illuminated face of the cloud;
- whether the cloud is constant pressure or constant density;
- whether the cloud has dust, and what are its properties and abundance
- the assumption of stationary equilibrium, i.e. no time evolution.

The model is integrated starting from the illuminated face of the cloud, numerically solving the equations of ionization equilibrium for all ions, the energy balance equation and the radiative transfer equation; all other relevant physical processes are also considered. The model predicts, among other things, the fluxes or luminosities of all the transitions considered which can then be compared with observations. The metallicity of the model which provides the best match is then the estimated gas metallicity.

The ionization level of the gas at a given point in the cloud is set by the value of the ionization parameter at that point, i.e. computed from $Q(\text{H})$ and n_H at r , where r is the distance from the ionizing source. This is the reason why single cloud constant pressure models perform better than constant density ones: with increasing r , the constant pressure associated with decreasing temperature within the cloud causes an increase in density and a corresponding decrease of U which is larger with respect to constant density models, allowing a better match for the observed emission lines from different ionization stages.

In order to provide a better match to the observed emission lines, combinations of single cloud models have been considered. One notable example is that of *Locally Optimally-emitting Clouds* or LOC models. Here a grid of single clouds in $\Phi(\text{H})$ and n_H is computed – $\Phi(\text{H}) = Q(\text{H})/(4\pi r_{in}^2)$ is the ionizing photon flux – and the emission lines predicted by the

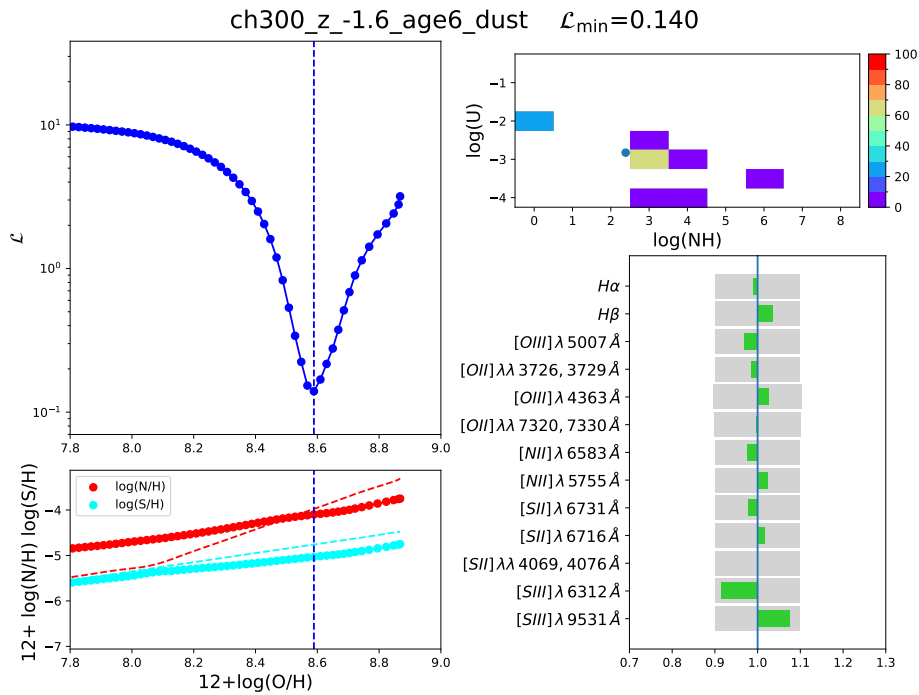


Figure 3.1. Variation of the loss function \mathcal{L} as a function of metallicity for the emission line spectrum of the test HII region. The blue dots/line represent the new multicloud model presented here, while the orange dots/line represent the case of single cloud, constant pressure models (section .). The red vertical dashed lines represent the metallicity of the model with the minimum value of the loss function \mathcal{L} . Middle: ratios of \mathcal{L} values from single cloud and multiple models, compared with \mathcal{L} values of multiple models. All HII regions have [OIII]4363 and [NII]5755 detected; the red points outline the HII regions where all 5 auroral lines have been detected with $S/N > 5$

single-cloud models are combined with a weighting function which is usually proportional to $\Phi(H)^{-\alpha} n_H^{-\beta}$, with α and β two slopes of the order of 1 which can be free parameters of the model. As in the case of single cloud models, the metallicity of the model which provides the best match is then the estimated gas metallicity. A different approach, mostly applied to AGN, assumes that the clouds are radiation or magnetic pressure confined and that their covering factor varies as a power law of distance r from the ionizing source, resulting in n_H and U which vary similarly as a power law of r (Netzer (2020)).

3.2 New multiple cloud models

The luminosity of an emission line l from ion X^{+i} either from recombination or from collisional excitation can be written as

$$L_l(X^{+i})_{obs} = \int_V N_e N(X^{+i}) J_l(X^{+i}, T_e) dV \quad (3.1)$$

where V is the volume of the ionized gas, N_e and $N(X^{+i})$ are the electron and ion densities, and T_e is the electron temperature. N and T are physical quantities which depends on the

position within the volume, however the luminosity does not depend on the detailed density and temperature distribution of the gas but on their properly weighted average values over the entire gas volume. Therefore to reproduce the observed line luminosity, any model must have the correct volume, average density and temperature of the X^{+i} region regardless of whether the spatial distribution of gas physical properties matches the real one. Therefore the observed line luminosity can be reproduced with a combination of many different models regardless of whether their detailed spatial distribution is a match for the real clouds:

$$L_l(X^{+i})_{mod} = \sum_j w_j L_l(X^{+i})_{mod,j} \quad (3.2)$$

$$= \sum_j w_j \int_{V_j} N_e N(X^{+i}) J_l(X^{+i}, T_e) dV \quad (3.3)$$

where $L_l(X^{+i})_{mod,j}$ is a set of *simple*, single cloud photoionization model which can be considered as the basic building blocks of the model. The weights w_j can either be assumed (like in the LOC models) or can be left as free parameters and determined from fitting the observed lines.

The main assumption here is that if a model is able to accurately reproduce the luminosity of many different emission lines from a few different ions, then it has the correct combinations of volume, average density and temperature for each ion, regardless on their real spatial distribution. The fitting procedure is as follows. We consider a grid of single clouds with constant density or pressure characterised by:

- the spectrum of the ionizing source
- the relative abundances of metal elements
- the gas metallicity, parameterised with the Oxygen metallicity
- a grid of ionization parameter and H density values

Each model of the grid predicts a set of emission line luminosities normalised such that, e.g., the luminosity of $H\beta$ is 100. All emission lines are then combined with weights which are found by minimising the loss function

$$\mathcal{L} = \frac{1}{n} \sum_{i=1}^n \left(\frac{L_l(X^{+i})_{obs} - L_l(X^{+i}; w_1, w_2, \dots, w_m)_{mod}}{\Delta L_l(X^{+i})_{obs}} \right)^2 \quad (3.4)$$

where n is the number of observed emission lines and m is the numbers of single cloud models. $\Delta L_l(X^{+i})_{obs}$ can be either the error on the observed emission line luminosity or the assumed *acceptable* discrepancy between the observed and model luminosities: in the following we will consider the maximum of the two. In order to allow for different relative abundances than those used in the computation of the single cloud models we rescale each set of model emission lines from a given element by a scaling factor which is a free parameter of the fit. The only element for which we do not apply such rescaling is oxygen since some of its forbidden emission lines provide the main cooling mechanism of the ionised zone and therefore the line luminosities are not trivially proportional to abundance. Considering, for

instance, observed lines from oxygen, nitrogen, and sulphur the loss function becomes

$$\mathcal{L} = \sum_{i=1}^{n_{O,H}} \left(\frac{L_l(X^{+i})_{obs} - L_l(X^{+i}; \mathbf{w})_{mod}}{\Delta L_l(X^{+i})_{obs}} \right)^2 \quad (3.5)$$

$$+ \sum_{i=1}^{n_N} \left(\frac{L_l(X^{+i})_{obs} - \mathcal{N} * L_l(X^{+i}; \mathbf{w})_{mod}}{\Delta L_l(X^{+i})_{obs}} \right)^2 \quad (3.6)$$

$$+ \sum_{i=1}^{n_S} \left(\frac{L_l(X^{+i})_{obs} - \mathcal{S} * L_l(X^{+i}; \mathbf{w})_{mod}}{\Delta L_l(X^{+i})_{obs}} \right)^2 \quad (3.7)$$

where $\mathbf{w} = (w_1, w_2, \dots, w_m)$ are the weights of the m single-cloud models, $n_{O,H}$ indicates that the sum is made on all H and O lines while n_N and n_S indicate summation on N and S lines respectively, and \mathcal{N} , \mathcal{S} are the scaling factors which are free parameters of the fit.

The values of the loss function can be approximately interpreted by assuming that the average relative disagreement between models and observations is ε and that for all emission lines and all ions

$$L_{l,obs} = L_{l,mod}(1 + \varepsilon_r \delta_l) \quad (3.8)$$

$$\Delta L_{l,obs} = \varepsilon_a L_{l,obs} \quad (3.9)$$

where δ_l are random numbers extracted from a normal distribution with zero average, and unit standard deviation. We have distinguished between the real relative disagreement ε_r and the acceptable disagreement ε_a . Therefore the loss function is given by

$$\mathcal{L} = \frac{1}{n} \sum_l \left(\frac{\varepsilon_r \delta_l}{\varepsilon_a (1 + \varepsilon_r \delta_l)} \right)^2 \quad (3.10)$$

For example, if the acceptable discrepancy is 10% ($\varepsilon_a = 0.1$) and the real average disagreement is also 10% ($\varepsilon_r = 0.1$), the loss function is $\mathcal{L} \simeq 1.1$. Conversely, if the real average disagreement is, e.g., $\varepsilon_r = 0.01, 0.05, 0.1, 0.11, 0.15, 0.2$ we obtain $\mathcal{L} \simeq 0.01, 0.25, 1.1, 1.36, 2.8, 6.3$, respectively.

The best fit model is found by minimizing the loss function \mathcal{L} : for a given set of scaling factors \mathcal{N} , \mathcal{S} , the weights (w_1, w_2, \dots, w_m) are found solving the non negative least square (NNLS) problem, in a similar way as in the pPXF python procedure by Cappellari, Emsellem (2004). Indeed, this model fitting is similar in principle to the fitting of the stellar continua of galaxies where many hundreds or thousands of stellar continuum templates are combined with non negative weights. Here the emission line *templates* from the single cloud models are combined with non-negative weights.

The single cloud models used in the following were computed using CLOUDY v17.03 (Ferland et al., 2017) with the following input parameters:

- BPASS continua (v2.3, Byrne et al. (2022); Stanway, Eldridge (2018)) for the binary star population, characterised by a Kroupa (2001) initial mass function from 0.1 to 300 M_\odot , $[\alpha/\text{Fe}] = +0.0$, metallicities solar and 0.1 solar, and ages (log yrs) 6, 6.3, 6.7 7.1, 8, 10 (for solar met.) and 6, 6.4, 6.7, 7.3, 8.3, 10.1 (for 0.1 solar met.)
- Abundances from -2 to +0.5 in steps for 0.1 dex relative to Solar; relative abundances were the Solar one from Grevesse et al. (2010); nitrogen is rescaled as a secondary

element with respect to oxygen as $[N/O] = -1.5 + 1.4 * ([O/H] - [O/H]_c)$ for $[O/H] \leq [O/H]_{crit}$ with $[O/H]_c = 8.3$ (see, eg., fig. 49 of Maiolino, Mannucci (2019b))

- Gas with and without dust; dust is included with the "grains ism Z log" where Z is the log of the abundance relative to solar; we then use the command "metals deplete" to take into account the depletion of metals into dust
- A grid in U and N_H with $\log U$ from -4 to -0.5 in steps of 0.5 dex and $\log N_H$ from 0 to 8 in steps of 1.0 dex
- All clouds with constant density

The model line luminosities relative to $H\beta$ are then log-linearly interpolated across metallicity in steps of 0.02 dex.

3.2.1 An example of a model fit

We describe the model by presenting an example of its application to the emission line fluxes of an HII region. The test HII region is extracted from the sample presented by Zurita et al. (2021) and has all the emission lines listed in the bottom right panel of figure 3.1 measured with $S/N > 5$; the results from the application of the model to the entire Zurita et al. (2021) sample will be presented in section 3.2.3. As mentioned in the previous section, the nitrogen lines ($[NII]\lambda 6583$, $[NII]\lambda 7555$) and sulphur lines ($[SIII]\lambda 9531$, $[SIII]\lambda 6312$, $[SII]\lambda 4069, 4076$, $[SII]\lambda 6716, 6731$) predicted by the model are rescaled by the factors \mathcal{N} and \mathcal{S} which are free parameters of the fit and which take into account that the relative N/O and S/O abundances may be different than those assumed in the photoionization calculations. The same rescaling is not applied to the oxygen lines ($[OIII]\lambda 5007$, $[OIII]\lambda 4363$, $[OII]\lambda 3726, 3729$, $[OII]\lambda 7320, 7330$) since they do not depend linearly from abundances. For any given ionizing continuum and gas metallicity, we find the weights w_i and \mathcal{N}, \mathcal{S} factors which minimise the loss function \mathcal{L} ; finally we consider the minimum \mathcal{L} across all metallicities considered.

The top left panel of figure 3.1 shows the variation of the loss function as a function of metallicity; the blue vertical dashed line represents the estimated model metallicity, which trivially corresponds to that of the model with the minimum value of \mathcal{L} . For all lines, we have adopted an *acceptable disagreement* of 10% ($\Delta L_i(X^{+i})_{obs} / L_i(X^{+i})_{obs} = 0.1$) when computing \mathcal{L} . The bottom left panel of figure 3.1 represent the Nitrogen and Sulphur metallicities provided as input in the CLOUDY simulations (dashed lines) and derived from the fit after correcting the input values with the \mathcal{N}, \mathcal{S} factors (filled circles). The values derived from the fit are well in agreement with the assumptions. The top right panel of figure 3.1 shows the weights of the single cloud models which were derived for the best fit: 7 single clouds out of 72 have non null weights, 2 of them account for 91% of the total and 3 for less than 1%. Using the weights, it is possible to compute the average density and ionization parameter of the clouds, which are identified by the blue filled circle in top right panel of figure 3.1. While it is not possible to affirm that the single clouds used in the model have a direct correspondence to the real N_H, U distribution, the average density and ionization parameter corresponds to the same values for the HII region.

In the bottom right panel of figure 3.1 we compare the model predictions with the observations: the x-axis represents the ratio between model and observed line fluxes and the

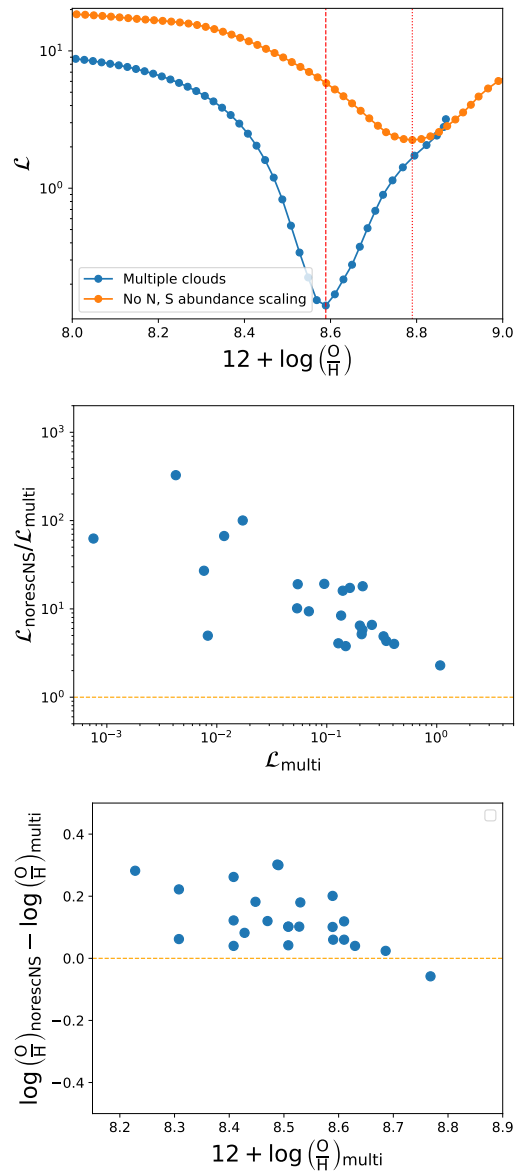


Figure 3.2. Comparison with models where N and S abundances are not rescaled compared to values used in photoionization calculations. Top: Variation of the loss function \mathcal{L} as a function of metallicity for the emission line spectrum of the test HII region. The blue dots/line represent the new multicloud model presented here (standard model), while the orange dots/line represent the case where N and S abundances are not rescaled (non-rescaled-NS models). The red vertical dashed lines represent the metallicity of the models with the minimum value of the loss function \mathcal{L} . Middle: ratios of \mathcal{L} minimum values from non-rescaled-NS models and standard models compared to the \mathcal{L} minimum values from standard models. Bottom: variation of abundances of non-rescaled-NS models with respect to standard models compared to the abundances of standard models.

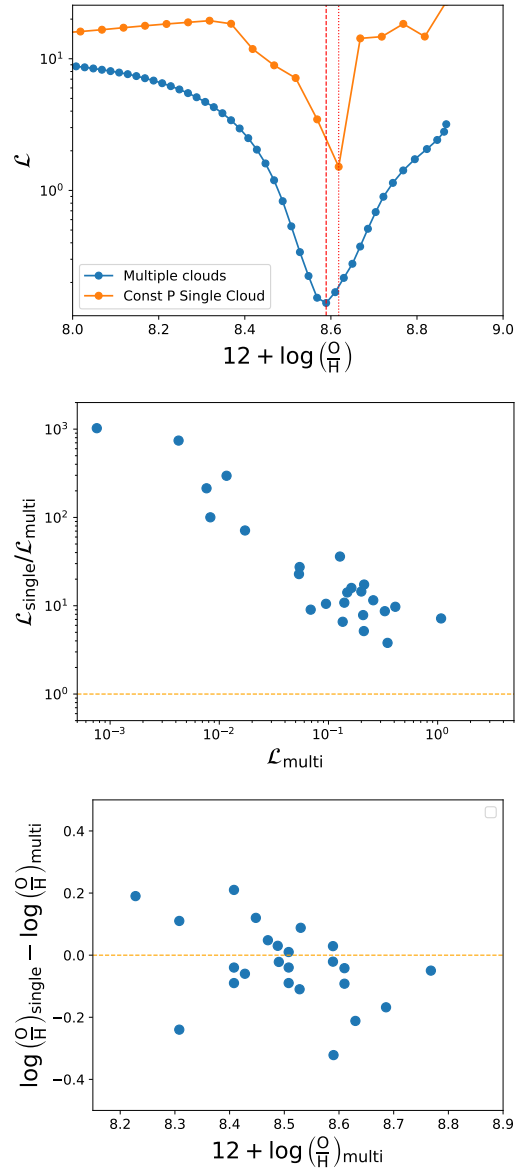


Figure 3.3. Comparison with single cloud, constant pressure models. Top-left: Variation of the loss function \mathcal{L} as a function of metallicity for the emission line spectrum of the test HII region. The blue dots/line represent the new multicloud model presented here. Top-right: Ionization parameter vs. number density of Hydrogen, color coded by weights, for the best models. Below-left: variation of abundances of single-P models with respect to standard models compared to the abundances of standard models. Below-right: The best models emission lines predicted over the observation.

length of the color bar indicate that value for the lines listed along the y-axis. The green color indicate a ratio which is within 0.9 and 1.1 (10% disagreement max), while the orange bar indicates values outside that range. The gray bar represent the $\pm 10\%$ disagreement. As previously discussed, a loss function value of 0.14 can be interpreted as an average disagreement of $\sim 4\%$ between observations and models which is visually confirmed in figure 3.1.

The model is able to reproduce a large number of emission lines from different ionization stages within 5%, with only the [SIII] lines reproduced with a 15% discrepancy: this is a definite improvement with respect to previous models. We also note that, although the [SIII] lines are the ones where the model perform the worst, still the agreement is very good when considering that [SIII] lines are usually so difficult to reproduce that problems with their atomic parameters have been suggested (Mingozzi et al., 2020a). Finally, the plot of the loss function in figure 3.1 presents a minimum so deep to require a logarithmic scale and indicates that the problem is well defined and not affected by degeneracies, as one might naively expect given the freedom in the choice of the weights.

Figure 3.2 outlines the importance of allowing for a scaling factor of the N and S abundances. The left panels shows how in the example model the minimum value of the \mathcal{L} increases by a factor $\simeq 15$. Overall, when fitting all the HII regions in the Zurita et al. (2021) sample (see section 3.2.3), minimum \mathcal{L} values increase by factors up to over 100 (center panel) and, while the same time, metallicities are overestimated by up to 0.3 dex (right panel). Clearly, rescaling of N and S abundances with respect to the ones assumed in the photoionization computations is extremely importance to improve the comparison of models and observations and the reliability of the metallicity estimates.

3.2.2 Comparison with constant-pressure single-cloud models

Figure 3.3 shows the large improvement of our multi-cloud approach with respect to the case of the single cloud constant pressure models which are used in the literature by many authors (e.g., Blanc et al. (2015); Dopita et al. (2016); Pérez-Montero et al. (2021) and references therein).

The left panel compares the \mathcal{L} curves obtained with the single (orange) and multi-cloud (blue) approach applied to the test HII region used before. Clearly the blue curve is the same as in figures 3.1 and 3.2. In order to obtain the orange curve, we have computed grids of constant pressure single cloud models following the same approach as before: for each given ionising continuum and gas metallicity, we have obtained a grid of models varying U and n_H . For each single cloud model in the grid we have then minimised the loss function \mathcal{L} finding the best scaling factors for N and S abundances. We have then considered the single cloud model with the lowest \mathcal{L} value. In the case of this particular example, the minimum \mathcal{L} value of our multi-cloud approach is more than a factor ten lower although the estimate gas metallicity is similar. The comparison between the orange curves in figures 3.1 and 3.2 shows that rescaling N and S abundances is crucial for having a low \mathcal{L} minimum value: indeed the single-cloud constant pressure model has a similar \mathcal{L}_{min} value as the multi-cloud model where the N and S abundances are those assumed in the photoionization calculations.

The center and right panels in the figure compare the minimum \mathcal{L} values and the oxygen abundances obtained by applying the two methods to the HII regions of the Zurita et al. (2021) sample: \mathcal{L} values obtained with the multi-cloud approach are more than a factor 10 lower, but the discrepancy can increase by several orders of magnitude. On the other hand

discrepancies in oxygen abundances are less severe and are up to 0.2 dex.

3.2.3 The sample by of HII regions by Zurita et al.

After presenting the model and its characteristics with a few selected examples we present its application to larger samples of emission line sources and in this paper we focus on HII regions. We consider the sample by Zurita et al. (2021), who collected the emission line fluxes of 2831 published HII regions from 51 nearby galaxies to study how the presence of bars affects metallicity gradients. The compiled line fluxes, reddening corrected and normalised to $H\beta$, include both bright emission lines ([OII] $\lambda\lambda$ 3726,3729, [OIII] $\lambda\lambda$ 4959,5007, [NII] $\lambda\lambda$ 6548,6583, $H\alpha$, [SII] $\lambda\lambda$ 6717,6731, [SIII] $\lambda\lambda$ 9069,9532) and auroral lines ([SII] $\lambda\lambda$ 4068,4076, [OIII] λ 4363, [NII] λ 5755, [SIII] λ 6312, and [OII] $\lambda\lambda$ 7320, 7330) when available.

For our analysis we selected only the sources where the fluxes of all bright and auroral emission lines are measured with $S/N > 5$ resulting in a sub sample of 24 HII regions. We then performed model fitting with both dusty and non-dusty clouds and with all the ionizing continua presented in section ??: each model set M is then characterised by the ionizing continuum and whether it is dusty or not, and consists of many U, N_H grids of single cloud models, each computed for a given metallicity Z . For each model set M we then find the minimum value of \mathcal{L} with varying Z , which we label $\mathcal{L}_{M,min}$. We then consider \mathcal{L}_{min} as the smallest of all $\mathcal{L}_{M,min}$ values. Finally, we consider acceptable all the models for which

$$\mathcal{L} \leq \mathcal{L}_{min} + 0.25 \quad (3.11)$$

following equation 3.10 the increase on average "disagreement" between model and observations depends on ε_a and on ε_r of the best model with $\mathcal{L} = \mathcal{L}_{min}$. For instance, given $\varepsilon_a = 0.1$, models with $\mathcal{L} = \mathcal{L}_{min} + 0.25$ have $\varepsilon = 0.05, 0.07, 0.11$ if the best models have $\varepsilon = 0.01, 0.05, 0.1$, respectively.

Figure 3.4a shows the distribution of the \mathcal{L}_{min} values for all the HII regions in the selected subsample. We distinguish the cases where, for each HII region, \mathcal{L}_{min} is found considering all models, only the models with dust, and those without. All models, regardless of whether they are dusty or not, reproduce the emission lines of all sources with $\mathcal{L}_{min} > 1.1$ except for one case with the dusty models where $\mathcal{L}_{min} = 1.66$. The distributions of \mathcal{L}_{min} values thus imply that our multi-cloud models are able to reproduce *all* emission lines to better than 10% an achievement which, to our knowledge, is unprecedented. It is also evident that there is no significant difference between using models with or without dust.

The performance of the model with each line is shown in figure 3.4, where we present the distributions of the ratios between observed and model line fluxes for all the selected HII regions and all the models with $\mathcal{L} \leq \mathcal{L}_{min} + 0.25$. The model is able to reproduce to within 10% both strong and auroral lines, from high ([OIII], [SIII]) and low excitation ([OII], [SII], [NII]) lines. In particular, the models are able to reproduce both [SII] and [SIII] lines at variance with what found by other authors (e.g. Mingozi et al (2020) Mingozi et al. (2020a)). In particular, [SIII] lines are so difficult to reproduce with photoionization models that problems with [SIII] atomic parameters have been suggested. In our case [SIII] lines are those for which we observe the largest discrepancies still, in only 13 and 35% of the cases the discrepancy is larger than 10% for [SIII] λ 9531 and [SIII] λ 6312 respectively.

We now compare models and observations by comparing the T_e -metallicities obtained by both observed and model line fluxes. We compute T_e -metallicities using the python package

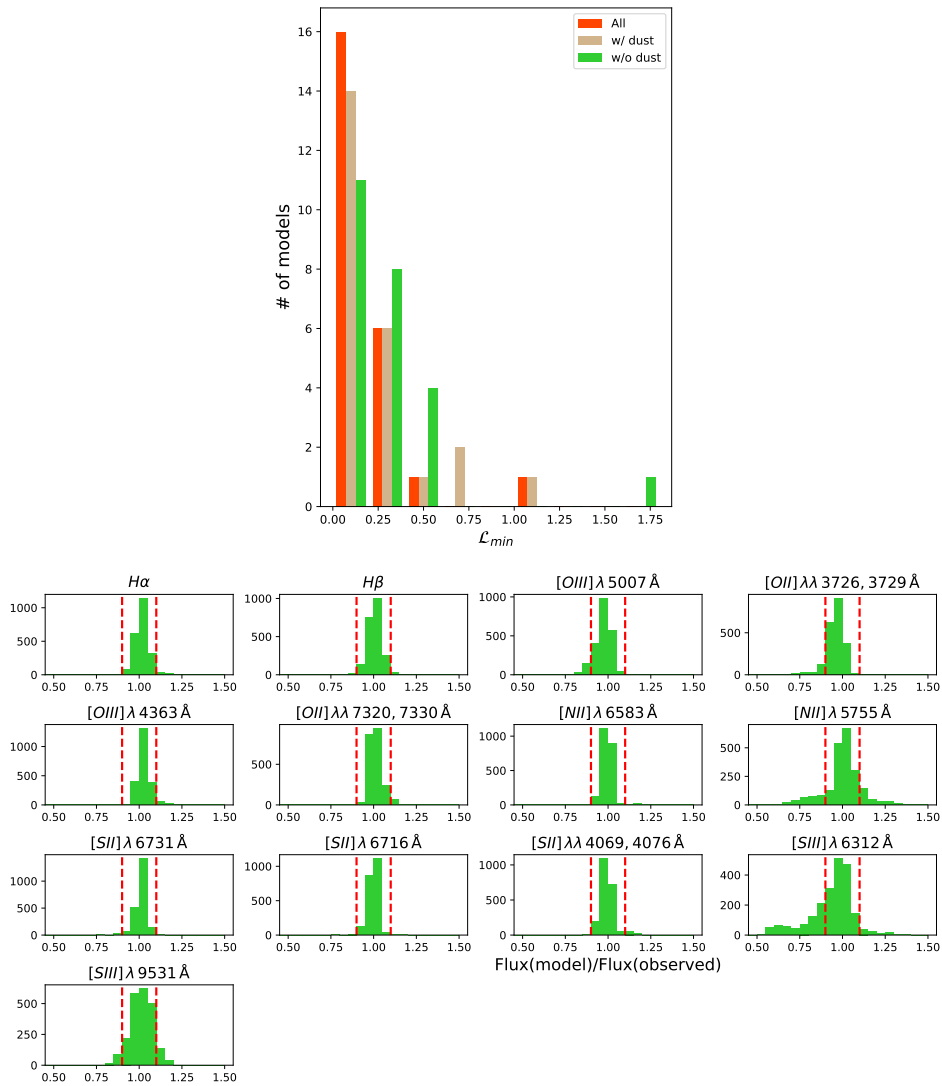


Figure 3.4. Top: distribution of \mathcal{L}_{min} values for the subsample of HII regions selected from Zurita et al. (2021). Bottom: distributions of the ratios between observed and model line fluxes for all the selected HII regions and all the models with $\mathcal{L} \leq \mathcal{L}_{min} + 0.25$.

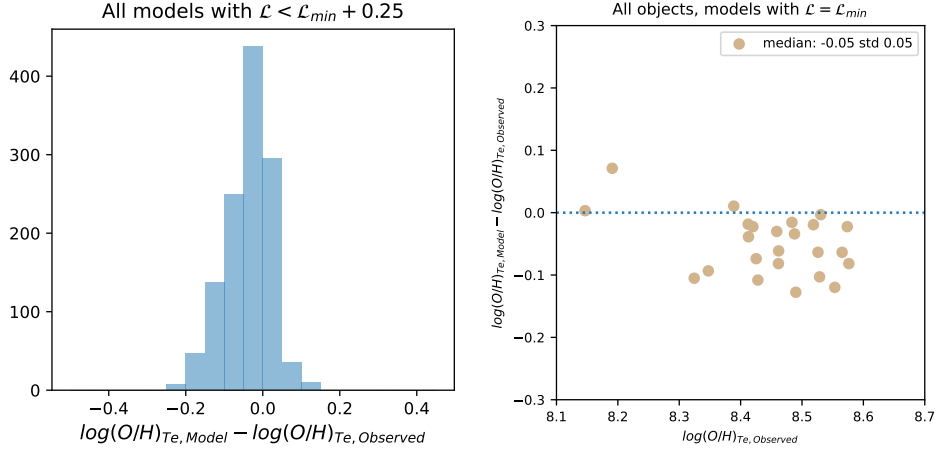


Figure 3.5. Comparison of T_e metallicities computed from observed and model line fluxes for the selected HII regions from the sample of Zurita et al. (2021).

pyneb (Luridiana et al., 2015a) where we selected the same sets of atomic parameters used in CLOUDY. We consider a two zone cloud where the density for both zones is given by $N_e(\text{SII})$, the temperature of the low ionization zone is given by $T_e(\text{NII})$ and that of the high ionization zone by $T_e(\text{OIII})$. The choice of $T_e(\text{NII})$ for the temperature of the low ionization zone is justified by the fact that $T_e(\text{OII})$ can lead to underestimate T_e -metallicities and is the same adopted by Zurita et al. (2021) (see also Pérez-Montero, Díaz (2003)). In particular the adopted procedure is the following.

- $T_e(\text{OIII})$ and $N_e(\text{SII})$ are computed simultaneously by combining the $[\text{OIII}]\lambda 5007/\lambda 4363$ and $[\text{SII}]\lambda 6731/\lambda 6716$ ratios with the `getCrossTemDen` pyneb procedure of pyneb;
- we used $N_e(\text{SII})$ to compute $T_e(\text{NII})$ from $[\text{NII}]\lambda 5755/\lambda 6584$, $T_e(\text{SII})$ from $[\text{SII}]\lambda 4069/\lambda 6720$, $T_e(\text{SIII})$ from $[\text{SIII}]\lambda 6312/\lambda 9531$ and $T_e(\text{OII})$ from $[\text{OII}]\lambda 7325/\lambda 3727$;
- we used $T_e(\text{OII})$ to compute $N_e(\text{OII})$ from $[\text{OII}]\lambda 3726/\lambda 3729$;
- $[\text{O}^+/\text{H}]$ and $[\text{O}^{+2}/\text{H}]$ abundance ratios are computed from $[\text{OII}]\lambda 3727/\text{H}\beta$, using $T_e(\text{NII})$, $N_e(\text{SII})$, and $[\text{OIII}]\lambda 5007/\text{H}\beta$ line ratios, using $T_e(\text{OIII})$, $N_e(\text{SII})$; $[\text{O}/\text{H}]$ is then the sum of the abundances of the two ions, neglecting any contribution from either neutral Oxygen or O^{+3} (e.g. Zurita et al. (2021))
- $[\text{N}/\text{O}]$ and $[\text{S}/\text{O}]$ abundance ratios are similarly computed from $[\text{NII}]\lambda 6584/[\text{OII}]\lambda 3727$ and $[\text{SII}]\lambda 6720/[\text{OII}]\lambda 3727$ line ratios

Errors are estimated with 100 Montecarlo realisations where the observed line sets are replicated 100 times by adding to line fluxes random numbers extracted from a Gaussian distribution with 0 mean and standard deviation equal to the observed error (i.e. the assumed discrepancy of $\varepsilon = 10\%$). Figure 3.5 (left) compares the T_e metallicities derived from the observed line fluxes and the ones predicted by the models: considering all acceptable models ($\mathcal{L} < \mathcal{L}_{min} + 0.25$) for all objects, the agreement is good as model and observed metallicities have a median difference, of -0.03 dex with a 0.06 dex standard deviation. Similarly, when considering only the best models ($\mathcal{L} = \mathcal{L}_{min}$) the median difference is -0.05 dex with a 0.05

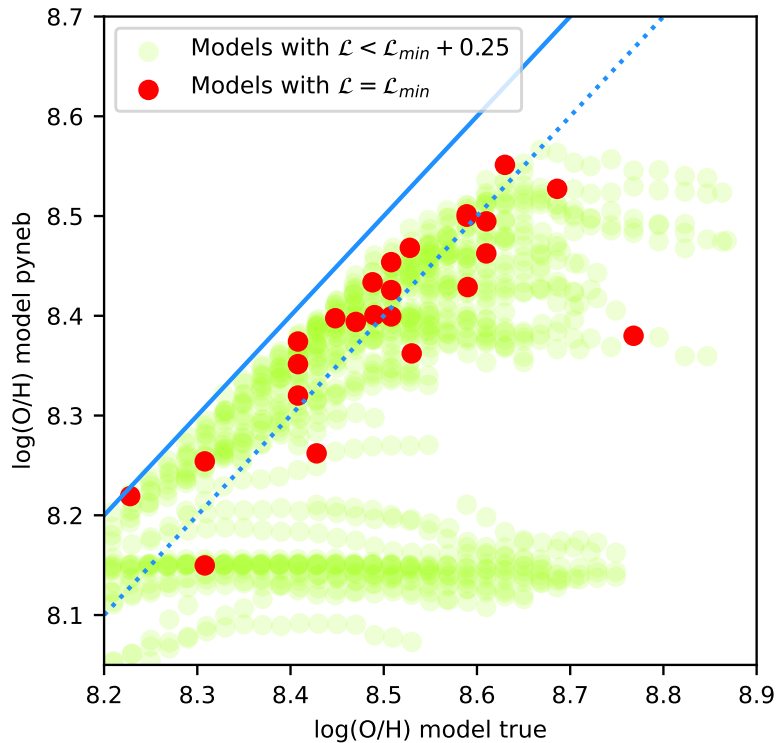


Figure 3.6. Comparison of model metallicities used in the photoionization calculations for the Zurita et al. (2021) sample and the T_e metallicities derived from the line fluxes predicted by the same models.

dex standard deviation. These values are consistent with the $<10\%$ discrepancy between model and observed line flux and provide a different measure of the (dis)agreement between models and observations.

Figure 3.6 presents the comparison between the metallicities used as input of the photoionization model calculations and the T_e metallicities derived from the line fluxes predicted by the models. This is not a comparison between models and observations, as it only involve model quantities, but provides an indication on the accuracy the T_e -method when applied to a system for which we know the true metallicity. The T_e metallicities are always smaller than the true values and can be discrepant up to ~ 0.5 dex: the median discrepancy and standard deviation of the difference between T_e and model metallicities considering only the best models are -0.09 and 0.07 dex, respectively. These values increase to -0.13 and 0.14 dex when considering all models with $\mathcal{L} < \mathcal{L}_{min} + 0.25$. We think that this disagreement is due to the simplified assumptions underlying the T_e method, confirming the findings by other authors (see, e.g., Esteban et al. (2014); Cameron et al. (2022)), and showing that with the computational capabilities and the quality and amount of data now available it is mandatory to adopt more accurate methods for abundance determinations from emission line ratios. A companion paper by Amiri et al. (2023) will address in more details these accuracy problems of the T_e method.

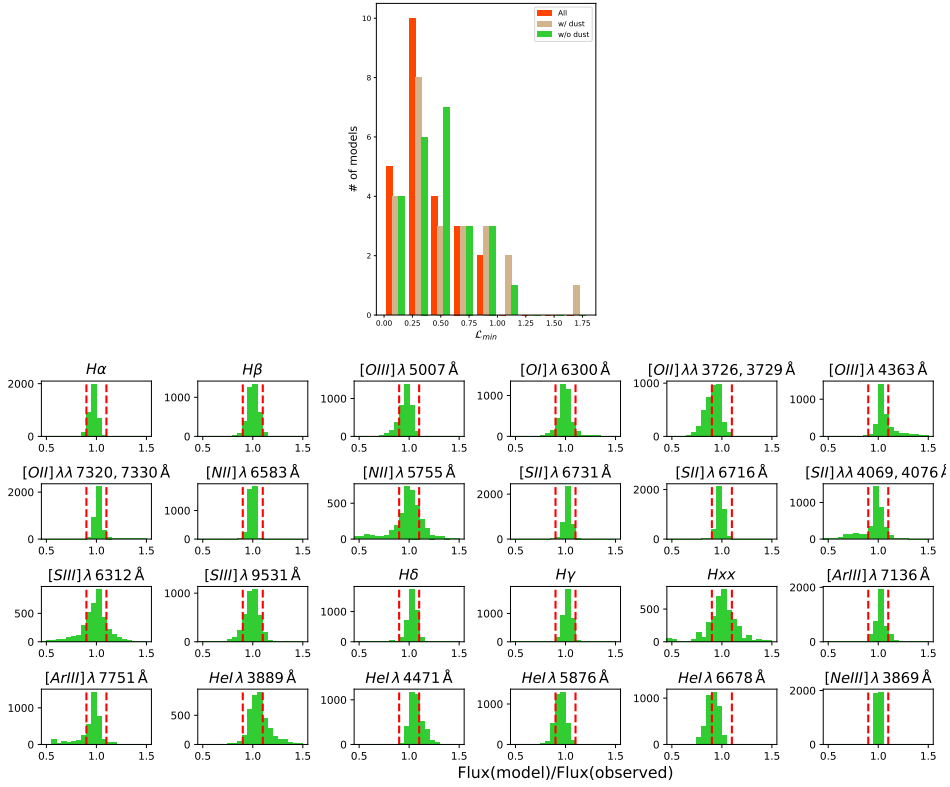


Figure 3.7. Top: distribution of \mathcal{L} values for the best/acceptable models of the HII regions from CHAOS sample. Bottom: distributions of the contributions to \mathcal{L} from each of the lines used for model fitting (the adopted error on line fluxes is the maximum between the observed error and 10%).

3.2.4 The sample by Berg et al.

We now apply the model to a sample of HII region with more homogeneous data, higher S/N and a larger number of emission lines.

We consider the HII regions of six galaxies from the CHEMICAL Abundances of Spirals (CHAOS) project (Berg et al. (2015a); Croxall et al. (2015a, 2016a); Berg et al. (2020); Rogers et al. (2021, 2022)) and we apply the same procedure followed in the previous section. At variance with the compilation by Zurita et al. (2021), the data now include 11 additional lines, including $[OI]\lambda 6300$ (see figure 3.7 for the list of lines). We select the HII regions with the same criterion used for the Zurita et al. (2021) sample, i.e. the auroral lines detected with $S/N > 5$.

Figure 3.7 and 3.8 confirm the results of the previous section: the \mathcal{L}_{\min} values of the best models are all lower than one (red bars in figure) indicating an average agreement between model and observed line fluxes better than 10%. All lines are well reproduced and in particular, the models are able to reproduce at the same time $[OI]$, $[OII]$ and $[OIII]$, as well as $[SII]$ and $[SIII]$, which is a significant improvement compared to previous works. Note that the $[NeIII]\lambda 3869$ line does not provide any constraint to the model since it is the

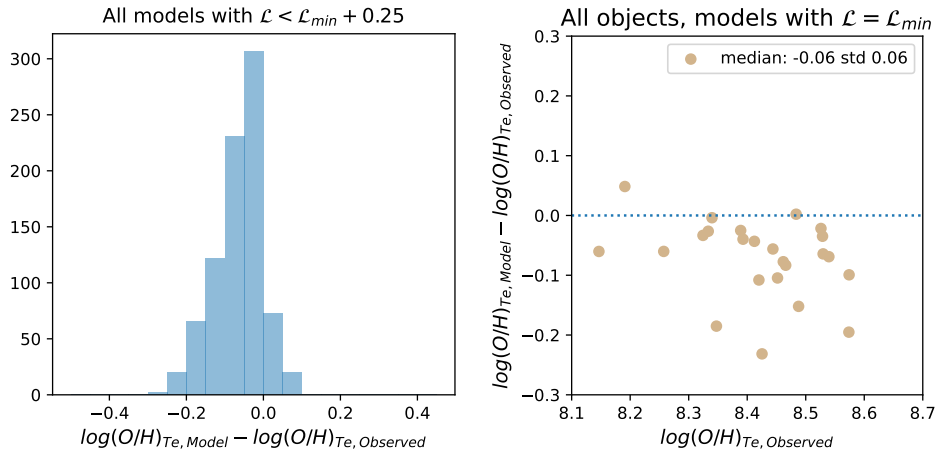


Figure 3.8. Comparison T_e metallicities computed from observed and model line fluxes for the selected HII regions from the CHAOS sample.

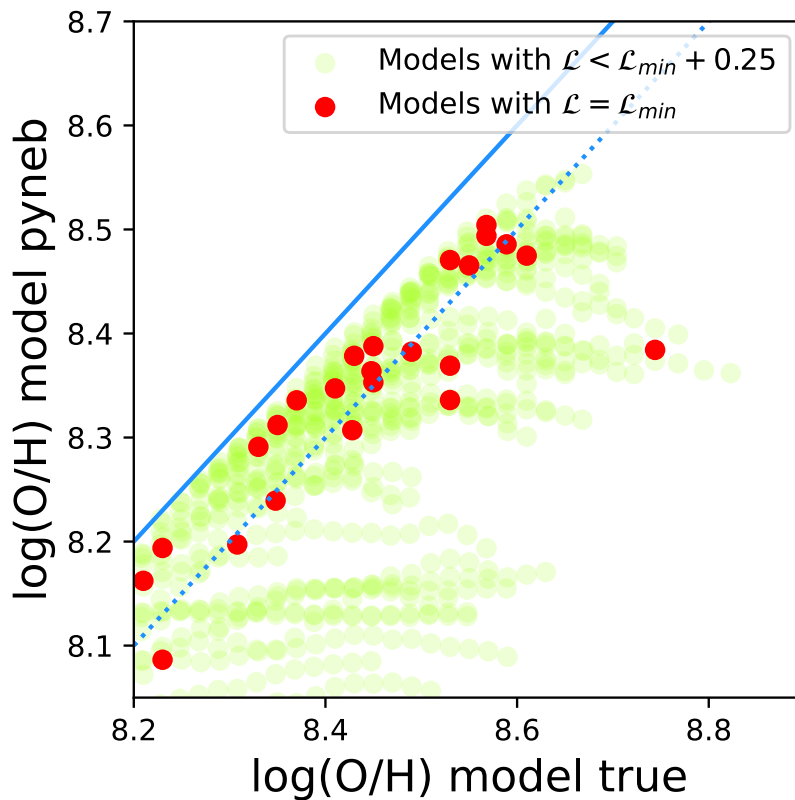


Figure 3.9. Comparison of model metallicities used in the photoionization calculations for the CHAOS sample and the T_e metallicities derived from the line fluxes predicted by the same models.

only Neon line, and it is used only to estimate Ne abundance. It is remarkable that when using only the emission lines from the Zurita et al. (2021) sample and $[\text{OI}]\lambda 6300$, the \mathcal{L}_{\min} values are all lower than 0.3.

We have estimated T_e metallicities as in the previous section and found that the agreement between estimates from observed and model line fluxes is similar to what found for the Zurita et al. (2021) sample (figure 3.8). Finally, we confirm as well the disagreement of up to 0.2 dex between the metallicities used in the photoionization model computations and the T_e metallicities derived from the line fluxes predicted by the same models (figure 3.9).

Mannucci et al. (2021) investigated the possible contribution of the Diffused Ionised Gas (DIG) which is often invoked to explain the differences between the spectra of HII regions in local galaxies and the total or kpc-scale spectra of star-forming galaxies when the flux ratios involving low-ionization emission lines are considered. Comparing single slit spectra of HII regions from CHAOS with those extracted with different aperture sizes from integral field spectra, they concluded that these differences are mostly ascribed to the smaller angular size of the slits with respect to the projected size of the HII regions. In principle, our model approach based on combining multiple clouds to reproduce the correct volume of gas occupied by any given ion X^{+i} with the correct T_e and N_e can naturally take into account both aperture effects and the contributions from regions with different physical properties like the DIG, however this issue will be addressed in a forthcoming paper.

3.2.5 Gas and stellar metallicities in the Milky Way

We present the last application of our method and its potentiality to solve the observed discrepancy between the metallicities of HII regions and those of the stars in our Galaxy.

Figure 4 of Esteban et al. (2022) summarises the discrepancy between the metallicities of HII regions in our Galaxy, derived from the application of the T_e -method to gas emission lines, and the stellar metallicities derived from B-type stars, Classical Cepheids and Open clusters. The latter are all consistent among themselves but are ~ 0.2 dex larger than HII region metallicities.

Such difference is not present when considering gas metallicities from recombination lines and constitutes the so-called abundance discrepancy problem, which is quite a common occurrence when comparing T_e and recombination-line-based metallicities. As mentioned by Esteban et al. (2022), such discrepancies might be related to temperature fluctuations which bias auroral lines towards the hotter parts of the HII regions providing higher than average temperatures and consequently lower abundances (Peimbert, 1967). Indeed this discrepancy disappears when correction for temperature fluctuations and ionization fractions are applied (Méndez-Delgado et al., 2022). Still corrections for temperature fluctuations are difficult to estimate and ionization corrections must be derived from photoionization models thus adding up additional assumptions and uncertainties to the T_e method.

We consider the HII regions from table 1 of (Méndez-Delgado et al., 2022) and estimate their metallicity by applying our method to the emission lines fluxes from Arellano-Córdova et al. (2020), 2021 and Zurita et al. (2021). Figure 3.10 shows the HII region metallicities plotted as a function of GAIA based galactocentric distances from Méndez-Delgado et al. (2022) and compare them with Cepheid metallicities from figure 1 of Mollá et al. (2019). The plot clearly shows how our model based metallicities are in better agreement with the stellar metallicities being on average lower by only 0.1 dex. It is important to note that these are pure gas metallicities which do not take into account the depletion of metals

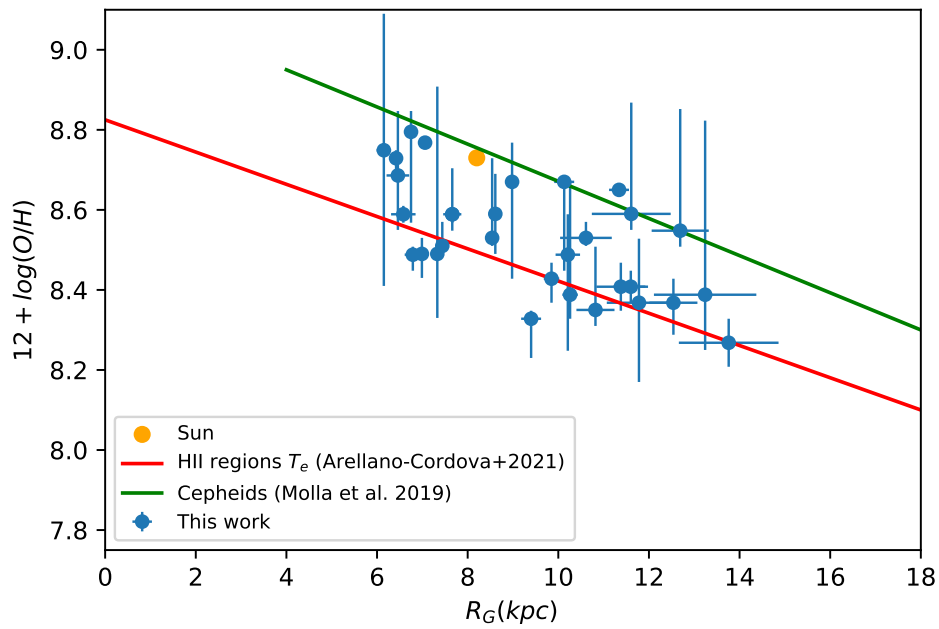


Figure 3.10. Comparison between our metallicity estimates of HII regions in our Galaxy (blue points with error bars) and the Cepheids metallicities from the compilation of Mollá et al. (2019) (green line). The red line represents the T_e metallicities of the same HII regions estimated without ionization or temperature fluctuations corrections.

into dust: indeed a 20% depletion of Oxygen can fully account for the residual difference thus explaining the abundance discrepancy without the use of temperature fluctuations or ionization corrections.

Chapter 4

Observation and flux measurements

The work described in this thesis leverages spectroscopic data from the Sloan Digital Sky Survey (SDSS) legacy survey. In the following sections, we make an overview on the instrumentation which provided the data analyzed in the subsequent chapters.

4.1 The Sloan Digital Sky Survey

The Sloan Digital Sky Survey (SDSS, (York et al., 2000)) provides one of the most impressive surveys in the astronomy. More than twenty years of operations, it captured images and spectra covering more than 35% of the sky, restructured our understanding of the Universe by addressing a wide range of different scientific fields, from low to high scale of structures. The data reduction and calibration are publicly released in a series of annual data releases, with both images and spectra, that can be downloaded by running queries in CasJob ¹.

The SDSS utilises a dedicated 2.5-m f/5 modified Ritchey-Chretien altitude-azimuth telescope placed at Apache Point Observatory, in south east New Mexico. The spectrograph operates by feeding an individual optical fibre of 3" diameter for each target through a hole drilled in an aluminum plate. The simultaneous use of two double spectrographs allowed to reach the desired spectral coverage of 3900-9100Å, while maintaining approximately a resolving power of $R=2000$. The original spectrograph was capable of recording 640 spectra simultaneously, while the updated spectrograph can record 1000 spectra at once. In its first five years of operations, the SDSS carried out deep, optical multi-band imaging (based on a photometric system of five filters, namely u,g,r,i and z) over 8000 square degrees. In this thesis, we use MPA/JHU ² catalogue. It is based on the Eighth SDSS Data Release (DR8)³. The Max Planck for Astrophysics (MPA) and Johns Hopkins University (JHU) researchers studied and catalogue galaxy properties for all DR8 galaxy spectra, based on the methods by Kauffmann et al. (2003); Brinchmann et al. (2004); Tremonti et al. (2004)

4.2 Sample Selection

As we want to investigate about metallicity, we need to cover a wide range of dynamical range of gas-phase metallicity from low to high values. Auroral lines which are needed for

¹skyserver.sdss.org/casjobs/

²www.sdss.org/dr12/spectro/galaxy_mpa_jhu/

³www.sdss3.org/dr8/

metallicity estimates are extremely dim and their detection is extremely hard. Therefore our data included low metallicity single galaxy spectra (section 4.2.2) from (Curti et al., 2019) and high metallicity stacked galaxy spectra (section 4.2.1) from (Curti et al., 2017) in order to be able to detect auroral lines. Galaxies were selected from the MPA/JHU catalog which includes data for 930000 entries. (Curti et al., 2017; Curti et al., 2019) considered only galaxies with redshifts in the range $0.027 < z < 0.25$, to ensure the appearance of both the $[\text{OII}]\lambda 3727$ emission line and the $[\text{OII}] \lambda\lambda 7320, 7330$ doublet within the useful spectral range of the SDSS spectrograph in wavelength ranges of 3800-9200Å. They also considered galaxies classified in the MPA/JHU as star forming, disregarding galaxies dominated by AGN contribution according to criteria for BPT- diagram classification demonstrated in Kauffmann et al. (2003), in order to preclude any influence on the emission line ratios that could cause spurious metallicity measurements. In the first work, they considered a Signal to Noise ratio(SNR) threshold of 5 on the $\text{H}\alpha$, $\text{H}\beta$, $[\text{OIII}]\lambda 5007$ and $[\text{OII}]\lambda 3727$ emission line fluxes. After applying these selection criteria the total number of galaxies in their sample was reduced to 118478.

4.2.1 Stacked galaxies

As our main purpose is investigating about gas-phase metallicity, we need to detect auroral line emission lines. These emission lines are not possible to detect in starforming galaxies with high gas-phase metallicity without stacking several hundreds of spectra. We then considered the sample of 62 stacked galaxy spectra from (Curti et al., 2017). Galaxies are stacked according to their values of emission lines reddening corrected $[\text{OII}]\lambda 3727/\text{H}\beta$ and $[\text{OIII}]\lambda 5007/\text{H}\beta$ flux ratios. This is based on the assumptions underlying the strong-line method for metallicity estimates: galaxies with the same values of those line ratios are supposed to have the same metallicity. Indeed, Curti et al. (2017) considered galaxies with simultaneously the same values of both $[\text{OII}]\lambda 3727/\text{H}\beta$ and $[\text{OIII}]\lambda 5007/\text{H}\beta$ have approximately the same oxygen abundance, as these two line ratios are proportionally connected to main ionization states of oxygen (individually applied as metallicity estimator) (Nagao et al., 2006b; Maiolino et al., 2008) (see Fig.4.1).

Furthermore, because of the physical link between ionization and gas-phase metallicity, their ratio $[\text{OIII}]/[\text{OII}]$ is sensitive to the ionization parameter and is also employed as an indicator of oxygen abundance, especially in metal-enriched galaxies. This indicates that a galaxy's position on the $[\text{OII}]\lambda 3727/\text{H}\beta$ - $[\text{OIII}]\lambda 5007/\text{H}\beta$ diagram is initially determined by its metal concentration and ionization characteristics.

The distribution of the chosen SDSS galaxies is depicted in the left panel of Fig.4.1 in the diagnostic diagram of $\log [\text{OII}]\lambda 3727/\text{H}\beta$ and $\log [\text{OIII}]\lambda 5007/\text{H}\beta$. For the $[\text{OII}]\lambda 5007/\text{H}\beta$ and $[\text{OIII}]\lambda 5007/\text{H}\beta$ indicators, Maiolino et al 2008 Maiolino et al. (2008) semi-empirical's calibration is over plotted in the aforementioned figure to better illustrate how the position on the two-dimensional diagram indicated by the combination of these line ratios represents a metallicity sequence.

Curti et al. (2017) used stacked spectra in bins of 0.1 dex of $\log [\text{OII}]\lambda 3727/\text{H}\beta$ and $\log [\text{OIII}]\lambda 5007/\text{H}\beta$. The main reason to select this step is based on a choice to keep high enough number of galaxies in bins to ensure auroral line detection.

Moreover, Curti et al. (2017) found evidence for $[\text{FeII}]$ contamination of the $[\text{OIII}]\lambda 4363$ auroral line flux. They have shown with increasing metallicity in stacks galaxy, we will have a contamination of $[\text{FeII}]\lambda 4360$. To avoid any contamination, we do not consider $[\text{OIII}]\lambda 4363$

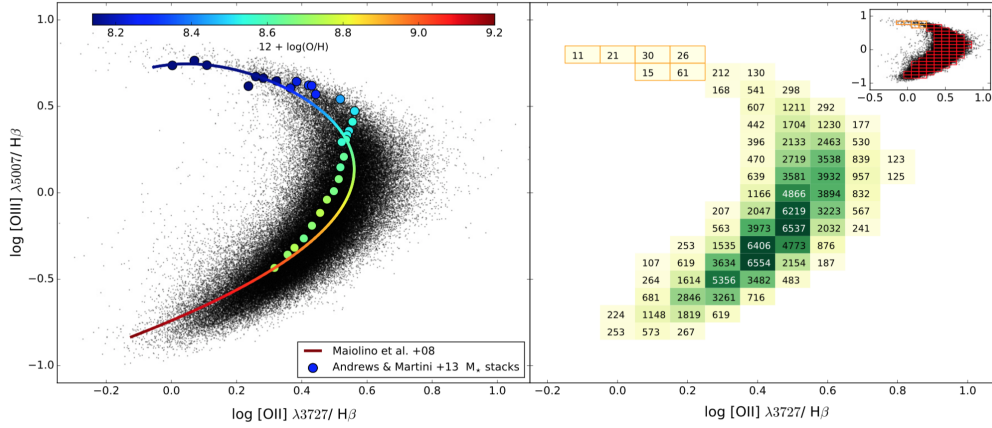


Figure 4.1. Stacking idea: the distribution of all galaxies which have been used in stacking procedures from Curti et al. (2017) in the $\log [OII] \lambda 3727 / H\beta$ - $\log [OIII] \lambda 5007 / H\beta$ diagram in the left panel. The curve demonstrates the combined calibrations for the $[OII] / H\beta$ and $[OIII] / H\beta$ metallicity indicators from Maiolino et al 2008 (Maiolino et al., 2008). Circle points and their direct metallicity measurement are from (Andrews, Martini, 2013), based on stacks in bins of stellar mass. Right Panel: Stacking grid for our sample of SDSS galaxies in the $\log [OII] \lambda 3727 / H\beta$ - $\log [OIII] \lambda 5007 / H\beta$ diagram from (Curti et al., 2017). It is color-coded by the number of galaxies included in it (for each bin) (Courtesy: Mirko Curti).

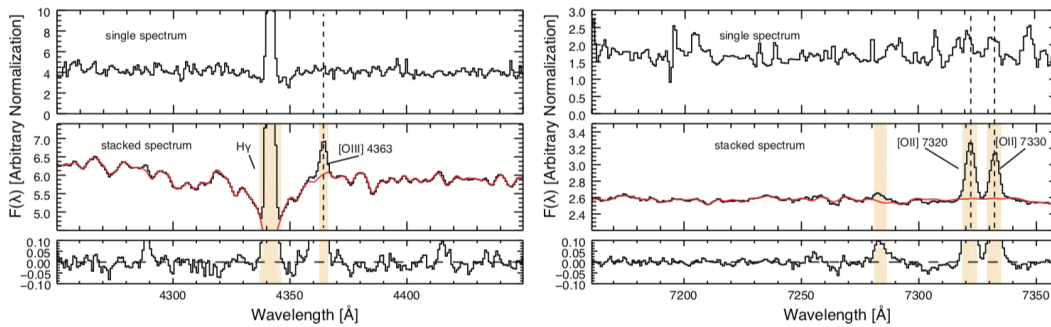


Figure 4.2. Fit and subtracted spectra for $[OIII] \lambda 4363$ auroral line (left panels) and $[OII] \lambda\lambda 7320, 7330$ auroral lines (right panels) respectively, for one of stack galaxies from Curti et al. (2017). For auroral lines, a single galaxy spectrum weakness is demonstrated in the upper panel for comparison, while the stacked spectrum is drawn in the middle one (Courtesy: Mirko Curti).

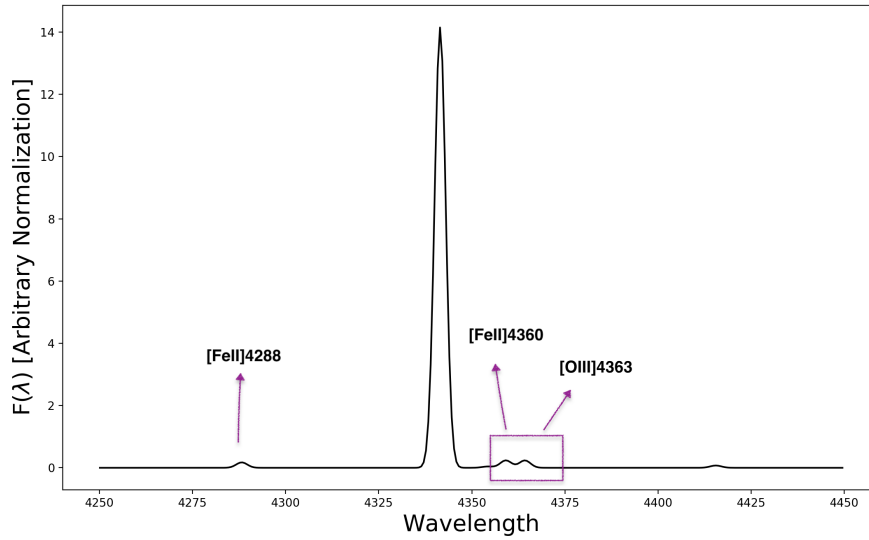


Figure 4.3. Galaxy stacks spectra for one of stacks galaxies at rich gas-phase metallicity, in the wavelength range 4250 - 4450Å. The contamination of the [OIII] λ 4363 with [FeII] λ 4360.

for those galaxies where the iron contamination is detected. To infer [OIII] λ 4363 flux for stacks, we rely on the relationship between the strong emission lines and the auroral line (Pilyugin et al., 2006a). This relation between auroral and nebular oxygen line fluxes, called ff relation, has been well known for HII regions of metallicity bigger than $12 + \log(O/H) \sim 8.25$ (see also Fig.4.3).

4.2.2 Single galaxies

To study the low-metallicity regime, we use a sample of 600 galaxies selected from SDSS selected by Curti et al. (2019). (Curti et al., 2019) applied a redshift selection of $z > 0.027$ to confirm the existence of the [OII] λ 3727 emission line. In this case, they are able to use this specific emission line to determine the metallicity of the sample while maintaining redshift consistency with the analysis performed (Curti et al., 2017). In contrast, a low redshift cut would mean that only the innermost sections of the SDSS fiber would be sampled, as 3" are equivalent to a projected physical distance of just near 1.6 kpc at $z = 0.027$. This would increase the amount of uncertainty when considering SFR aperture correction, but it would also make the metallicity measured within the fiber less indicative of the metallicity of the entire galaxy and more susceptible to metallicity gradients. In order to solve this issue, they limited the scope of their study to these galaxies with a coverage factor of at least 10%, as determined by the percentage of total light that enters the fibre. Additionally, they eliminated any galaxies with flags in their catalogues indicating inaccurate SFR estimators, including any with nonphysical aperture correction values of less than 1.

They have also applied a SNR threshold of 15 on the H α flux, in terms of SNR cuts on emission lines(for a detailed study (Mannucci et al., 2010)).

We additionally consider those galaxies with detected both [OII] λ 7319,7330 and

[OIII] λ 4363 auroral lines. With this criterion, we have a sample of 207 galaxies.

4.3 Stellar Continuum Subtraction and Line Flux Measurement

Since (Curti et al., 2017; Curti et al., 2019) do not provide measurements for all the lines that we need for our model fitting, we remeasured line fluxes both in stacked and single galaxy spectra. To measure the emission-line fluxes from both galaxy stacks and single galaxies, we fit spectra with a set of stellar population models to remove continuum emission. In particular, we use the penalised pixel-fitting (pPXF) method, Cappellari, Emsellem (2004) and fit the observed spectra using a combination of templates from the E-MILES stellar library (Vazdekis et al., 2016).

These templates cover the wavelength range 3525 - 7500Å with a constant spectral resolution of 2.50Å FWHM, similar to the SDSS spectral resolution. We employ the Padova stellar tracks (Girardi et al., 2000), considering a series of initial mass functions(IMF) such as Unimodal (UN), Bimodal (BI), Kroupa Universal (KU), Kroupa Revised (KB), Chabrier (CH) with a high-mass slope of 1.30 (Vazdekis et al., 1996), independent of age and total metallicity.

For two reasons, we prefer to do a new flux measurement, instead of utilizing (Kauffmann et al., 2003; Curti et al., 2017): 1) at variance with (Curti et al., 2017; Curti et al., 2019) with pPXF we can now simultaneously fit stellar continua and emission lines, obtaining more precise flux estimates; 2) in galaxy stacks, we additionally need to measure [OI] emission lines as they are one of the most significant emission lines that they are emitted by the partially ionized regions in HII regions and starforming galaxies, and [OII] auroral lines in single galaxies. These lines are not measured by Curti et al. (2017); Kauffmann et al. (2003); Curti et al. (2019), respectively. We fitted gas emission line fluxes in different narrower wavelength intervals.

We correct emission line fluxes for extinction caused by dust using the Balmer Decrement. In particular, we assume an intrinsic $\frac{H\alpha}{H\beta}$ ratio of 2.86, appropriate for case B recombination and a temperature of $T_e = 10^4 K$ and a density of 100 cm^{-3} . To measure the colour excess $E(B - V)$ we use the (O'Donnell, 1994) extinction law, with a typical $R(V)$ value of 3.1. We correct the flux of all emission lines for extinction recovering un-reddened fluxes for the sample of single SDSS galaxies.

In the case of stacks the extinction correction was performed prior to stacking by (Curti et al., 2017). Before creating the composite spectrum from galaxies belonging to the same bin, each individual spectrum has been corrected for reddening with a (Cardelli et al., 1989) extinction law and normalized to the extinction corrected $H\beta$. Then, each spectrum has been re-mapped onto a linear grid (3000-9200Å), with wavelength steps of $= 0.8\text{Å}$, and shifted at the same time to the rest frame to compensate for the intrinsic redshift of the sources. This procedure may cause a redistribution of the flux contained in a single input channel to more than one output channel; in order to take into account this effect, the incoming flux is weighted on the overlap area between the input and output channels.

Fig.4.4 shows the total results of the fit with using pPXF in the different wavelength ranges to detect different emission lines.

From Fig.4.5 to Fig.4.18 we show how we applied pPXF to our both single and stacks galaxy and did stellar subtraction, in different wavelengths.

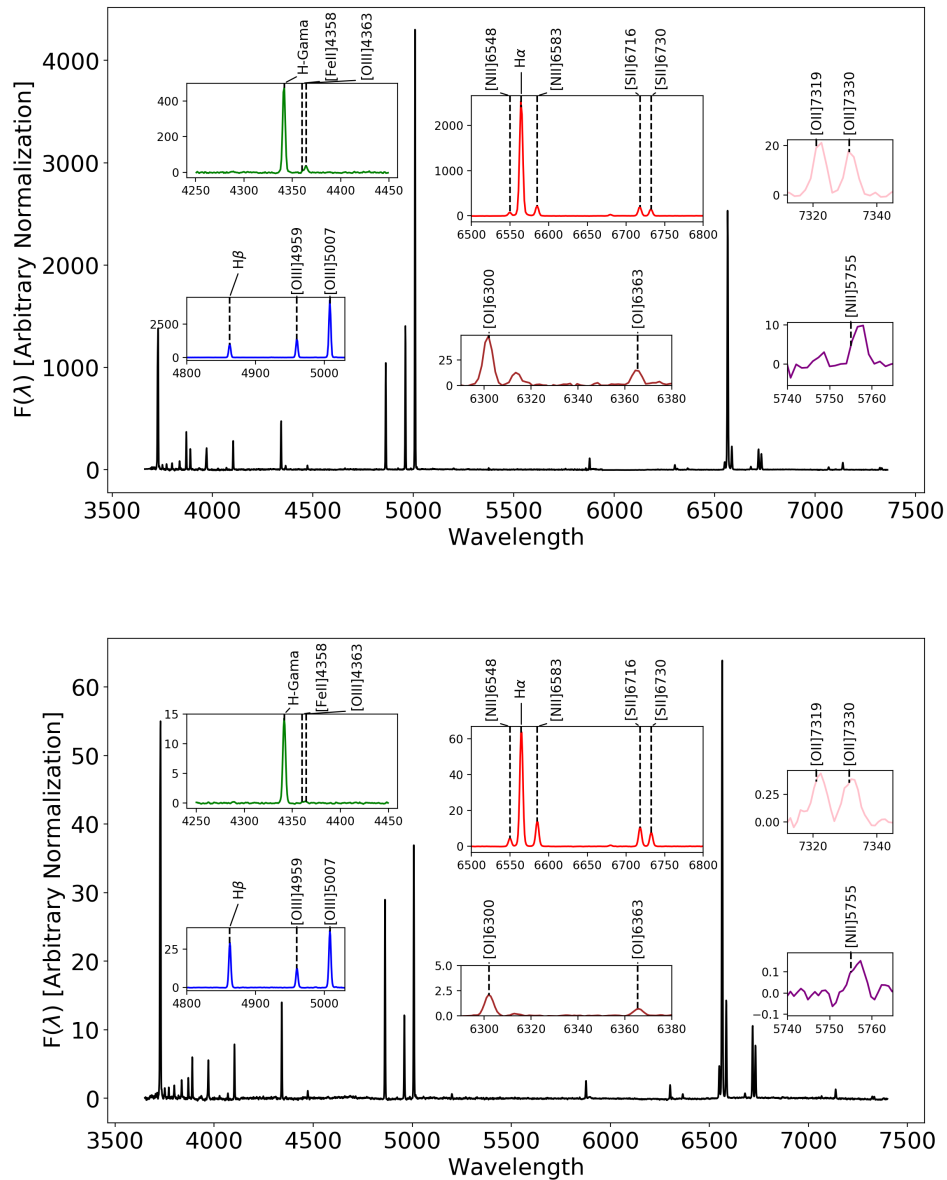


Figure 4.4. An example of the continuum-subtracted fitting to one of single galaxies (above) and one stack galaxy (below). Faint, temperature sensitive auroral lines $[\text{OIII}]\lambda 4363$, $[\text{OII}]\lambda 7319$, and $[\text{OII}]\lambda 7330$ necessary for direct abundance calculation are pointed out in green and pink color, respectively.

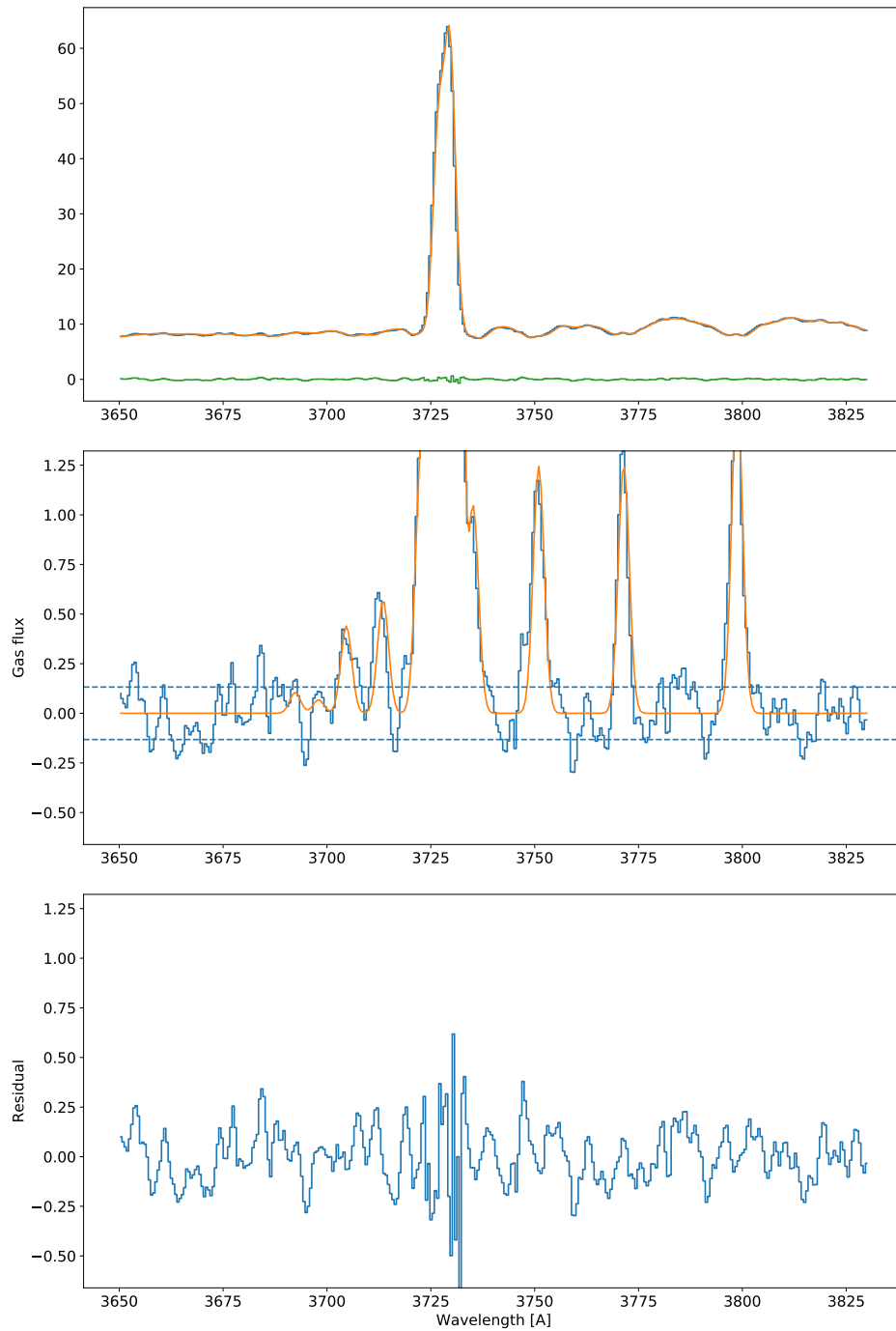


Figure 4.5. The figure illustrates a typical pPXF fit to one of stacks galaxies, and to the gas emissions in 3650 - 3850Å wavelength interval. In this range, we could perfectly detect HI series, [HeI] λ 3704, [OII] λ 3726, [OII] λ 3728, [SIII] λ 3722, and H η . Top panel: total spectrum (blue), model spectrum (orange) and residuals (green). Middle panel: spectrum after subtraction of the stellar continuum and model fit. Bottom panel: residuals of the fit with the same scaling of middle panel.

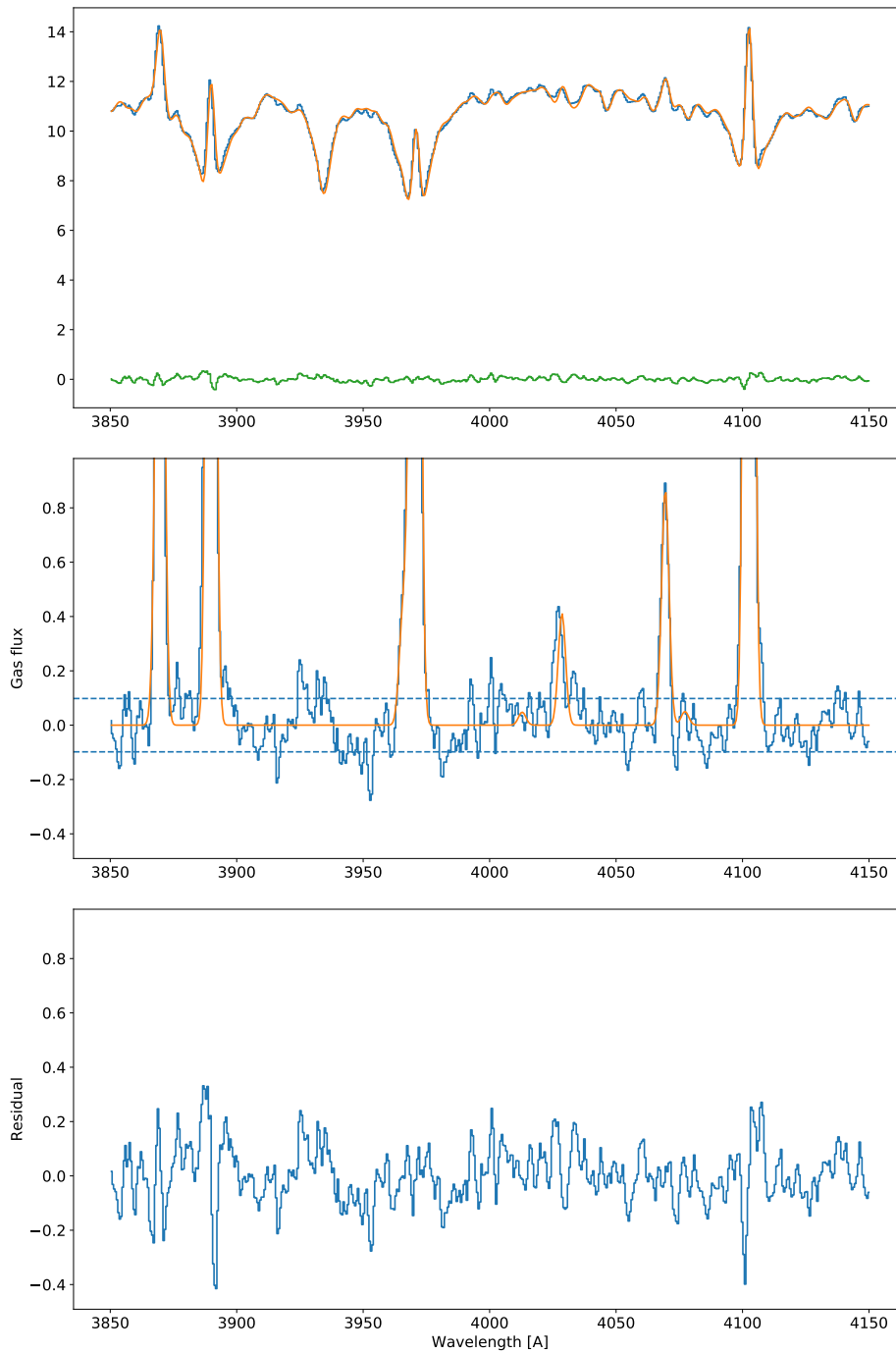


Figure 4.6. The description is as same as Fig.4.5 but in 3850 - 4150Å wavelength interval. In this range, we could perfectly detect [HeI] λ 3867, H ζ , H ϵ , [HeII] λ 3969, [SII] λ 4068, [SII] λ 4077, and H δ .

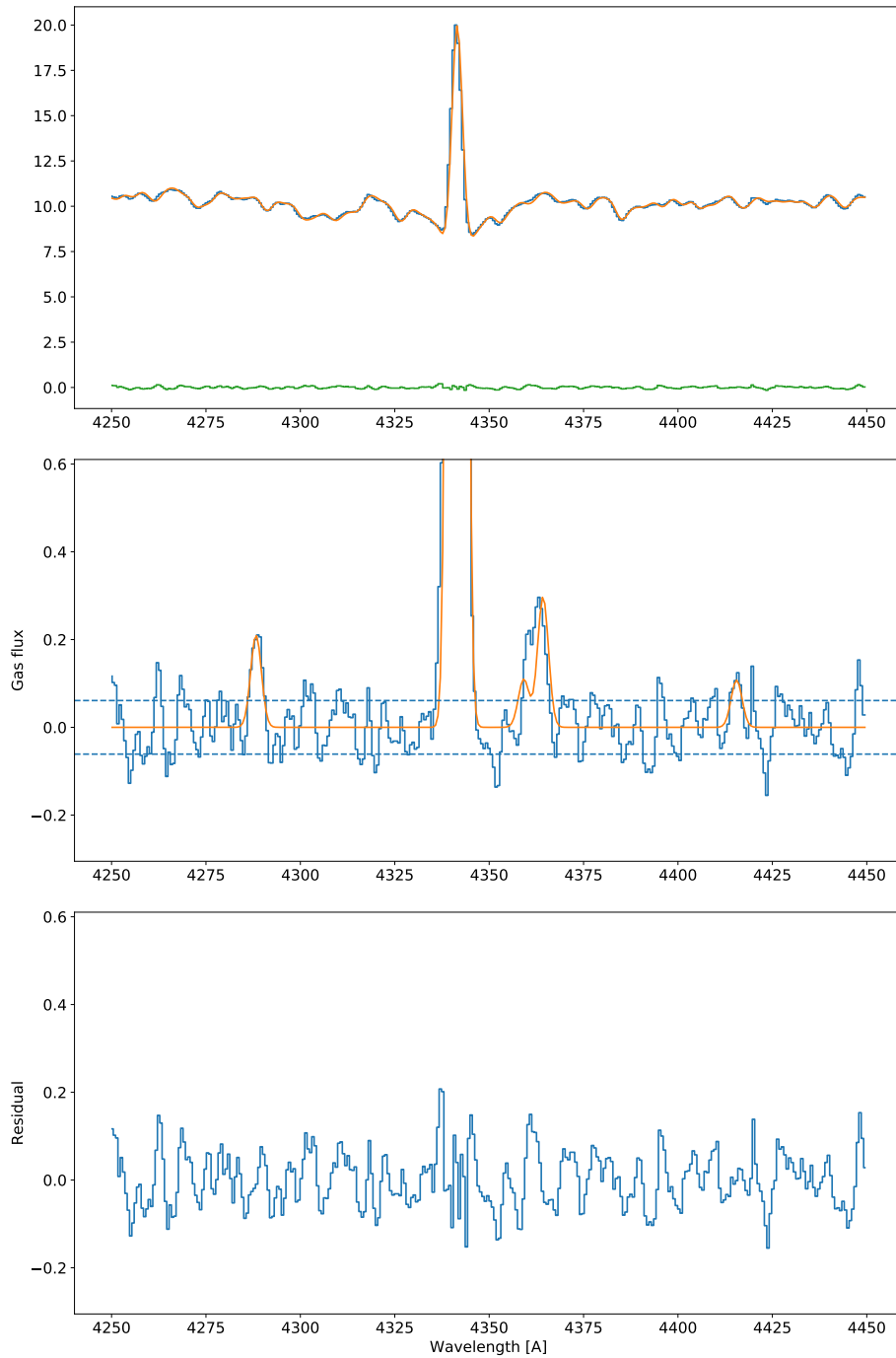


Figure 4.7. The description is as same as Fig.4.5 but in 4250 - 4450Å wavelength interval. In this range, we could perfectly detect [OIII] λ 4363, H γ , and [FeII] λ 4288.

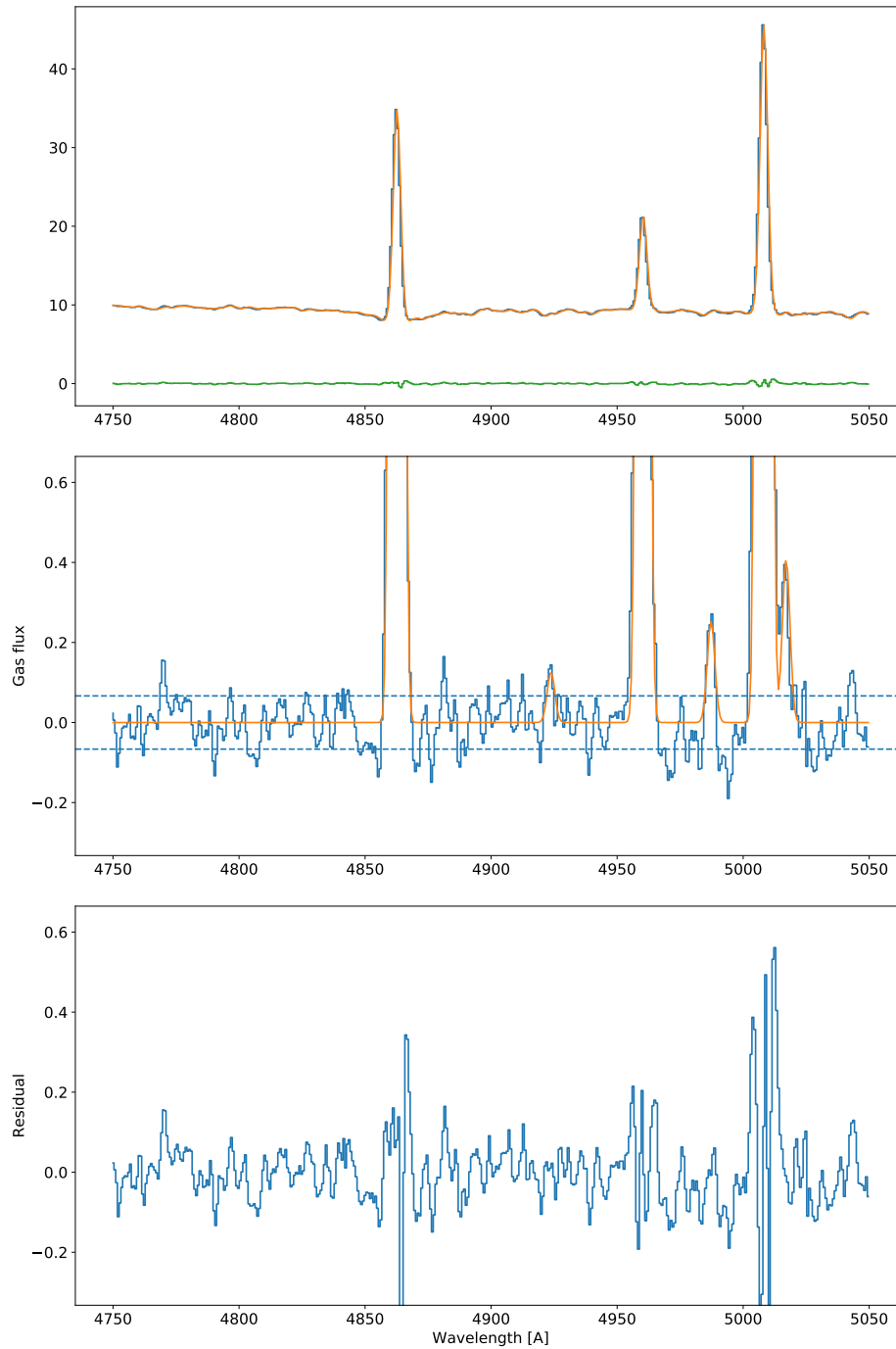


Figure 4.8. The description is as same as Fig.4.5 but in 4750 - 5050Å wavelength interval. In this range, we could perfectly detect [OIII] λ 4959, [OIII] λ 5007, H β , and [HeI] λ 4922.

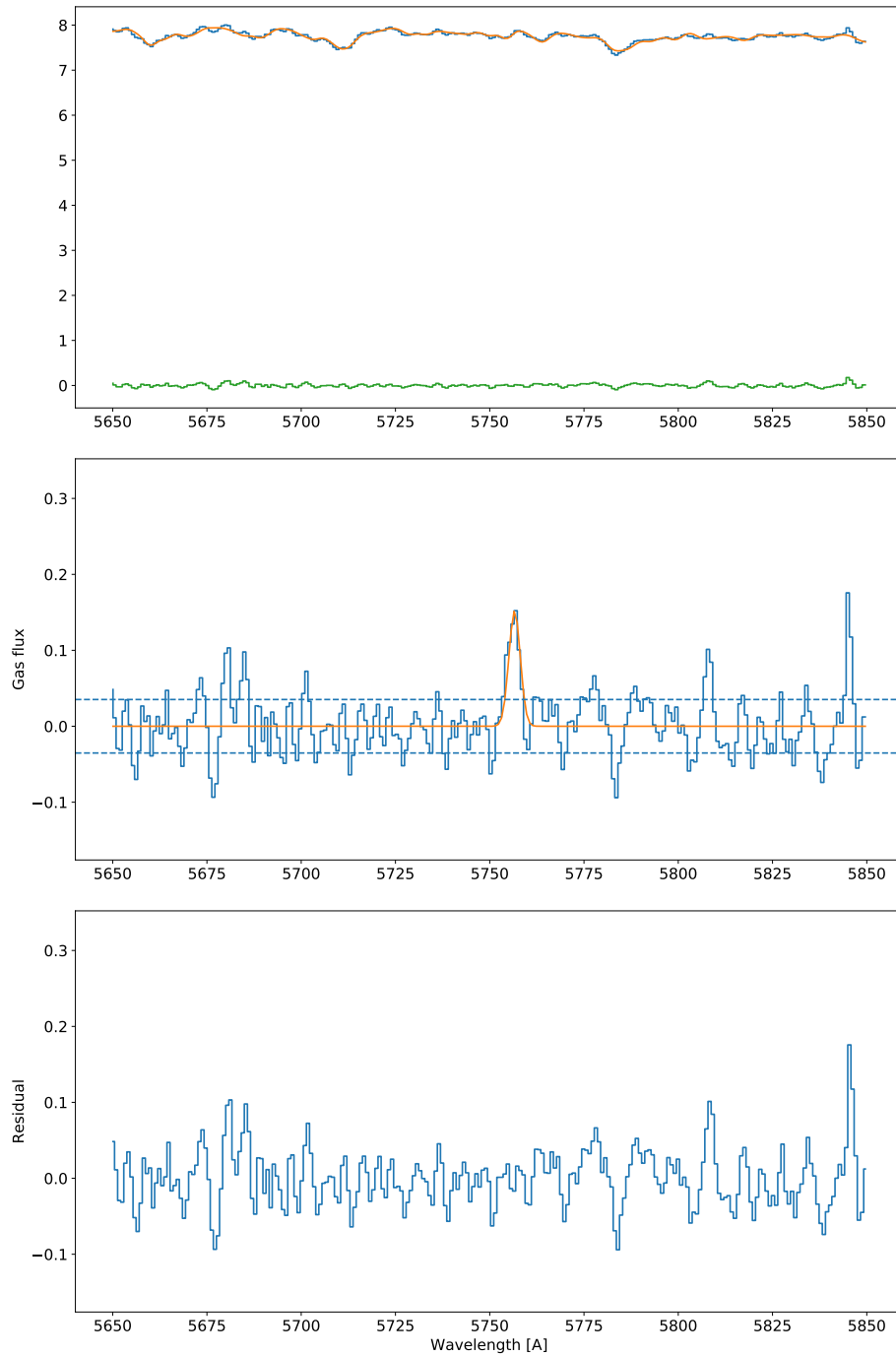


Figure 4.9. The description is as same as Fig.4.5 but in 5650 - 5850Å wavelength interval. In this range, we could perfectly detect [NII] λ 5754.

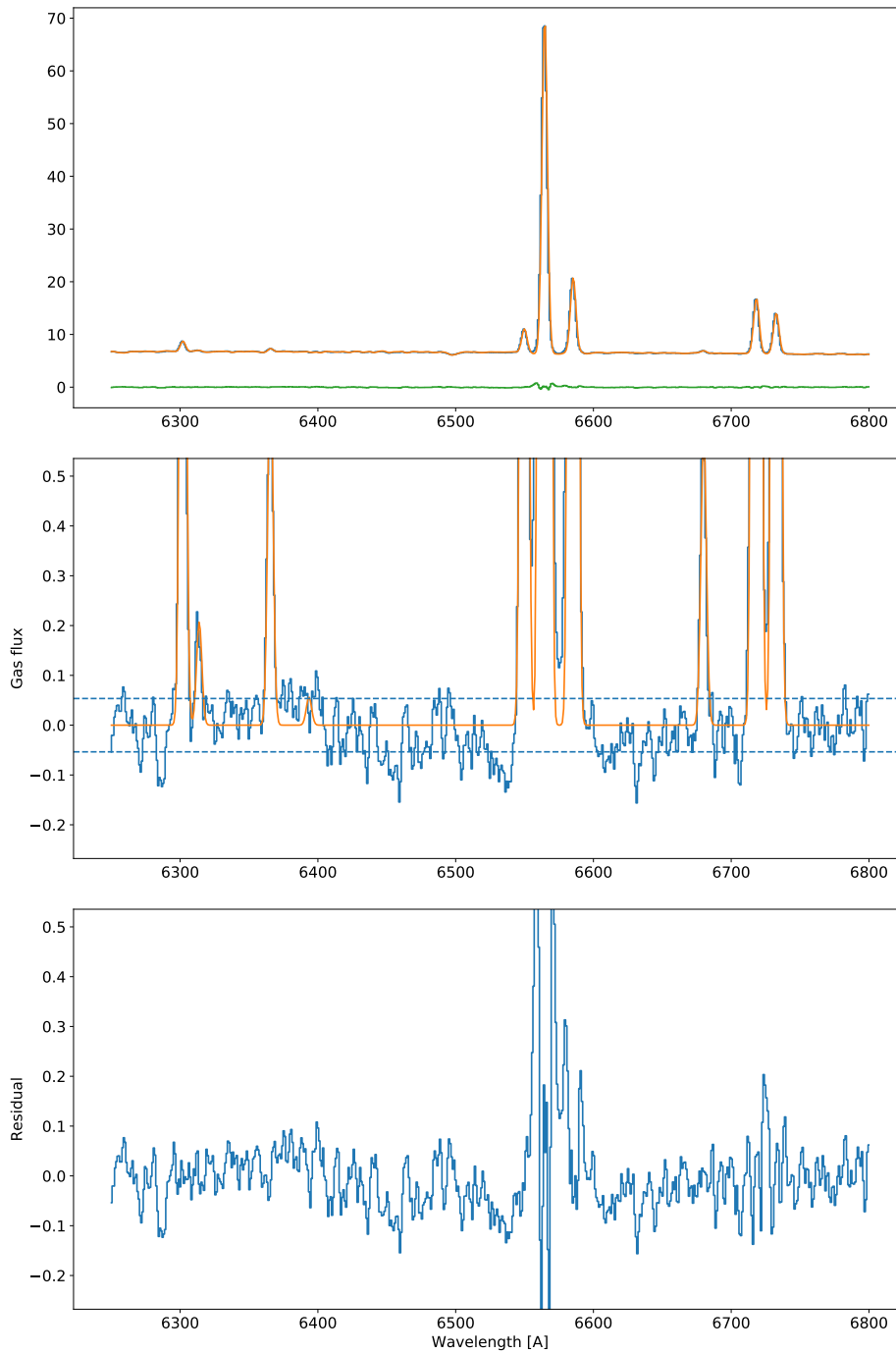


Figure 4.10. The description is as same as Fig.4.5 but in 6250 - 6800Å wavelength interval. In this range, we could perfectly detect [O I] λ 6300, [O I] λ 6363, [O I] λ 6391, [N II] λ 6548, [N II] λ 6584, H α , [He I] λ 6678, [S II] λ 6716, and [N II] λ 6730.

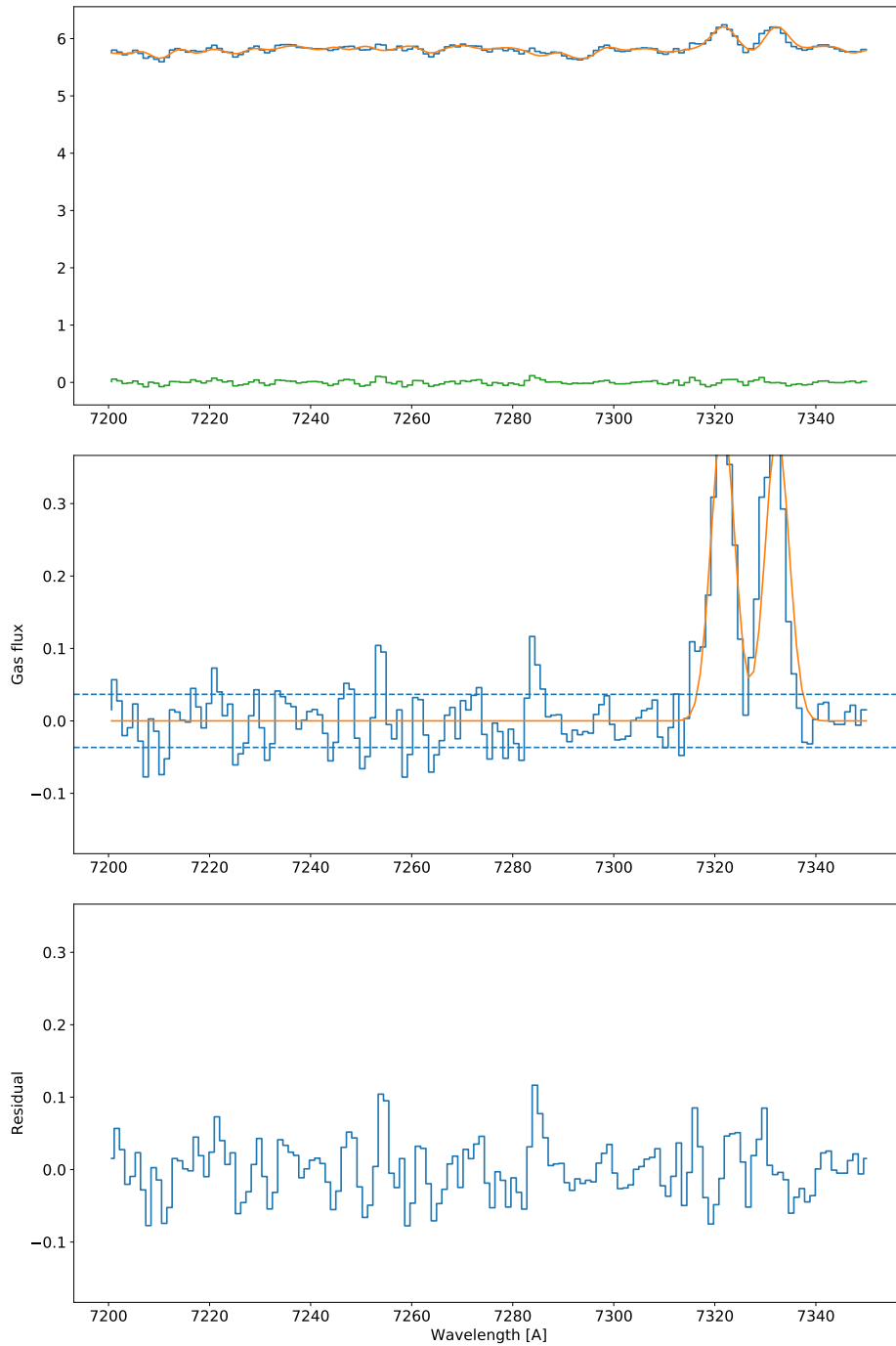


Figure 4.11. The description is as same as Fig.4.5 but in 7200 - 7350Å wavelength interval. In this range, we could perfectly detect [OII] λ 7319 and [OII] λ 7330.

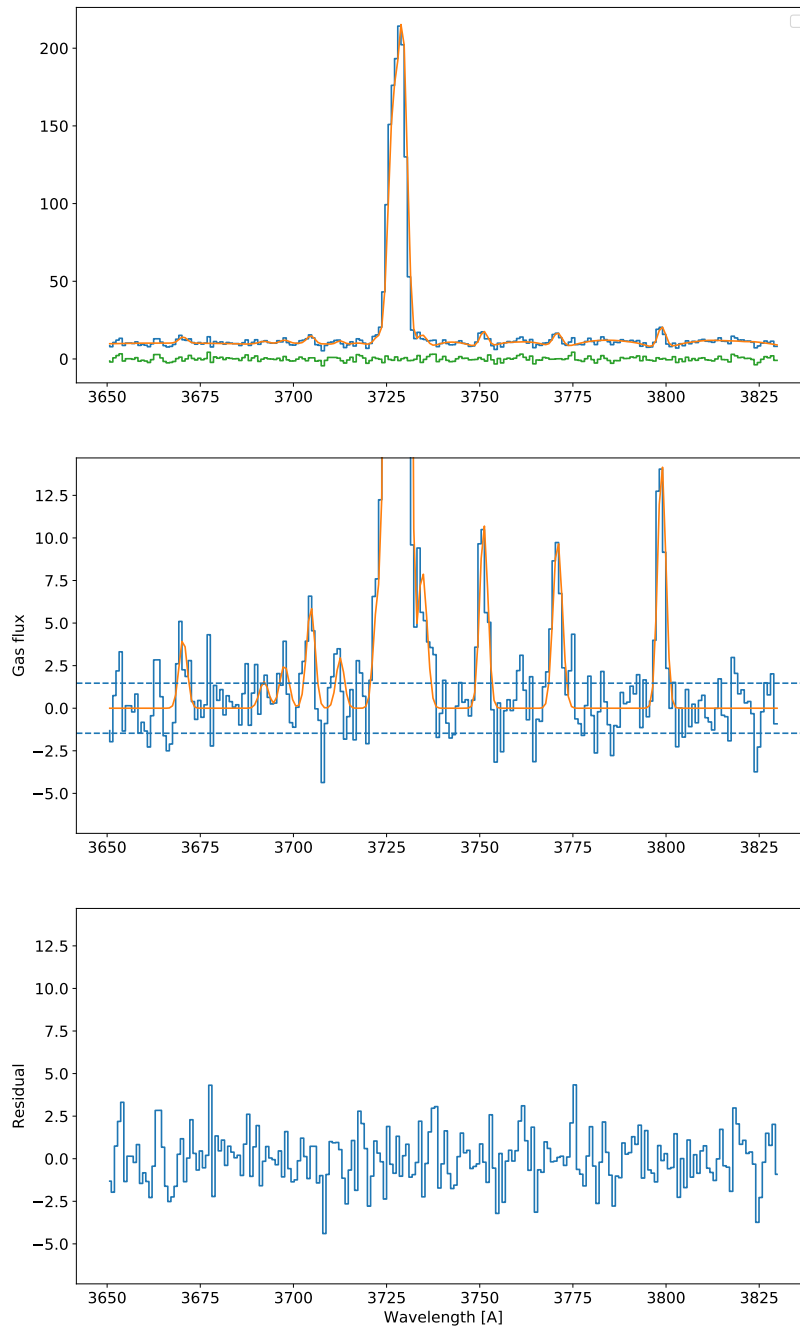


Figure 4.12. The figure illustrates a typical pPXF fit to one of single galaxies, and to the gas emissions in 3650 - 3850Å wavelength interval. In this range, we could perfectly detect HI series, [HeI] λ 3704, [OII] λ 3726,[OII] λ 3728,[SIII] λ 3722, and H γ .

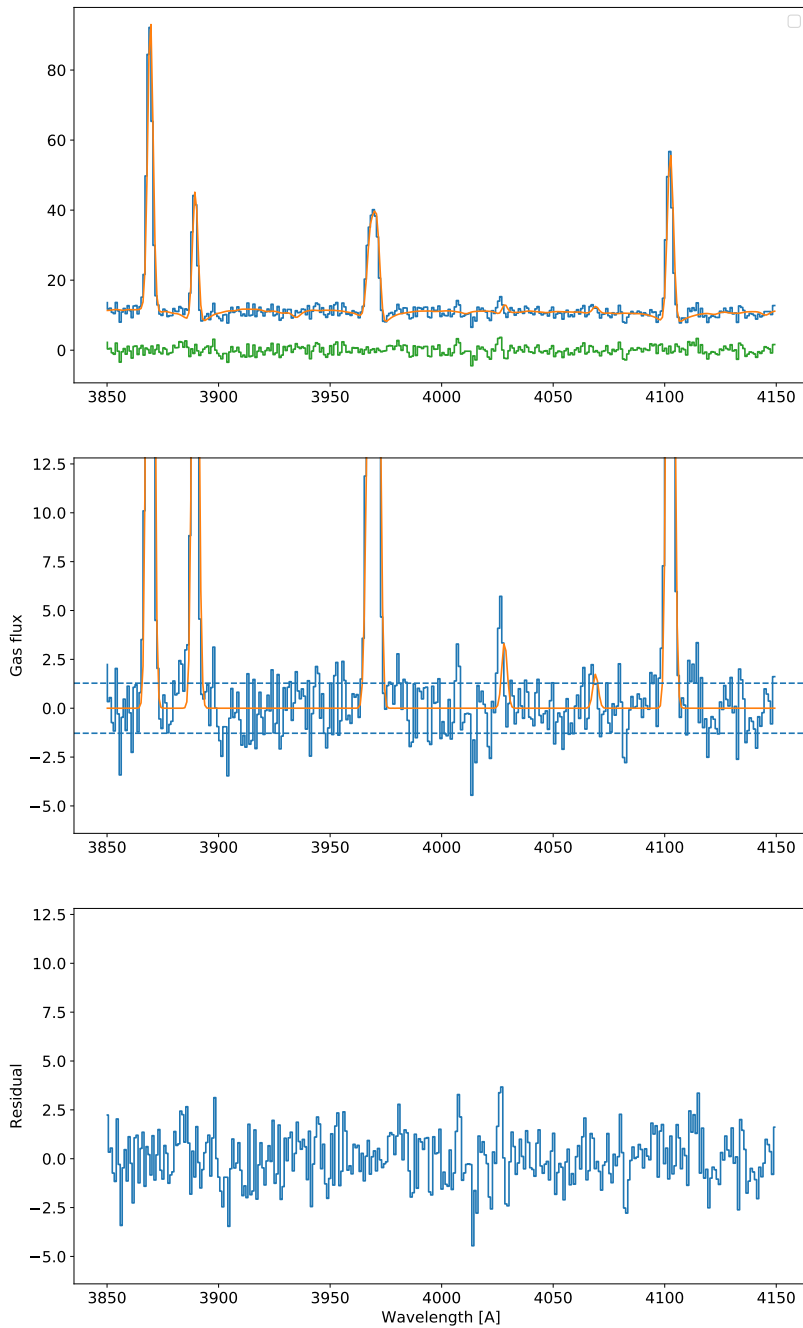


Figure 4.13. The description is as same as Fig.4.5 but in 3850 - 4150Å wavelength interval. In this range, we could perfectly detect [HeI] λ 3867, H ζ , H ϵ , [HeII] λ 3969, [SII] λ 4068, [SII] λ 4077, and H δ .

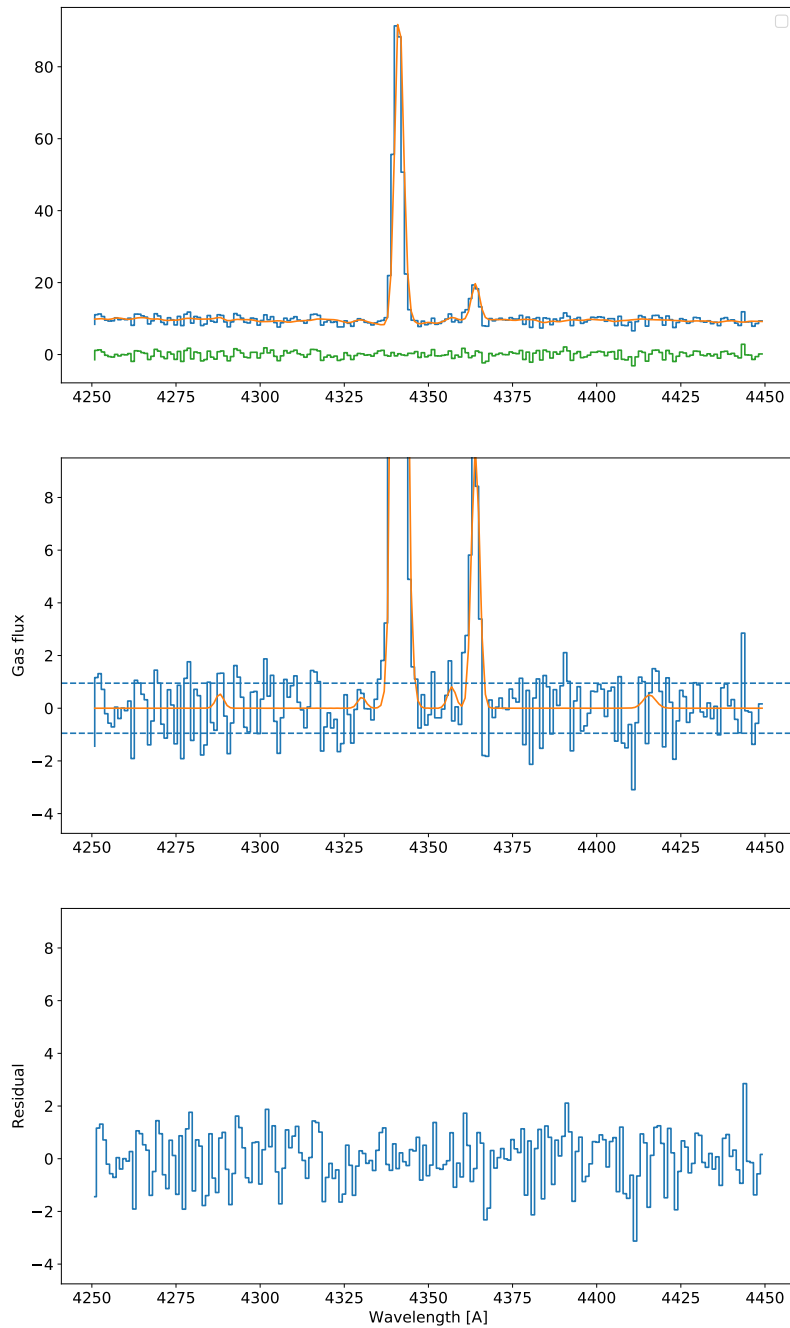


Figure 4.14. The description is as same as Fig.4.5 but in 4250 - 4450Å wavelength interval. In this range, we could perfectly detect [OIII]λ4363, H γ , and [FeII]λ4288.

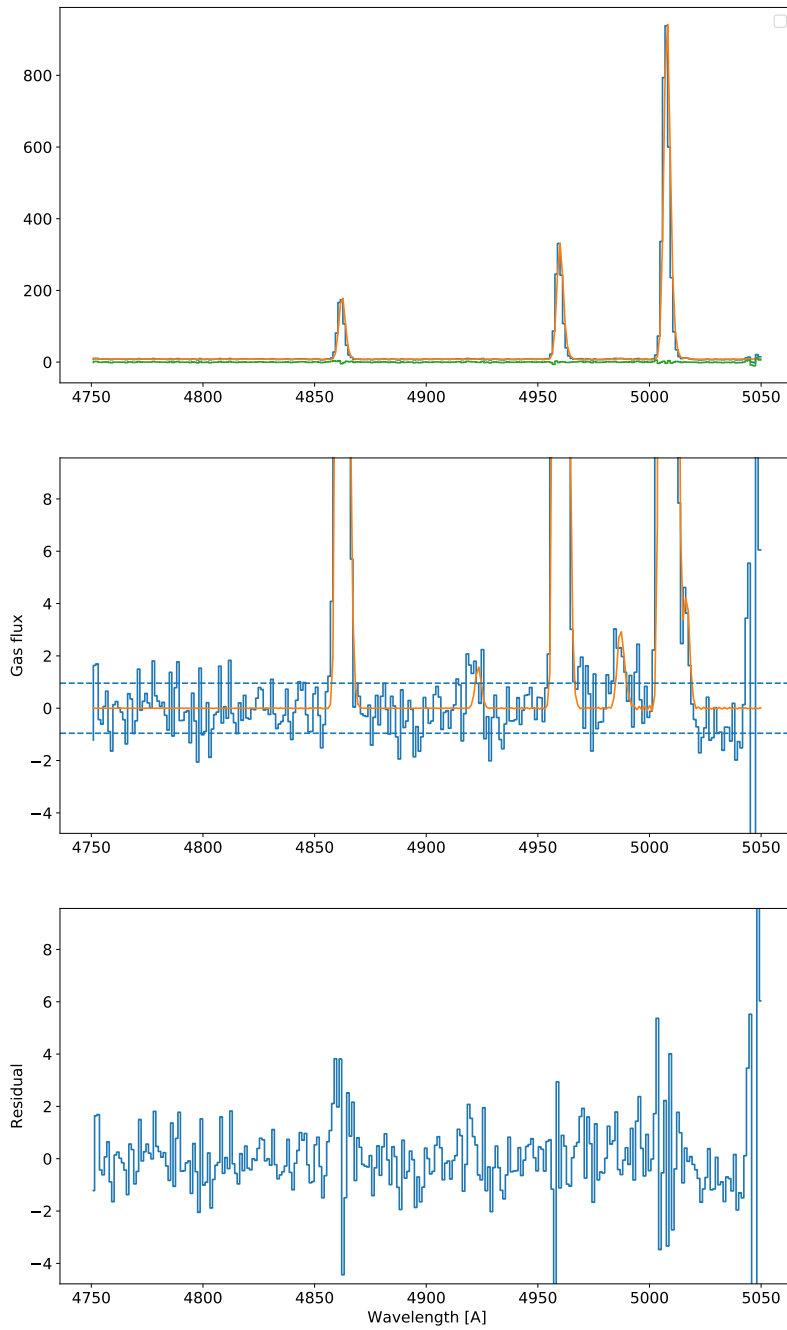


Figure 4.15. The description is as same as Fig.4.5 but in 4750 - 5050Å wavelength interval. In this range, we could perfectly detect [OIII]λ4959, [OIII]λ5007, Hβ, and [HeI]λ4922.

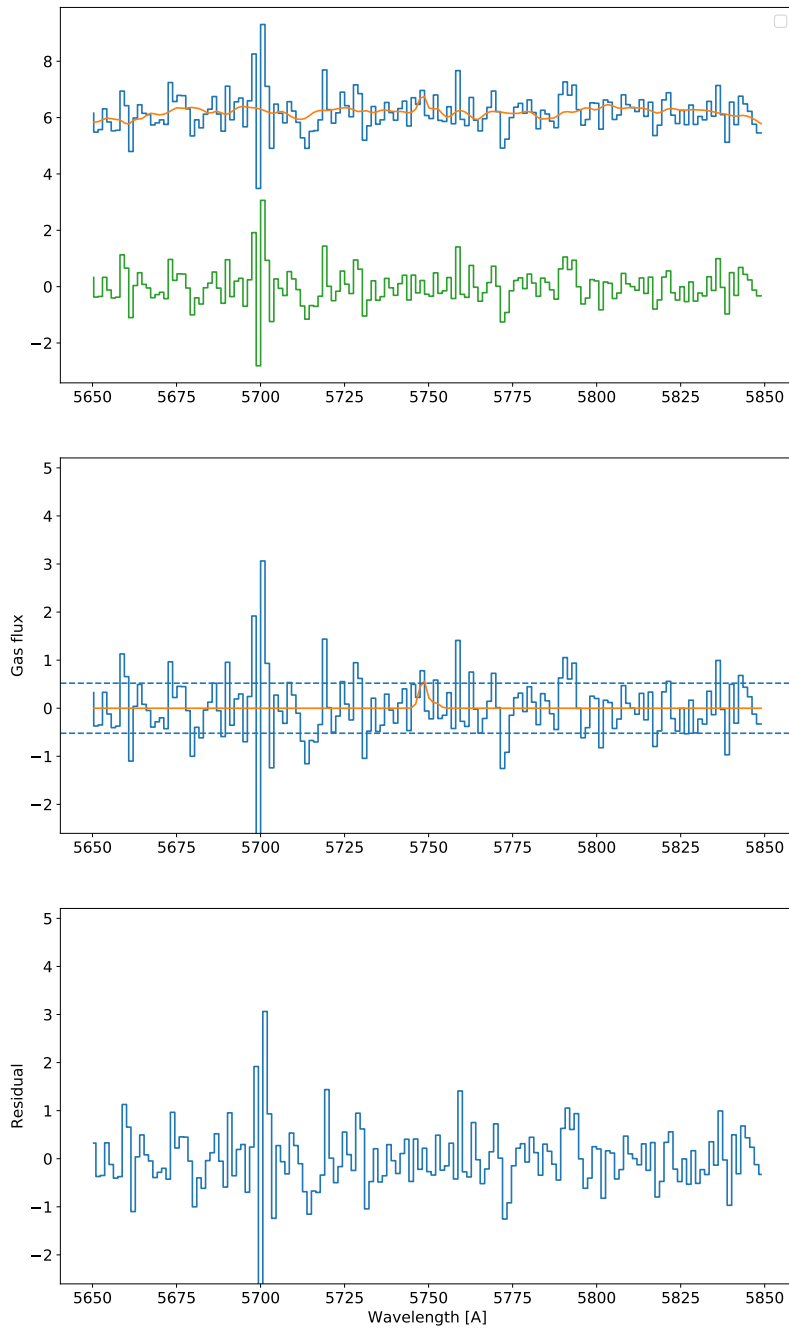


Figure 4.16. The description is as same as Fig.4.5 but in 5650 - 5850 Å wavelength interval. In this range, we could perfectly detect [NII] λ 5754.

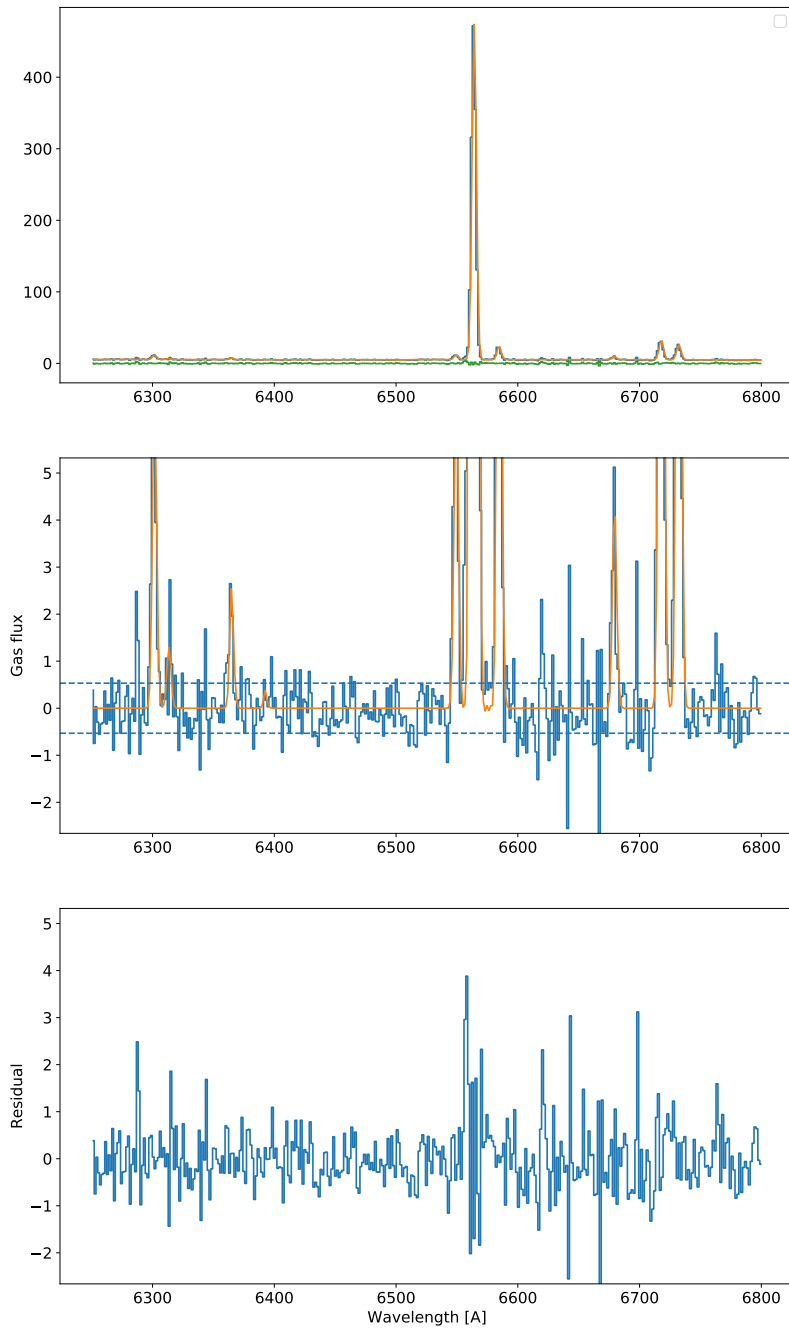


Figure 4.17. The description is as same as Fig.4.5 but in 6250 - 6800Å wavelength interval. In this range, we could perfectly detect [OI] λ 6300, [OI] λ 6363, [OI] λ 6391, [NII] λ 6548, [NII] λ 6584, H α [HeI] λ 6678, [SII] λ 6716, and [NII] λ 6730.

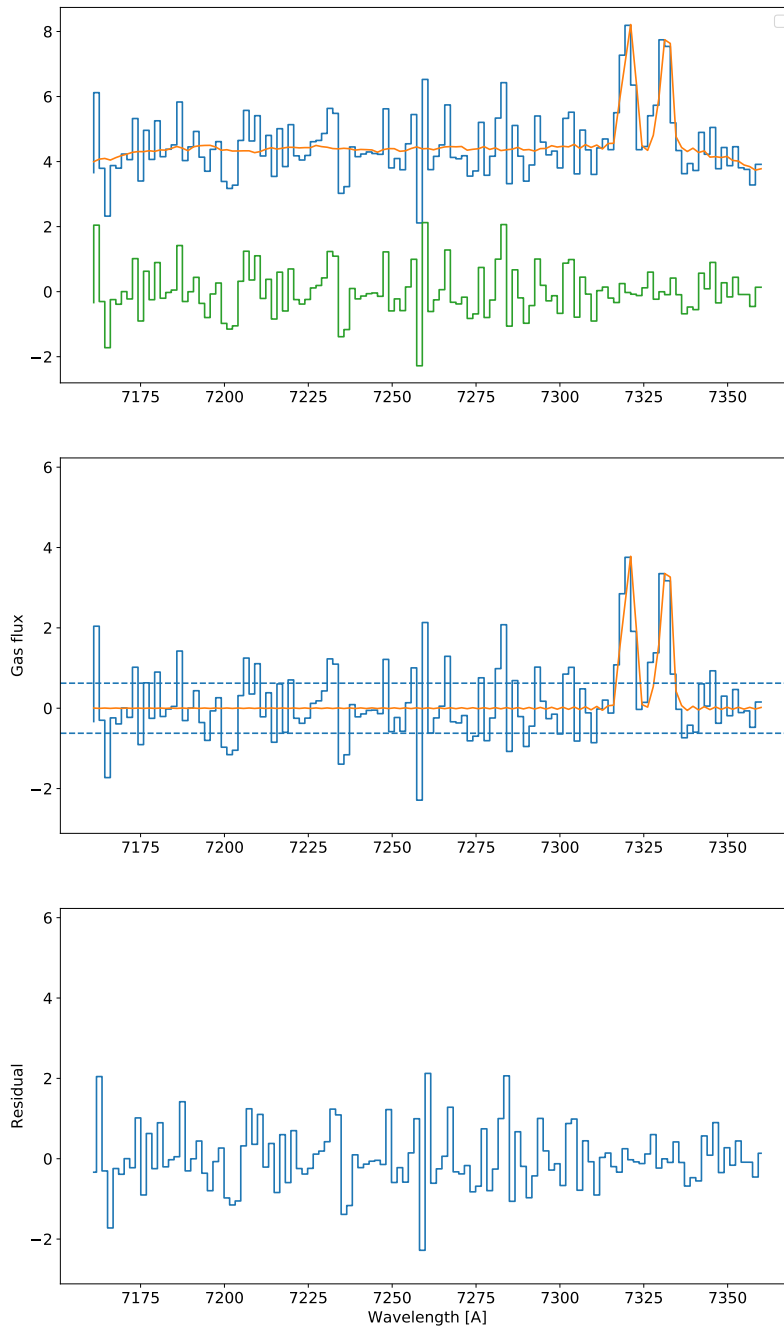


Figure 4.18. The description is as same as Fig.4.5 but in 7160 - 7340Å wavelength interval.

Chapter 5

Multi-cloud application on starforming galaxies

The abundance of chemical elements across cosmic time provide unique information on the physical processes driving the evolution of galaxies. Current methods for measuring gas-phase metallicities, based on either direct measurements of electron temperature (T_e) or calibrations from strong nebular emission line ratios, are based on simplifying assumptions and do not adequately describe the complexity of the emitting regions. We present a new approach based on fitting galaxy spectra with multi-cloud photoionisation models. Unlike current methods, based on comparisons with single-cloud models, our methodology is able to reproduce all observed emission lines to a very high accuracy, down to a few percent, thus allowing for accurate metallicity measurements. We further recover the well known trends between ionization parameter and metallicity, and between the Nitrogen and Oxygen abundances. Our models accurately reproduce the auroral-to-nebular line ratios, while the results of the standard T_e method are sometimes very different from the best-fitting model metallicity. We finally present newly calibrated metallicity estimators for galaxies based on ratios between strong emission lines.

5.1 A new, multi-cloud method to accurately model emission lines in star-forming galaxies

To apply our new photoionisation models and verify their performances, we consider sample of galaxies covering a wide range of metallicity at both low and high metallicity which spoke in section 3. Throughout this work, in our CLOUDY simulation, we will assume the gas nebula is dusty, ionisation-bounded and consider models at constant pressure.

The prominent parameters of the photoionised gas and their range of variation are as followed:

- **Nebular metallicity**, $12 + \log(O/H)_{PH}$: We consider values of $12 + \log(O/H)_{PH}$ in the range between 6.69 and 9.19, in steps of 0.05 dex. Assuming a solar metallicity of $Z_{\odot} = 8.69$ (Asplund et al., 2009), this range corresponds to $[Z/Z_{\odot}] = [-2.0, 0.5]$.
- **Ionization parameter**, U : The ionization parameter (U) is defined as the ratio of

ionizing photon density to hydrogen density:

$$U = \frac{Q(H)}{4\pi R_{in}^2 n_H c}, \quad (5.1)$$

where $Q(H)$ is the flux of ionizing photons striking the illuminated face of the cloud, n_H is the hydrogen gas density, R_{in} is the inner radius of the cloud and c is speed of light. We compute models for values of $\log U$ in the range between -4.0 to 0.0, in steps of 0.5 dex.

- **Hydrogen gas density (n_H):** We compute models for hydrogen densities of the ionized gas, spanning logarithmic from 0 to 5 in steps of 1.0 dex corresponding roughly to the observed values of electron densities in extragalactic HII regions and star-forming galaxies.
- **Stellar population synthesis libraries:** The shape of ionising radiation field produced by a star cluster depends on the age of the stellar population and on its metallicity. We use the BPASS spectral synthesis code (Eldridge, Stanway, 2012), which includes binary stars and has a range of values of both stellar ages and stellar metallicities. We consider a wide range of ages (3, 5, 8, 10, 20 Myrs) and logarithmic stellar metallicity (-3.6, -2.6, and -1.6).

To find which combination of photoionisation models reproduces the emission lines from the observed sample, based on a new multiple-cloud approach, we consider a linear combination of single-cloud photoionisation models. The idea underlying our new multiple component approach is that if a model can reproduce all the emission line luminosity then, for each ionic species, the model reproduces the correct occupied volume at the right temperature and therefore it can be used to determine the abundances and then metallicity.

We consider a two-dimensional grid of models with varying U and n_H , ionising continuum, and metallicity. The best model is therefore a linear combination of single-cloud models with

$$L_i = \sum_j w_j l_{i,j}, \quad (5.2)$$

where $l_{i,j}$ is the luminosity of line i from model j and w_j are the non-negative weights required to reproduce the observed line luminosity.

To select the best model we minimise the χ^2 per degree of freedom, defined as

$$\chi^2 = \frac{1}{N_l} \sum_l \left(\frac{f_l - m_l}{\sigma_l f_l} \right)^2, \quad (5.3)$$

where f_l is the observed flux of line l , m_l is the flux in the model; N_l number of observed lines used in fit σ_l the acceptable relative disagreement between observed and model line flux.

In practice, σ_l is taken to be by the relative error of the observed line flux or a fixed value of 10% if the relative error is smaller than that.

The fitting process works as follows: for each value of metallicity and each ionising continuum we compute the best-fit linear combination of models of varying $\log U$ and n_H . We then pick as the best model the one with the lowest χ^2 per degree of freedom.

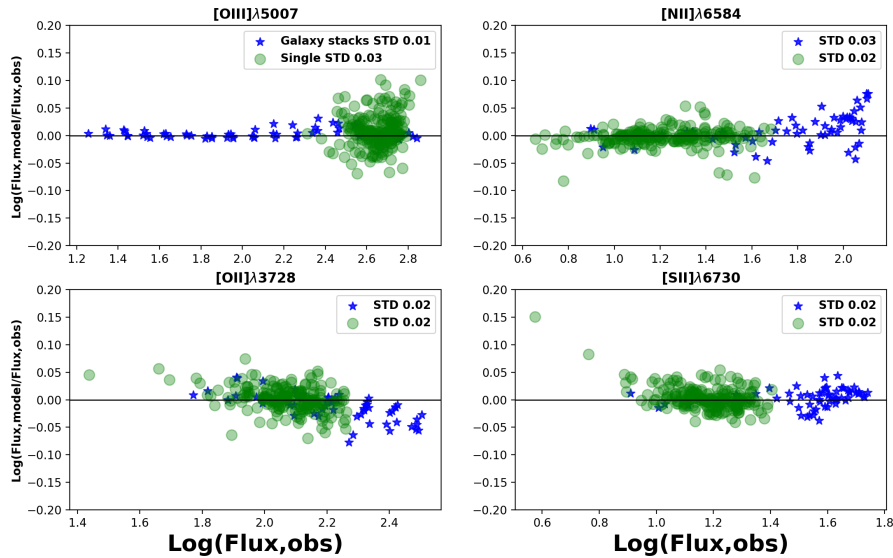


Figure 5.1. Best-Model predicted emission lines fluxes (normalized to $H\beta=100$) for different elements in different ionisation states, compared to observed emission lines. With using a multiple cloud approach, different emission lines in both low and high ionisation states simultaneously provided. Green circle and blue stars represent single galaxies and galaxy stacks, respectively.

Thus, we find the best weights for for all the models to reproduce the observed luminosity. These emission lines fluxes are $H\alpha$, $H\beta$, $[OIII]\lambda 5007$, $[OIII]\lambda 4363$, $[OII]\lambda 3726$, $[OII]\lambda 3728$, $[OII]\lambda 7319, 7329$, $[OI]\lambda 6300$, $[NII]\lambda 6584$, $[NII]\lambda 5754$, $[SII]\lambda 6730$, $[SII]\lambda 6716$, and $[SII]\lambda 4068$.

We apply also the flux rescaling for $[NII]\lambda 6584$, $[NII]\lambda 5754$, $[SII]\lambda 6730$, $[SII]\lambda 6716$, and $[SII]\lambda 4068$ to obtain sulfur and nitrogen abundances. In Fig.5.2 we show the behaviour of χ^2 as a function of metallicity (for a fixed ionising spectrum) for an example galaxy. Here we plot for each metallicity the lowest χ^2 obtained by combining models of different $\log U$ and n_H . We always observe a clear minimum χ^2 , at a value of metallicity which is in agreement with that measured from the direct method, in both single galaxies and stacks.

5.1.1 Flux comparisons

In Fig.5.1 we show four different emission lines, roughly representative of species probing different ionisation zones in the nebula. In particular, $[OIII]$ and $[NII]$ species probe high and low ionization zones, respectively. We compare the observed line fluxes with those obtained from the the best models, finding that the two are in agreement at a level of better than 10 percent.

5.1.2 Electron Temperatures and Density

To estimate electron temperatures and densities of different zones, the complete ionization structure of a HII region/ star forming galaxy is required. In practice, a two-zone (of low and high ionization) or even a three-zone (of low, intermediate and high ionization) structure

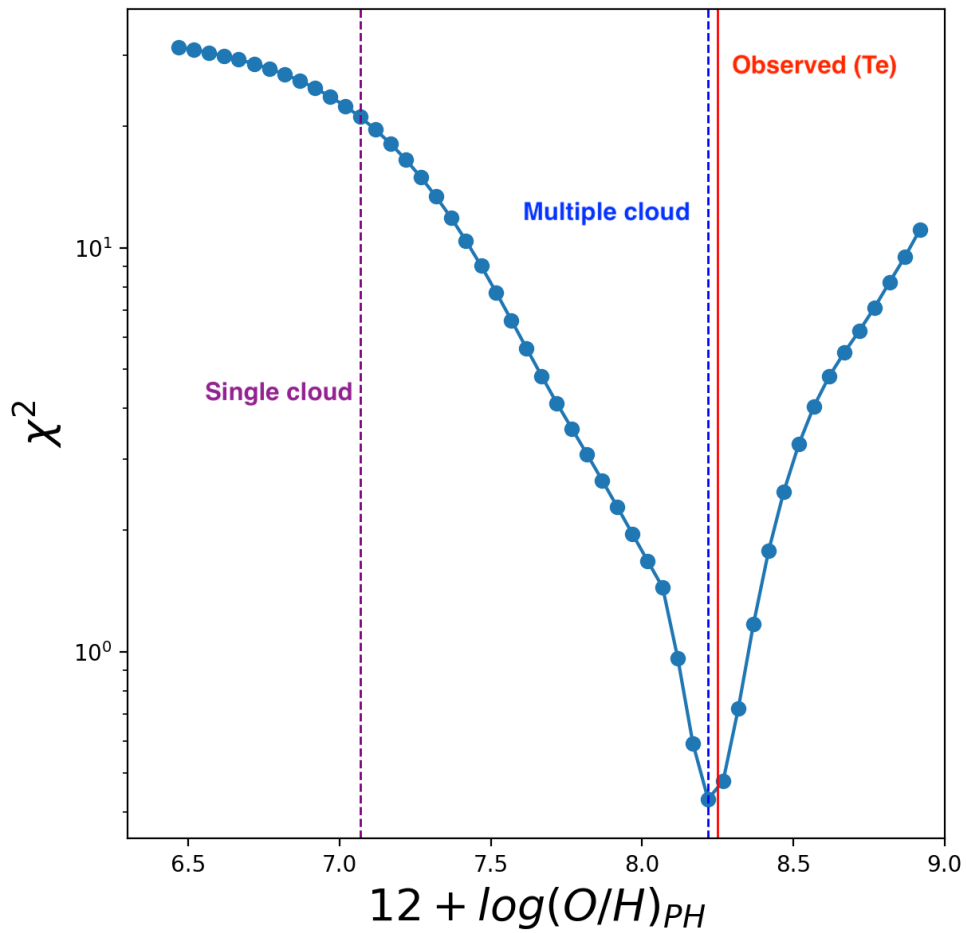


Figure 5.2. Variation of the χ^2 of the best-fit models as a function of $12 + \log(O/H)_{PH}$ for a single galaxy. The red dotted line shows the observed galaxy T_e metallicity. The blue dotted lines is located in a clear minimum of the χ^2 curve. The metallicity inferred from a best-fit single cloud approach is shown for comparison with a purple dotted line.

is acquired to model the HII regions/ star forming galaxy responsible for emission lines in them. For temperature estimation, we utilise a two-zone HII region: in this scenario, the high ionization zone is traced by the O^{2+} ion, while the low ionization zone could be traced by different ionic species, e.g. O^+ , N^+ and S^+ .

Given the SDSS spectral coverage, in our data, we have two different diagnostics for the temperature of the low ionization zone (which we will refer to as t_2 from now on), namely $[OII] \lambda 3727, 3729 / [OII] \lambda 7320, 7330$, and $[SII] \lambda 6717, 6731 / [SII] \lambda 4969$ (t_s). On the other hand, we have only one tracer of the temperature of the high-ionization zone (t_3), namely $[OIII] \lambda 5007 / [OIII] \lambda 4363$. Other collisionally excited lines probing the temperature of the intermediate and high ionization region are either too weak and thus undetectable even in galaxy stacks (e.g. $[ArIII] \lambda 5192$) or fall outside the spectral range of the SDSS spectrograph (e.g. $[SIII] \lambda 9069$, $[Ne III] \lambda 3342$).

We compute electron temperatures using PyNeb Luridiana et al. (2011); Luridiana et al. (2015b), for oxygen and sulfur auroral lines and the $[SII] \lambda \lambda 6717, 6731$ ratio is used to determine electron densities.

Temperature–Temperature relation

In Fig.5.3 we show the relations between $T_{[OII]}$ and $T_{[OIII]}$ and between $T_{[SII]}$ and $T_{[OIII]}$ for the best-fit models. $[OII]$ and $[SII]$ trace the low-ionisation zone, while $[OIII]$ traces the high ionisation one. The linear form of the relation between $T_{[OII]}$ and $T_{[OIII]}$, called t2-t3 relation, has been proposed first by Campbell et al. (1986) and then revised in several subsequent studies Garnett (1990); Pilyugin et al. (2006b,a, 2009, 2010). This relation is of great interest in the context of nebular studies since it is generally used to compute the electron temperature for unseen ionization states. We fit the temperature-temperature relations with linear models and obtain:

$$T_{[OII]} = 2300(\pm 648) + (0.83(\pm 0.05)) \times T_{[OIII]} \quad (5.4)$$

and for $T_{[SII]}$ and $T_{[OIII]}$:

$$T_{[SII]} = 3110(\pm 832) + (0.71(\pm 0.07)) \times T_{[OIII]}. \quad (5.5)$$

As shown in Fig.5.3, our model-derived best-fit relations are in good agreement with the empirical relation presented by Pilyugin et al. (2009). Our best models for the SDSS galaxy stacks falls below the t2-t3 relation, as already reported in Curti et al. (2017). It is evident that for composite spectra, the t2-t3 relation both overestimates (or underestimates) the temperature of the high ionization zone and reflects the intrinsic characteristics of global galaxy spectra.

The best models for single galaxies suggests a smooth positive correlation between $T_{[OIII]}$, $T_{[OII]}$, and $T_{[SII]}$. At least two factors can contribute to deviations from a linear relations. First, The $[SII]$ and $[OII]$ line intensities can be affected by recombination, which will lead to temperature values higher than the real ones. Second, finding the best models may be constrained by the low S/N ratio $[SII]$ auroral lines.

5.1.3 Ionic Abundances Determination

The relation between N/O and O/H trend is well studied in galaxies of varying types. This diagram traces the difference in nucleosynthetic origin between oxygen and nitrogen. At

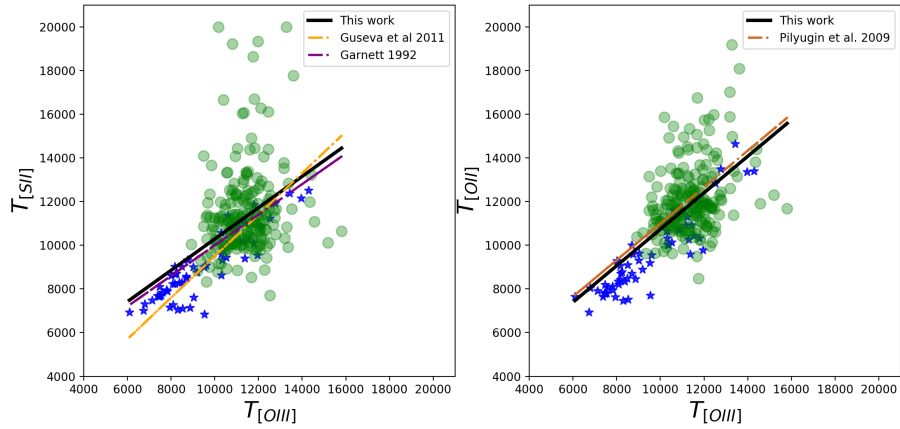


Figure 5.3. Comparison of electron temperatures between different ionisation zones. Electron temperatures $T_{[OIII]}$, $T_{[OII]}$, and $T_{[SII]}$ are determined, respectively, from the auroral lines $[OIII]\lambda 4363$, $[OII]\lambda\lambda 7320, 7330$ and $[SII]\lambda 4068$. Blue stars and green circles represent the best models for galaxy stacks and single galaxies, respectively. The black solid line is the best linear fit to the data points. The right panel compares $[OII]$ temperatures to the high-ionization zone temperatures from $[OIII]$. The brown line is the $T_{[OII]} - T_{[OIII]}$ relation from Pilyugin et al. (2009). The left panel shows the $T_{[SII]} - T_{[OIII]}$ relation. The orange and purple dotted lines show the empirical relations presented in Guseva et al. (2011) and Garnett (1992), respectively.

low metallicity, nitrogen has mostly a primary nucleosynthetic origin (Tomkin, Lambert, 1984; Edmunds, Pagel, 1978; Henry et al., 2000; Carbon et al., 1987) and the N/O ratio is fixed at a value of $\log(N/O) \sim -1.6$. At higher metallicity, the N/O ratio shows a steeply increasing trend (Vila-Costas, Edmunds, 1993). This trend is interpreted as due to production of nitrogen as a secondary nucleosynthetic product, which is delayed relative to oxygen and dominates at high abundances. (Garnett, 1990) demonstrated that there can be significant scatter in N/O at a given O/H, and (Izotov, Thuan, 1999b) confirmed that this scatter is significant for oxygen abundances above $12 + \log(O/H) = 7.7$ (Vincenzo et al., 2016).

The N/O abundance ratios derived from the best models as a function of the total oxygen abundance is presented in Fig.5.4. As a visual aid, we plot the empirical fit to stellar abundances by Nicholls et al. (2017) as a orange green line. For our samples, we find a 2-degree polynomial function of (black solid line):

$$\log(N/O) = 44.09(\pm 15.36) - 12.02(\pm 3.68) \times z + 0.78(\pm 0.22) \times z^2 \quad (5.6)$$

which z is $12 + \log(O/H)_{PH}$ value. This abundance ratio is clearly different in single galaxies versus galaxy stacks. At a given metallicity, the galaxy stacks have higher N/O with respect to single galaxies, with largest spread. N/O is expected to depend on the star-formation history and it maybe indicate the large spread between single galaxies and galaxy stacks depends on this parameter in each bin used for stacking procedure. Ne, S and Ar are α -elements, and are synthesized in massive stars by α -particle capture, and released to the ISM by core-collapse supernovae. In Fig.5.4, we show the S/O abundance ratio obtained for our best models as a function of metallicity for both single galaxies and galaxy stacks. The relation between S/O and best model metallicity can be approximated well by a linear relation of the type

$$\log(S/O) = -0.70(\pm 0.18) + (-0.11(\pm 0.022) \times z). \quad (5.7)$$

In agreement with the work of Izotov et al. (2006); Guseva et al. (2011), our results points towards a decrease in the S/O abundance with increasing metallicity. This result is inconsistent with CHAOS observations (Berg et al., 2015b; Croxall et al., 2015b, 2016b) and their estimation denoted by the pink dashed lines ($\log S/O = -1.41 \pm 0.16$) in figure 5.4. Although the galaxy stacks show a roughly constant value of S/O, $\log(S/O) = -1.62$, the addition of single galaxies reveals the decreasing relation. Some mild trends in S/O abundance ratios may indicate a metallicity dependence of massive stars' α -elements production (Izotov et al., 2004). Variations of the explosion energy of Type II supernovae with low metallicity might also play a role Kobayashi et al. (2006). Yin et al. (2011) also show a stronger energy released (by supernovae or stellar wind) not only reduces the abundances and increases the ratio between the long recycling term elements and the short ones, but also decreases the gas fraction dramatically.

Moreover, Izotov et al. (2006) noted that abundance determinations for some elements, such as S, Cl, and Ar, could be uncertain due to uncertainties in atomic data, such as dielectric recombination rates.

5.1.4 Calibrations of strong-line metallicity indicators

For all our best models, we plot the relationships between some of the best-known strong-line metallicity indicators and the true model gas-phase oxygen abundance in Fig.5.5. We adopt the following abbreviations for strong emission-line ratios:

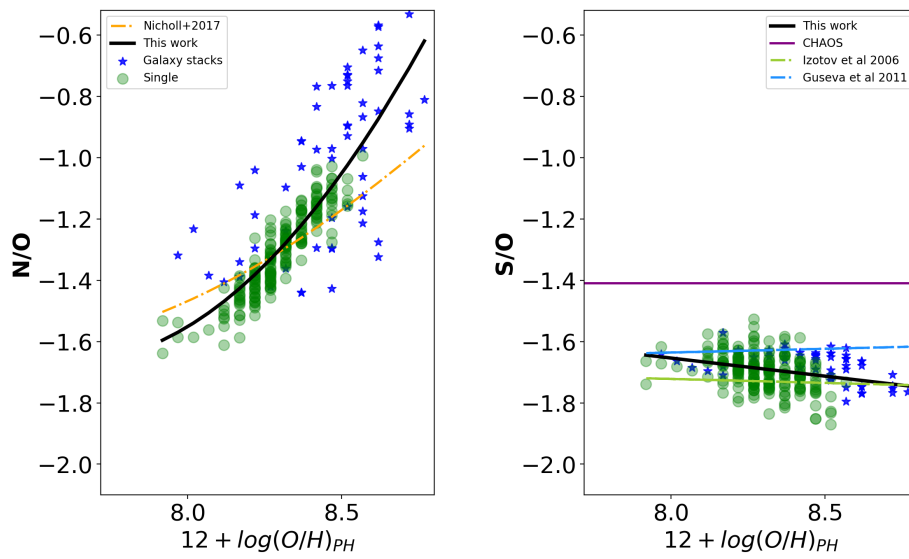


Figure 5.4. Abundance ratios as a function of $12 + \log(O/H)_{PH}$ for the best models. Green circles and blue stars represent the best models for the single galaxies and galaxy stacks, respectively. Left panel: N/O ratio versus $12 + \log(O/H)_{PH}$. The black solid line represents (5.4) and orange fit demonstrates Nicholls et al. (2017). Right panel: S/O ratio versus $12 + \log(O/H)_{PH}$: The black solid line shows (5.7). The results from Guseva et al. (2011); Izotov et al. (2006) demonstrated in green and light blue dashed lines, respectively while the solid purple line show a fit by Berg et al. (2015b). The $12 + \log(O/H)_{PH}$ galaxies stack, on their own, show a flatter relation more than the $12 + \log(O/H)_{PH}$ single galaxies.

$$R2 = [OII]\lambda3727/H\beta \quad (5.8)$$

$$R3 = [OIII]\lambda5007/H\beta \quad (5.9)$$

$$R23 = ([OII]\lambda3726, 3728 + [OIII]\lambda5007)/H\beta \quad (5.10)$$

$$O32 = [OIII]\lambda5007/([OII]\lambda\lambda3726, 3728) \quad (5.11)$$

$$N2 = [NII]\lambda6584/H\alpha \quad (5.12)$$

$$O3N2 = (([OIII]\lambda5007/H\beta)/([NII]\lambda6584/H\alpha)) \quad (5.13)$$

The green circles represent the best models for single galaxies, while the blue stars represent our best models for the galaxy stacks. To obtain our new calibrations, we performed a polynomial fit with the general functional form

$$\log R = \sum_N C_N x^N, \quad (5.14)$$

where R is a given diagnostic and x is $12 + \log(O/H)_{PH}$, which normalized to solar metallicity ($x = 12 + \log(O/H)_{PH} - 8.69$ (see table 5.1).

Based on the ratio of oxygen forbidden lines over hydrogen recombination lines possess the well-known double branch behavior, a high order polynomial fitting is considered necessary because the indicators. In Figure 5.5 we compare our new calibrations with those from Curti et al. (2017) and Maiolino et al. (2008). They obtained observational and semi empirical calibrations, respectively. We should stress that we are considering the metallicity of the best-fit multi-cloud models, which is directly obtained from the model input, while in both Maiolino et al. (2008) and Curti et al. (2017) they consider observed metallicity.

Our N2 calibration is in good agreement with Curti et al. (2017) at both low and high metallicities. At metallicities close to solar this diagnostic begins to saturate, as expected from the fact that nitrogen becomes the dominant coolant of the ISM: Maiolino et al. (2008) calibrations then become comparable against both Curti et al. (2017) and this work. [comment on interpretation]

The O3N2 calibration instead presents a different slope than the Maiolino et al. (2008) calibration,

Although the slope of our O32 calibration is in a good agreement with Curti et al. (2017) as same as R3 and O32 calibration relation, it is different from Maiolino et al. (2008)...

5.1.5 Ionisation properties

In galaxies, the global ionization parameter is usually found to anti-correlate with the gas-phase metallicity. Low-metallicity galaxies or HII regions therefore show high ionization parameters (Dopita, Evans, 1986; Nagao et al., 2006a). Dopita et al. (2006) proposed that the metallicity-dependence of stellar atmospheres causes the anti-correlation. When the

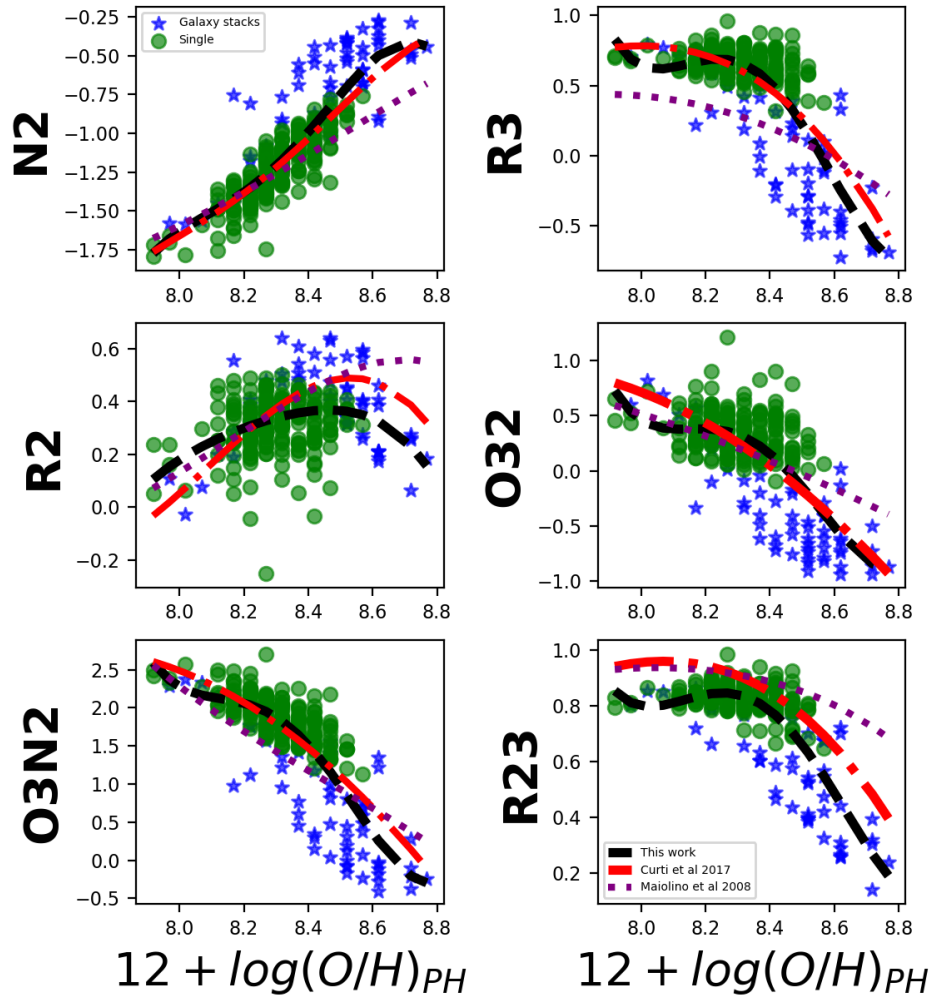


Figure 5.5. Strong line diagnostics as a function of $12 + \log(O/H)_{PH}$ for the best models: blue stars represent the best models strong line ratios values for observed galaxy stacks while the green circles show the best models for single galaxies. Our best fit polynomial functions are shown as solid black curves, while the purple dotted line represents semi-empirical (Maiolino et al., 2008) and the red dashed line demonstrates the observational Curti et al. (2017) calibrations.

Table 5.1. Best fit coefficients for calibrations of $12 + \log(O/H)_{PH}$ diagnostics given by equation (5.5).

		C_0	C_1	C_2	C_3	C_4
Diagnostics	N2	-0.41 ± 0.04	0.56 ± 0.65	-9.53 ± 3.82	-19.34 ± 8.32	-11.63 ± 5.82
	R3	-0.52 ± 0.06	-3.44 ± 0.86	7.63 ± 5.10	31.82 ± 11.10	24.73 ± 7.77
	R2	0.26 ± 0.03	-1.12 ± 0.45	-3.92 ± 2.67	-5.01 ± 5.82	-2.81 ± 4.07
	O32	-0.78 ± 0.08	-2.32 ± 1.13	11.55 ± 6.65	36.83 ± 14.48	27.54 ± 10.14
	O3N2	-0.1 ± 0.105	-4.0 ± 1.47	17.17 ± 8.65	51.16 ± 18.84	36.37 ± 13.19
	R23	0.3 ± 0.02	-1.81 ± 0.33	1.72 ± 1.98	11.04 ± 4.32	8.97 ± 3.02

stellar wind has a high metallicity, it has a higher metal opacity and absorbs a larger fraction of the ionizing photons, leaving fewer high energetic photons to ionize the surrounding HII region. Metal-rich stellar atmospheres also scatter photons from the photosphere more efficiently than metal-poor atmospheres. This process more efficiently converts luminous energy to mechanical energy in the stellar wind region, reducing the number of ionizing photons incident on the HII region (Kewley et al., 2019). By contrast, some other studies show that the metallicity and ionization parameter either have a positive correlation or have no obvious correlation in observed HII regions Kreckel et al. (2019); Zinchenko et al. (2019); Mingozzi et al. (2020b); Ji, Yan (2022); Grasha et al. (2022).

In Fig.5.6 we present the relation between metallicity and the average ionisation parameter (U_{avr}) calculated for our best-fit models. We utilize an approach for robust linear regression using repeated medians to fit a line to best models average ionisation parameter and best model metallicity values SIEGEL (1982). We find an anti-correlation between these two parameters, more evident at high metallicity, in good agreement with Dopita et al. (2006).

In a close accord with (Dopita, Evans, 1986; Maier et al., 2006) finding, at low metallicity regime, the best models represents a much mildly anti-correlation with higher average ionisation parameter.

We report our fits also in three different cases:

$$\log(U_{avr}) = 2.86 - 0.62 \times \log(z) \text{ single galaxy} \quad (5.15)$$

$$\log(U_{avr}) = 10.98 - 1.66 \times \log(z) \text{ stacks galaxy} \quad (5.16)$$

$$\log(U_{avr}) = 11.76 - 1.70 \times \log(z) \text{ all galaxies} \quad (5.17)$$

The ionization parameter is possible to estimated empirically by comparing two emission lines from the same atomic species in different ionization states. One of these more popular ionisation parameter diagnostics in the optical wavelength range is based on the $[OIII]\lambda 5007/[OII]\lambda 3726,29$ ratio(Kewley, Dopita, 2002a; Kobulnicky, Kewley, 2004b). Unfortunately, this ratio also shows a non-negligible secondary dependence on the the gas-phase metallicity. In Fig.5.7, we present our average U_{avr} for the best models as a function of observed O32. The black solid line represents a second-degree polynomial fit given by:

$$\log(U_{avr}) = -2.72(\pm 0.02) + 1.19(\pm 0.03) \times O32 + 0.44(\pm 0.07) \times O32^2. \quad (5.18)$$

The red and yellow solid lines are theoretical calibrations proposed by Kewley, Dopita (2002a) which covers ionisation parameter between -3.98 and -1.98 at metallicity 7.63 to 8.93. Also, to estimate ionisation parameter they considered a bi-cube fit between ionisation parameter and simultaneously both o32 emission lines and metallicity parameter.

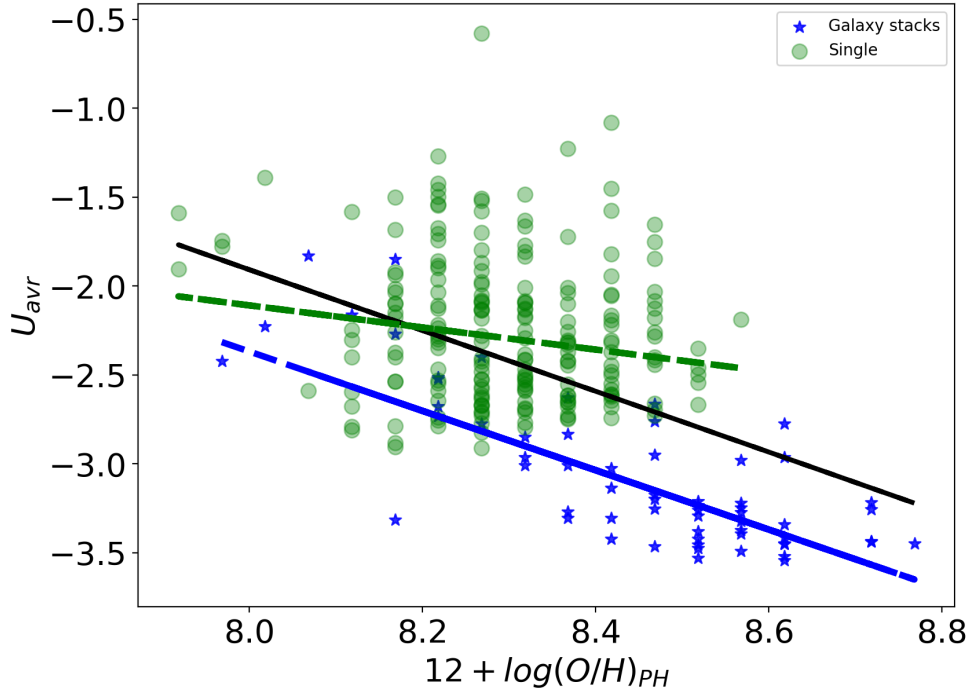


Figure 5.6. The average ionisation parameter (U_{avr}) for the best models as a function of metallicity. There is a negative correlation between these two parameter. The anti-correlation appears steeper at high metallicity, while at low metallicity the relation appears to flatten. The black line demonstrates a fit on the whole data, while green and blue are individual fit to best models for single galaxies and galaxy stacks, respectively.

5.1.6 Model Metallicity deviation from T_e

The Fig.5.8 is shown the comparisons between the best model metallicity, $12 + \log(O/H)_{PH}$, and the values obtained from the T_e method. The T_e model-based abundances were estimated using the emission lines of best models covering all possible excitation conditions by Pyneb. It is important to note that no extra efforts were made to obtain this agreement between the metallicity abundances from the models, $12 + \log(O/H)_{PH}$, and the metallicity derived from the direct method, but it arises in a natural way when a consistent set of atomic data, realistic geometrical conditions, and an updated code and SEDs are used. The agreement is very

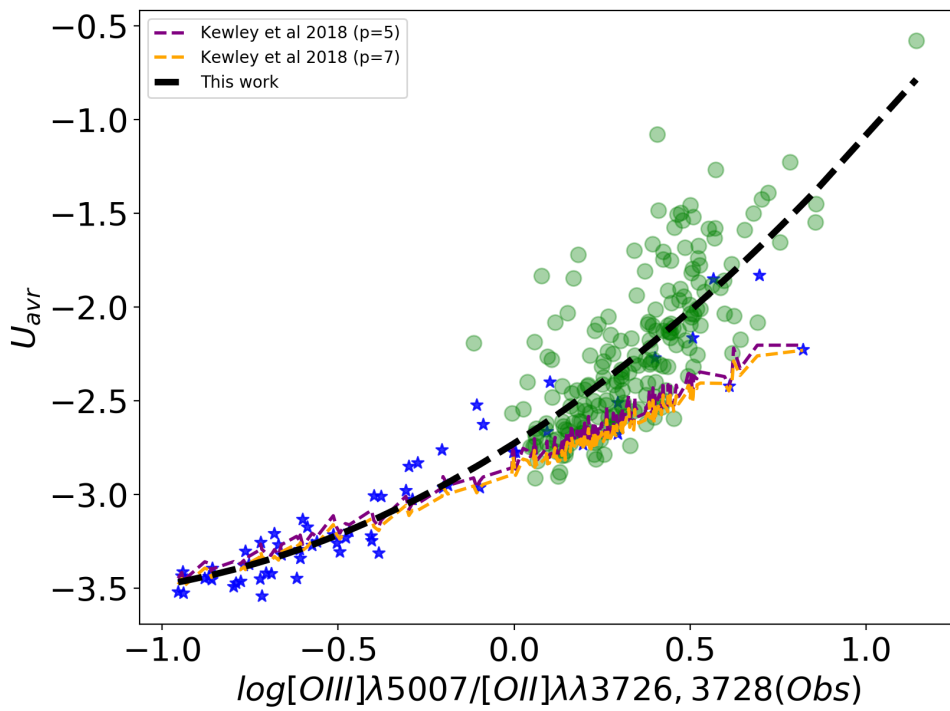


Figure 5.7. The average ionisation parameter (U_{avr}) for the best models as a function of the observed O32 strong line ratio. Solid red and yellow dotted lines correspond to ISM pressures $\log(P/K) = 5$ and $\log(P/K) = 7$, respectively Kewley, Dopita (2002a), while the black dotted line shows our best fit.

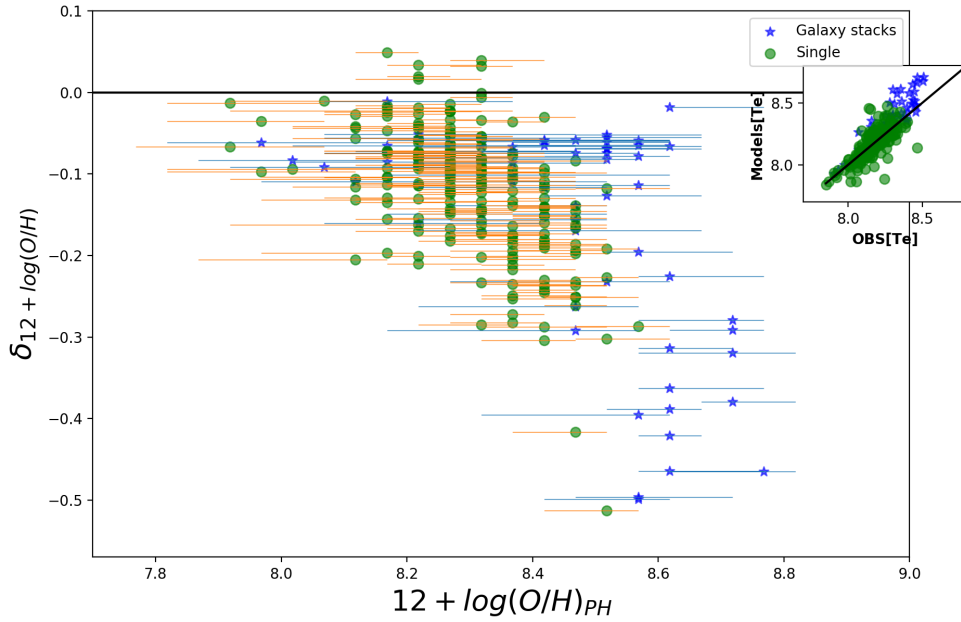


Figure 5.8. The difference between $12 + \log(O/H)_{PH}$ and its T_e metallicity for the best models (y-axis) as a function of $12 + \log(O/H)_{PH}$. The blue stars are representing the best models for galaxy stacks and the green circles are showing the best single galaxies' models. The difference between T_e and $12 + \log(O/H)_{PH}$ metallicities is increasing toward to high metallicity. The small box is showing the relation between best models T_e metallicity and observed T_e metallicity estimation. The black solid line represents a one by one relation.

good at low metallicity. However, this dispersion is higher for $12 + \log(O/H) > 8.5$. This behaviour demonstrates two things. First, $[OIII]\lambda 4363$ is the main discriminator between low metallicity and high metallicity objects independently of their excitation or geometrical conditions. Secondly, different conditions of metallicity and/or excitation lead to similar sets of emission line fluxes if we consider with the same probability the whole space of possible values for each parameter.

5.1.7 Lacking of Auroral lines on model constrain

To investigate on the multi-cloud approach in objects with no detection of any auroral lines to derive chemical abundances and how it leads to values consistent with considering auroral lines, we apply our method with the same conditions but without considering auroral lines to find the best models regarded to our observational samples.

The best models metallicity, $12 + \log(O/H)_{PH}$, for single galaxies are extremely comparable in both scenarios, whether or not auroral lines are taken into account, as shown in Fig.5.9. The discrepancies are rising for galaxy stacks.

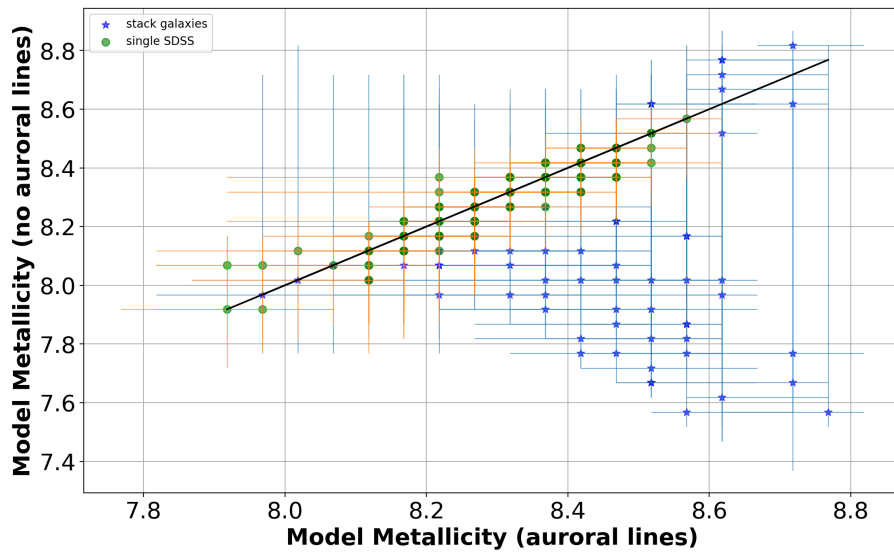


Figure 5.9. The difference between the best models metallicity estimation when we consider auroral lines or not to find the best models, according to observations. Although the best models for single galaxies represents less dependency to auroral lines, there are more influence on stacked galaxies.

Chapter 6

Summary and Conclusions

We have presented a new approach to modelling emission lines from photoionized gas which allows to reproduce observed line ratios from a wide range of ionization and with an accuracy better than 10%, and whose main application is the accurate determination of gas metallicity. Our approach is based on the weighted combination of multiple single cloud photoionization models computed with CLOUDY. The novelty of our approach is in the weights of the single cloud models, which are not parametric nor assumed a priori, but are free parameters of the fit. Since observed line luminosities are integral quantities over the entire volume of the emitting source, the single cloud models contributing to a best fit do not necessarily correspond to physical entities but are the basic *building blocks* of the model. Therefore if a best fit model has a single cloud with specific U , N_{H} , this does not necessarily mean that such cloud exists but that the total line emission has a contribution from gas with those physical parameters, regardless of where and how it is spatially distributed.

Our model has as many free parameters as the single cloud models considered, however the fitting of the observed data is not degenerate and the loss function (\mathcal{L}) curves computed as a function of gas metallicity have very deep and well defined minima. Indeed our approach is similar to the one used for fitting the stellar continua of galaxies, where many hundreds of templates can be combined with weights which are free parameters in the fit. We have shown that our approach provides a significant improvement compared to the single cloud, constant pressure models commonly used in the literature. Overall, our method provides a new accurate tool to estimate the metallicity and the physical conditions of the ionized gas. It can be applied in many different science cases and wherever there are emission lines from photoionized gas. Some of these applications of our method will be addressed in future works.

We have also shown that a critical point for our modelling is to allow for different abundances for elements like N and S than those used in the photoionisation calculations: N and S emission lines are not major coolants of the photoionized region like O lines and therefore their luminosities scale linearly with gas abundances. Not accounting for N and S abundance variations can significantly affect the quality of the fit (with minimum \mathcal{L} values worse by even a couple of orders of magnitude) and the estimated gas metallicity.

To show the performance of new multiple-cloud approach, we applied this novel investigation to both HII regions and star-forming galaxies.

Multi-cloud approach on HII regions

In our first paper of the thesis (A.Marconi, A.Amiri et al. 2023), we have applied our model to the HII regions from the samples by Zurita et al. (2021) and from the CHAOS project (Berg et al. (2015a); Croxall et al. (2015a, 2016a); Berg et al. (2020); Rogers et al. (2021, 2022)).

For the sample by Zurita et al. (2021), we have considered HII regions where all the following lines were detected with $S/N > 5$: [OII] $\lambda\lambda$ 3726,3729, [OIII] $\lambda\lambda$ 4959,5007, [NII] $\lambda\lambda$ 6548,6583, $H\alpha$, [SII] $\lambda\lambda$ 6717,6731, [SIII] $\lambda\lambda$ 9069,9532, [SII] $\lambda\lambda$ 4068,4076, [OIII] λ 4363, [NII] λ 5755, [SIII] λ 6312, and [OII] $\lambda\lambda$ 7320, 7330. All the observed emission lines for the 24 selected HII regions were reproduced by the model to better than 10%. In particular the model was able to reproduce also the [SIII] lines which are well known to be problematic in the previous generation of single-cloud models. The T_e -metallicities derived from the observations and those derived from the model agree to within 0.05 dex, another indication of the extremely good performance of the models. We also showed that T_e -metallicities suffer from uncertainties which are related to the simplified assumptions underlying the method: the T_e metallicities computed from the emission lines predicted by the models can be 0.2 dex smaller than the real gas metallicities of the models themselves.

The CHAOS sample is more homogeneous in terms of data quality, is characterised by better S/N and provides the fluxes of many more emission lines. Overall, we have modeled the same emission lines used for the Zurita et al. (2021) sample but we have added also other lines, doubling their total number. Even with these increased constraints, the models reproduce the observed emission lines to better than 10%. It is worth noting that the model is able to reproduce the emission lines from very different ionization stages, like [OI], [OII] and [OIII].

Finally, we have shown that the gas metallicities estimated with our models in HII regions of the Milky Way are in better agreement with the stellar metallicities (average lower by 0.1 dex) than the estimates based on the T_e -method.

Multi-cloud approach on star-forming galaxies

In our second part of this thesis (A.Amiri et al. 2023), we presented the application of our new method to the spectra of galaxies, with the aim of determining their metallicities. We considered a wide span of star-forming galaxies from Curti et al. (2017); Curti et al. (2019) to cover a broad range of dynamical gas-phase metallicities. Our sample is composed of 600 single galaxy spectra (Curti et al., 2019) and 62 stacked spectra, averaging several hundreds of galaxies each (Curti et al., 2017). All the following lines detected with $S/N > 5$, were considered: [OII] $\lambda\lambda$ 3726,3729, [OIII] $\lambda\lambda$ 4959,5007, [NII] $\lambda\lambda$ 6548,6583, $H\alpha$, [SII] $\lambda\lambda$ 6717,6731, [SII] $\lambda\lambda$ 4068,4076, [OIII] λ 4363, [NII] λ 5755, [OI] λ 6300, and [OII] $\lambda\lambda$ 7320, 7330.

All the observed emission lines for the 600 single galaxies and 62 galaxy stacks were reproduced by the model to better than $\sim 10\%$.

The excellent performance of the models is demonstrated by the fact that the T_e -metallicities derived from the observations and those derived from the model agree to within 0.05 dex.

We then used our new method to obtain a new self-consistent calibration of the strong line method, we investigated the reliability of T_e metallicities and confirmed relations between line ratios and ionization parameter and the ionization parameter vs metallicity

anticorrelation in galaxies. In particular, the T_e metallicities computed from the emission lines predicted by the models and the gas-phase metallicities of the models, are discrepant by ~ 0.2 dex and this discrepancy increases at high metallicities. It maybe point out that the T_e -metallicities suffer from uncertainties which are related to the simplified assumptions, particularly with increasing gas-phase metallicity.

6.1 Future developments

In this section, I will provide a few examples of application of our new multiple-cloud model for the determination of gas-phase metallicities and a further assessment of the reliability of the T_e method.

6.1.1 T_e metallicities and calibration of the strong-line method at high redshift

Metallicity provides unique information on the evolution and the physical properties of galaxies. Gas phase metallicity determinations generally rely on adopting locally calibrated strong-line diagnostics, as temperature-sensitive auroral lines are usually too faint to be detected, preventing the use of the more robust and direct electron-temperature (T_e) method. However, it is not clear whether the strong-line calibrations derived in the local universe are valid for distant galaxies, which have drastically different properties. Recently, we have shown that high-redshift galaxies have a different relationship between T_e metallicity and strong-line ratios (Curti et al., 2023).

As shown in Fig 6.1, high-redshift galaxies likely follow a different calibration of the strong line method from the one of the local universe. In order to find which physical properties could affect these changes in calibration, we need to study samples of high- z galaxies with available detection of auroral lines. These will be finally available thanks to the advent of JWST observations.

It will be possible to apply our new multi-component photoionisation model to the JWST spectra to accurately determine metallicities of high red-shift galaxies, to refine T_e metallicity estimates and provide a new calibration of the strong line method for high redshift galaxies. Furthermore, from the best-simulated models, we will be able to extract fundamental parameters of the high redshift ISM, e.g. average ionisation parameter, ionisation temperature and density, and compare them with those of the local galaxies. These results will indicate how parameters such as ionisation parameter and temperature change between the local and higher redshift universe, and whether T_e metallicity measurements are precise enough in higher-redshift galaxies.

6.1.2 Active Galactic Nuclei

Single-zone models compute the ionization structure of a single, ionization-bounded, gas cloud of hydrogen irradiated by a continuum source. Although these models are successful in fitting strong optical lines they fail to reproduce some of the properties of the emission line spectra of AGN, in particular those from the BLR (Broad Line Region) and NLR (Narrow Line Region).

Compared with observations, these models predict too weak high ionization lines such as [NeV] λ 3426, and [FeVII] λ 6087. Moreover, they expect that in the ENLR (Extended NLR) the excitation tends to be even higher than in the NLR, at variance with what one would

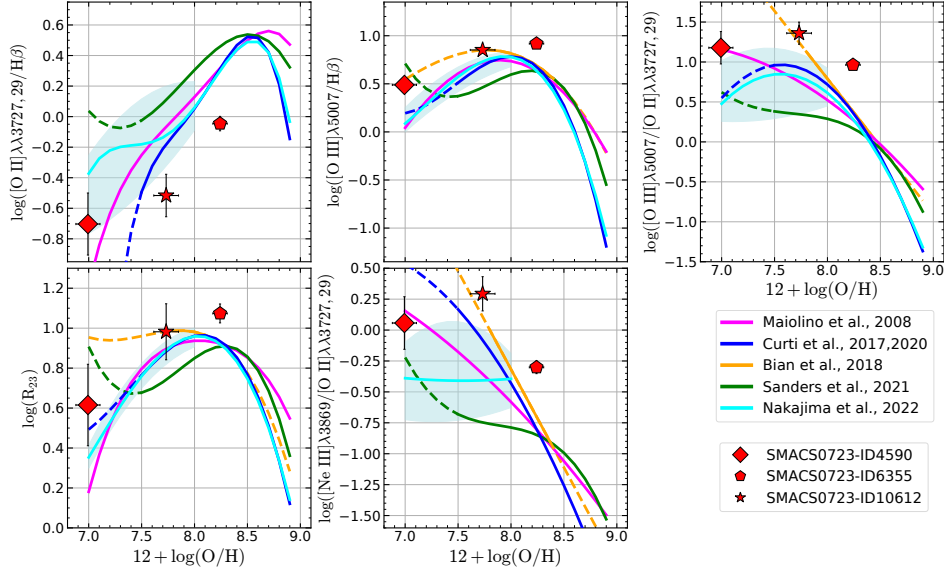


Figure 6.1. The relationships between T_e metallicity and strong-line ratios for the JWST galaxy sample (Curti et al., 2023) are compared with some widely adopted abundance calibrations (Curti et al., 2017; Curti et al., 2019; Maiolino, Mannucci, 2019a; Sanders et al., 2021; Nakajima et al., 2022). All these calibration relations are built from samples of local star-forming galaxies with T_e -based measurements, but are based on slightly different assumptions. Solid lines represent the relationships in the metallicity calibration range as provided by the authors, whereas dashed lines mark extrapolations of the polynomial fit outside that range (courtesy: Mirko Curti).

expect. The single cloud models are unable to account for both high and low ionization lines at the same time and it seems that at least two gas components are responsible for the emission. This can be easily taken into account by our multi cloud approach. Furthermore, we can consider two different approaches: the standard combination of multiple ionization bounded cloud like in this thesis, but also a mix of matter bounded and ionization bounded clouds. The latter approach involves the presence of two distinct classes of clouds: matter-bounded clouds are fully ionized regions of gas whose limits are defined by the presence of matter, conversely ionization-bounded clouds are able to absorb all ionizing photons and their dimensions are set by ionization. Applying our new multi-cloud method to a wide range of observed AGN spectra, we will try to reproduce observed AGN emission lines and address this open issue in AGN spectroscopy.

Bibliography

- Aller Lawrence H.* The Spectra of the Emission Nebulosities in Messier 33. // . I 1942. 95. 52.
- Alloin D., Collin-Souffrin S., Joly M., Vigroux L.* Nitrogen and oxygen abundances in galaxies. // . IX 1979. 78. 200–216.
- Andrews Brett H., Martini Paul.* The Mass-Metallicity Relation with the Direct Method on Stacked Spectra of SDSS Galaxies // . III 2013. 765, 2. 140.
- Arellano-Córdova K. Z., Esteban C., García-Rojas J., Méndez-Delgado J. E.* The Galactic radial abundance gradients of C, N, O, Ne, S, Cl, and Ar from deep spectra of H II regions // . VIII 2020. 496, 2. 1051–1076.
- Arellano-Córdova K. Z., Esteban C., García-Rojas J., Méndez-Delgado J. E.* On the radial abundance gradients of nitrogen and oxygen in the inner Galactic disc // . III 2021. 502, 1. 225–241.
- Asplund Martin, Grevesse Nicolas, Sauval A. Jacques, Scott Pat.* The Chemical Composition of the Sun // . IX 2009. 47, 1. 481–522.
- Baldwin J. A., Phillips M. M., Terlevich R.* Classification parameters for the emission-line spectra of extragalactic objects. // . II 1981. 93. 5–19.
- Belfiore F., Maiolino R., Bundy K., Thomas D., Maraston C., Wilkinson D., Sánchez S. F., Bershady M., Blanc G. A., Bothwell M., Cales S. L., Coccato L., Drory N., Emsellem E., Fu H., Gelfand J., Law D., Masters K., Parejko J., Tremonti C., Wake D., Weijmans A., Yan R., Xiao T., Zhang K., Zheng T., Bizyaev D., Kinemuchi K., Oravetz D., Simmons A.* P-MaNGA Galaxies: emission-lines properties - gas ionization and chemical abundances from prototypal observations // . V 2015. 449, 1. 867–900.
- Berg Danielle A., Pogge Richard W., Skillman Evan D., Croxall Kevin V., Moustakas John, Rogers Noah S. J., Sun Jiayi.* CHAOS IV: Gas-phase Abundance Trends from the First Four CHAOS Galaxies // . IV 2020. 893, 2. 96.
- Berg Danielle A., Skillman Evan D., Croxall Kevin V., Pogge Richard W., Moustakas John, Johnson-Groh Mara.* CHAOS I. Direct Chemical Abundances for H II Regions in NGC 628 // . VI 2015a. 806, 1. 16.
- Berg Danielle A., Skillman Evan D., Croxall Kevin V., Pogge Richard W., Moustakas John, Johnson-Groh Mara.* CHAOS I. Direct Chemical Abundances for H II Regions in NGC 628 // . VI 2015b. 806, 1. 16.

- Berg Danielle A., Skillman Evan D., Henry Richard B. C., Erb Dawn K., Carigi Leticia.* CARBON AND OXYGEN ABUNDANCES IN LOW METALLICITY DWARF GALAXIES* † // *The Astrophysical Journal*. aug 2016. 827, 2. 126.
- Binette L., Matadamas R., Hägele G. F., Nicholls D. C., Magris C. G., Peña-Guerrero M. Á., Morisset C., Rodríguez-González A.* Discrepancies between the [O iii] and [S iii] temperatures in H ii regions // . XI 2012. 547. A29.
- Blanc Guillermo A., Kewley Lisa, Vogt Frédéric P. A., Dopita Michael A.* IZI: Inferring the Gas Phase Metallicity (Z) and Ionization Parameter (q) of Ionized Nebulae Using Bayesian Statistics // . I 2015. 798, 2. 99.
- Borkowski Kazimierz J., Williams Brian J., Reynolds Stephen P., Blair William P., Ghavamian Parviz, Sankrit Ravi, Hendrick Sean P., Long Knox S., Raymond John C., Smith R. Chris, Points Sean, Winkler P. Frank.* Dust Destruction in Type Ia Supernova Remnants in the Large Magellanic Cloud // *The Astrophysical Journal*. apr 2006. 642, 2. L141.
- Bresolin F., Schaerer D., González Delgado R. M., Stasińska G.* A VLT study of metal-rich extragalactic H II regions. I. Observations and empirical abundances // . X 2005. 441, 3. 981–997.
- Brinchmann J., Charlot S., White S. D. M., Tremonti C., Kauffmann G., Heckman T., Brinkmann J.* The physical properties of star-forming galaxies in the low-redshift Universe // . VII 2004. 351, 4. 1151–1179.
- Byler Nell, Dalcanton Julianne J., Conroy Charlie, Johnson Benjamin D.* Nebular Continuum and Line Emission in Stellar Population Synthesis Models // . V 2017. 840, 1. 44.
- Byrne C. M., Stanway E. R., Eldridge J. J., McSwiney L., Townsend O. T.* The dependence of theoretical synthetic spectra on α -enhancement in young, binary stellar populations // . VI 2022. 512, 4. 5329–5338.
- Calzetti Daniela, Armus Lee, Bohlin Ralph C., Kinney Anne L., Koornneef Jan, Storchi-Bergmann Thaisa.* The Dust Content and Opacity of Actively Star-forming Galaxies // . IV 2000. 533, 2. 682–695.
- Cameron Alex J., Katz Harley, Rey Martin P.* A novel approach to correcting T_e -based mass-metallicity relations // arXiv e-prints. X 2022. arXiv:2210.14234.
- Campbell Alison, Terlevich Roberto, Melnick Jorge.* The stellar populations and evolution of H II galaxies - I. High signal-to-noise optical spectroscopy. // . XII 1986. 223. 811–825.
- Cappellari Michele, Emsellem Eric.* Parametric Recovery of Line-of-Sight Velocity Distributions from Absorption-Line Spectra of Galaxies via Penalized Likelihood // . II 2004. 116, 816. 138–147.
- Cappellari Michele, Emsellem Eric.* Parametric Recovery of Line-of-Sight Velocity Distributions from Absorption-Line Spectra of Galaxies via Penalized Likelihood // *Publications of the Astronomical Society of the Pacific*. feb 2004. 116, 816. 138–147.

- Carbon Duane F., Barbu Beatrice, Kraft Robert P., Friel Eileen D., Suntzeff Nicholas B.* Carbon and nitrogen abundances in metal-poor dwarfs of the solar neighborhood. // . V 1987. 99. 335–368.
- Cardelli Jason A., Clayton Geoffrey C., Mathis John S.* The Relationship between Infrared, Optical, and Ultraviolet Extinction // . X 1989. 345. 245.
- Castaneda H. O., Vilchez J. M., Copetti M. V. F.* Density studies on giant extragalactic HII regions. // . VII 1992. 260. 370–380.
- Charlot Stéphane, Longhetti Marcella.* Nebular emission from star-forming galaxies // Monthly Notices of the Royal Astronomical Society. 05 2001. 323, 4. 887–903.
- Chatzikos Marios, Ferland G. J., Williams R. J. R., Porter Ryan, van Hoof P. A. M.* Effects of External Radiation Fields on Line Emission—Application to Star-forming Regions // . XII 2013. 779, 2. 122.
- Croxall Kevin V., Pogge Richard W., Berg Danielle A., Skillman Evan D., Moustakas John.* CHAOS II. Gas-phase Abundances in NGC 5194 // . VII 2015a. 808, 1. 42.
- Croxall Kevin V., Pogge Richard W., Berg Danielle A., Skillman Evan D., Moustakas John.* CHAOS II. Gas-phase Abundances in NGC 5194 // . VII 2015b. 808, 1. 42.
- Croxall Kevin V., Pogge Richard W., Berg Danielle A., Skillman Evan D., Moustakas John.* CHAOS III: Gas-phase Abundances in NGC 5457 // . X 2016a. 830, 1. 4.
- Croxall Kevin V., Pogge Richard W., Berg Danielle A., Skillman Evan D., Moustakas John.* CHAOS III: Gas-phase Abundances in NGC 5457 // . X 2016b. 830, 1. 4.
- Curti M., Cresci G., Mannucci F., Marconi A., Maiolino R., Esposito S.* New fully empirical calibrations of strong-line metallicity indicators in star-forming galaxies // . II 2017. 465, 2. 1384–1400.
- Curti Mirko, D’Eugenio Francesco, Carniani Stefano, Maiolino Roberto, Sandles Lester, Witstok Joris, Baker William M., Bennett Jake S., Piotrowska Joanna M., Tacchella Sandro, Charlot Stephane, Nakajima Kimihiko, Maheson Gabriel, Mannucci Filippo, Amiri Amirnezam, Arribas Santiago, Belfiore Francesco, Bonaventura Nina R., Bunker Andrew J., Chevallard Jacopo, Cresci Giovanni, Curtis-Lake Emma, Hayden-Pawson Connor, Jones Gareth C., Kumari Nimisha, Laseter Isaac, Looser Tobias J., Marconi Alessandro, Maseda Michael V., Scholtz Jan, Smit Renske, Übler Hannah, Wallace Imaan E. B.* The chemical enrichment in the early Universe as probed by JWST via direct metallicity measurements at $z \approx 8$ // . I 2023. 518, 1. 425–438.
- Curti Mirko, Mannucci Filippo, Cresci Giovanni, Maiolino Roberto.* The mass–metallicity and the fundamental metallicity relation revisited on a fully α -based abundance scale for galaxies // Monthly Notices of the Royal Astronomical Society. nov 2019. 491, 1. 944–964.
- Dijkstra Mark, Jeason-Daniel Akila.* Empirical constraints on the star formation and redshift dependence of the Ly α ‘effective’ escape fraction // . XI 2013. 435, 4. 3333–3341.

- Dong Hui, Li Zhiyuan, Wang Q. Daniel, Lauer Tod R., Olsen Knut A. G., Saha Abhijit, Dalcanton Julianne J., Williams Benjamin F.* Photometric evidence of an intermediate-age stellar population in the inner bulge of M31 // . VIII 2015. 451, 4. 4126–4138.
- Dopita M. A., Evans I. N.* Theoretical Models for H II Regions. II. The Extragalactic H II Region Abundance Sequence // . VIII 1986. 307. 431.
- Dopita M. A., Kewley L. J., Heisler C. A., Sutherland R. S.* A Theoretical Recalibration of the Extragalactic H II Region Sequence // *The Astrophysical Journal*. oct 2000. 542, 1. 224.
- Dopita Michael A., Fischera Jörg, Sutherland Ralph S., Kewley Lisa J., Leitherer Claus, Tuffs Richard J., Popescu Cristina C., van Breugel Wil, Groves Brent A.* Modeling the Pan-Spectral Energy Distribution of Starburst Galaxies. III. Emission Line Diagnostics of Ensembles of Evolving H II Regions // . XII 2006. 167, 2. 177–200.
- Dopita Michael A., Kewley Lisa J., Sutherland Ralph S., Nicholls David C.* Chemical abundances in high-redshift galaxies: a powerful new emission line diagnostic // . II 2016. 361. 61.
- Dors Jr O. L., Krabbe Angela, Hägele Guillermo F., Pérez-Montero Enrique.* Analysing derived metallicities and ionization parameters from model-based determinations in ionized gaseous nebulae // *Monthly Notices of the Royal Astronomical Society*. 08 2011. 415, 4. 3616–3626.
- Draine B. T.* Interstellar Dust Models and Evolutionary Implications // *Cosmic Dust - Near and Far*. 414. XII 2009. 453. (Astronomical Society of the Pacific Conference Series).
- Draine B. T., Salpeter E. E.* On the physics of dust grains in hot gas. // . VII 1979. 231. 77–94.
- Draine Bruce T.* Evolution of interstellar dust. // *The Evolution of the Interstellar Medium*. 12. I 1990. 193–205. (Astronomical Society of the Pacific Conference Series).
- Dunne Loretta, Eales Stephen A., Edmunds M. G.* A census of metals at high and low redshift and the connection between submillimetre sources and spheroid formation // *Monthly Notices of the Royal Astronomical Society*. 05 2003. 341, 2. 589–598.
- Dwek Eli, Arendt Richard G.* Dust-gas interactions and the infrared emission from hot astrophysical plasmas. // . I 1992. 30. 11–50.
- Dwek Eli, Cherchneff Isabelle.* THE ORIGIN OF DUST IN THE EARLY UNIVERSE: PROBING THE STAR FORMATION HISTORY OF GALAXIES BY THEIR DUST CONTENT // *The Astrophysical Journal*. jan 2011. 727, 2. 63.
- Edmunds M. G., Pagel B. E. J.* Nitrogen synthesis and the ‘age’ of galaxies // *Monthly Notices of the Royal Astronomical Society*. 11 1978. 185, 1. 77P–80P.
- Eldridge John J., Izzard Robert G., Tout Christopher A.* The effect of massive binaries on stellar populations and supernova progenitors // *Monthly Notices of the Royal Astronomical Society*. 07 2008. 384, 3. 1109–1118.

- Eldridge John J., Stanway Elizabeth R.* The effect of stellar evolution uncertainties on the rest-frame ultraviolet stellar lines of C IV and He II in high-redshift Lyman-break galaxies // . I 2012. 419, 1. 479–489.
- Esteban C., García-Rojas J., Mesa-Delgado A., Toribio San Cipriano L.* Deep high spectral resolution spectroscopy and chemical composition of ionized nebulae // *Astronomische Nachrichten*. I 2014. 335, 1. 73.
- Esteban C., Méndez-Delgado J. E., García-Rojas J., Arellano-Córdova K. Z.* About Metallicity Variations in the Local Galactic Interstellar Medium // . VI 2022. 931, 2. 92.
- Fabian A. C.* Observational Evidence of Active Galactic Nuclei Feedback // . IX 2012. 50. 455–489.
- Ferland G. J., Chatzikos M., Guzmán F., Lykins M. L., van Hoof P. A. M., Williams R. J. R., Abel N. P., Badnell N. R., Keenan F. P., Porter R. L., Stancil P. C.* The 2017 Release Cloudy // . X 2017. 53. 385–438.
- Ferland G. J., Porter R. L., van Hoof P. A. M., Williams R. J. R., Abel N. P., Lykins M. L., Shaw G., Henney W. J., Stancil P. C.* The 2013 Release of Cloudy // . IV 2013. 49. 137–163.
- Fraternali Filippo.* Gas Accretion via Condensation and Fountains // *Gas Accretion onto Galaxies*. 430. I 2017. 323. (Astrophysics and Space Science Library).
- Garnett Donald R.* Nitrogen in Irregular Galaxies // . XI 1990. 363. 142.
- Garnett Donald R.* Electron Temperature Variations and the Measurement of Nebular Abundances // . IV 1992. 103. 1330.
- Gehrz Robert D.* Sources of Stardust in the Galaxy // *Interstellar Dust*. Dordrecht: Springer Netherlands, 1989. 445–453.
- Girardi L., Bressan A., Bertelli G., Chiosi C.* Evolutionary tracks and isochrones for low- and intermediate-mass stars: From 0.15 to 7 M_{sun} , and from $Z=0.0004$ to 0.03 // . II 2000. 141. 371–383.
- Gordon Karl D., Clayton Geoffrey C., Misselt K. A., Landolt Arlo U., Wolff Michael J.* A Quantitative Comparison of the Small Magellanic Cloud, Large Magellanic Cloud, and Milky Way Ultraviolet to Near-Infrared Extinction Curves // . IX 2003. 594, 1. 279–293.
- Grasha K., Chen Q. H., Battisti A. J., Acharyya A., Ridolfo S., Poehler E., Mably S., Verma A. A., Hayward K. L., Kharbanda A., Poetrodjojo H., Seibert M., Rich J. A., Madore B. F., Kewley L. J.* Metallicity, Ionization Parameter, and Pressure Variations of H II Regions in the TYPHOON Spiral Galaxies: NGC 1566, NGC 2835, NGC 3521, NGC 5068, NGC 5236, and NGC 7793 // . IV 2022. 929, 2. 118.
- Grevesse N., Asplund M., Sauval A. J., Scott P.* The chemical composition of the Sun // . VII 2010. 328, 1-2. 179–183.
- Groves Brent A., Dopita Michael A., Sutherland Ralph S.* Dusty, Radiation Pressure-Dominated Photoionization. I. Model Description, Structure, and Grids // . VII 2004. 153, 1. 9–73.

- Guseva N. G., Izotov Y. I., Stasińska G., Fricke K. J., Henkel C., Papaderos P.* VLT spectroscopy of low-metallicity emission-line galaxies: abundance patterns and abundance discrepancies // . V 2011. 529. A149.
- Henry R. B. C., Edmunds M. G., Köppen J.* On the Cosmic Origins of Carbon and Nitrogen // . X 2000. 541, 2. 660–674.
- Izotov Y. I., Stasińska G., Meynet G., Guseva N. G., Thuan T. X.* The chemical composition of metal-poor emission-line galaxies in the Data Release 3 of the Sloan Digital Sky Survey // . III 2006. 448, 3. 955–970.
- Izotov Yuri I., Stasinska Grazyna, Guseva N. G., Thuan Trinh X.* Abundance patterns in the low-metallicity emission-line galaxies from the Early Data Release of the Sloan Digital Sky Survey // *Astronomy and Astrophysics - A&A.* 2004. 415. 87–94.
- Izotov Yuri I., Thuan Trinh X.* Heavy-Element Abundances in Blue Compact Galaxies // . II 1999a. 511, 2. 639–659.
- Izotov Yuri I., Thuan Trinh X.* Heavy-Element Abundances in Blue Compact Galaxies // . II 1999b. 511, 2. 639–659.
- Izotov Yuri I., Thuan Trinh X., Wilson John C.* NEAR-INFRARED SPECTROSCOPY OF THE BLUE COMPACT DWARF GALAXY MARKARIAN 59 // *The Astrophysical Journal.* sep 2009. 703, 2. 1984.
- Ji Xihan, Yan Renbin.* Correlation between the gas-phase metallicity and ionization parameter in extragalactic H II regions // . III 2022. 659. A112.
- Kauffmann Guinevere, Heckman Timothy M., Tremonti Christy, Brinchmann Jarle, Charlot Stéphane, White Simon D. M., Ridgway Susan E., Brinkmann Jon, Fukugita Masataka, Hall Patrick B., Ivezić Željko, Richards Gordon T., Schneider Donald P.* The host galaxies of active galactic nuclei // . XII 2003. 346, 4. 1055–1077.
- Kelly Patrick L., Fox Ori D., Filippenko Alexei V., Cenko S. Bradley, Prato Lisa, Schaefer Gail, Shen Ken J., Zheng WeiKang, Graham Melissa L., Tucker Brad E.* Constraints on the Progenitor System of the Type Ia Supernova 2014J from Pre-explosion Hubble Space Telescope Imaging // . VII 2014. 790, 1. 3.
- Kewley L. J., Dopita M. A.* Using Strong Lines to Estimate Abundances in Extragalactic H II Regions and Starburst Galaxies // . IX 2002a. 142, 1. 35–52.
- Kewley L. J., Dopita M. A.* Using Strong Lines to Estimate Abundances in Extragalactic H II Regions and Starburst Galaxies // . IX 2002b. 142, 1. 35–52.
- Kewley L. J., Dopita M. A., Sutherland R. S., Heisler C. A., Trevena J.* Theoretical Modeling of Starburst Galaxies // . VII 2001. 556, 1. 121–140.
- Kewley Lisa J., Ellison Sara L.* Metallicity Calibrations and the Mass-Metallicity Relation for Star-forming Galaxies // . VII 2008. 681, 2. 1183–1204.
- Kewley Lisa J., Nicholls David C., Sutherland Ralph S.* Understanding Galaxy Evolution Through Emission Lines // . VIII 2019. 57. 511–570.

- Kobayashi Chiaki, Umeda Hideyuki, Nomoto Ken'ichi, Tominaga Nozomu, Ohkubo Takuya.* Galactic Chemical Evolution: Carbon through Zinc // . XII 2006. 653, 2. 1145–1171.
- Kobulnicky Henry A., Kewley Lisa J.* Metallicities of $0.3 < z < 1.0$ Galaxies in the GOODS-North Field // . XII 2004a. 617, 1. 240–261.
- Kobulnicky Henry A., Kewley Lisa J.* Metallicities of $0.3 < z < 1.0$ Galaxies in the GOODS-North Field // . XII 2004b. 617, 1. 240–261.
- Kozasa T., Nozawa T., Tominaga N., Umeda H., Maeda K., Nomoto K.* Dust in Supernovae: Formation and Evolution // Cosmic Dust - Near and Far. 414. XII 2009. 43. (Astronomical Society of the Pacific Conference Series).
- Kreckel K., Ho I. T., Blanc G. A., Groves B., Santoro F., Schinnerer E., Bigiel F., Chevance M., Congiu E., Emsellem E., Faesi C., Glover S. C. O., Grasha K., Kruijssen J. M. D., Lang P., Leroy A. K., Meidt S. E., McElroy R., Pety J., Rosolowsky E., Saito T., Sandstrom K., Sanchez-Blazquez P., Schrubba A.* Mapping Metallicity Variations across Nearby Galaxy Disks // . XII 2019. 887, 1. 80.
- Kroupa Pavel.* On the variation of the initial mass function // . IV 2001. 322, 2. 231–246.
- Lara-López Maritza A., R. López-Sánchez Ángel, Hopkins Andrew M.* ERRATUM: “ON THE THREE-DIMENSIONAL STRUCTURE OF THE MASS, METALLICITY, AND STAR FORMATION RATE SPACE FOR STAR-FORMING GALAXIES” (2013, ApJ, 764, 178) // The Astrophysical Journal. feb 2014. 782, 2. 120.
- Levesque Emily M., Kewley Lisa J., Larson Kirsten L.* Theoretical Modeling of Star-Forming Galaxies. I. Emission-Line Diagnostic Grids for Local and Low-Metallicity Galaxies // . II 2010. 139, 2. 712–727.
- Luridiana V., Morisset C., Shaw R. A.* PyNeb: a new tool for analyzing emission lines. I. Code description and validation of results // . I 2015a. 573. A42.
- Luridiana V., Morisset C., Shaw R. A.* PyNeb: a new tool for analyzing emission lines. I. Code description and validation of results // . I 2015b. 573. A42.
- Luridiana Valentina, Morisset Christophe, Shaw Richard A.* PyNeb: a new software for the analysis of emission lines // Proceedings of the International Astronomical Union. 2011. 7, S283. 422–423.
- Maier C., Lilly S. J., Carollo C. M., Meisenheimer K., Hippelein H., Stockton A.* Erratum: “Oxygen Gas Abundances at $z \approx 1.4$: Implications for the Chemical Evolution History of Galaxies” (ApJ, 639, 858 [2006]) // The Astrophysical Journal. may 2006. 643, 1. 584.
- Maiolino R., Mannucci F.* De re metallica: the cosmic chemical evolution of galaxies // . II 2019a. 27, 1. 3.
- Maiolino R., Mannucci F.* De re metallica: the cosmic chemical evolution of galaxies // . II 2019b. 27, 1. 3.

- Maiolino R., Nagao T., Grazian A., Cocchia F., Marconi A., Mannucci F., Cimatti A., Pipino A., Ballero S., Calura F., Chiappini C., Fontana A., Granato G. L., Matteucci F., Pastorini G., Pentericci L., Risaliti G., Salvati M., Silva L. AMAZE. I. The evolution of the mass-metallicity relation at $z > 3$ // . IX 2008. 488, 2. 463–479.
- Mannucci F., Belfiore F., Curti M., Cresci G., Maiolino R., Marasco A., Marconi A., Mingozzi M., Tozzi G., Amiri A. The diffuse ionized gas (DIG) in star-forming galaxies: the influence of aperture effects on local H II regions // . XII 2021. 508, 2. 1582–1589.
- Mannucci F., Cresci G., Maiolino R., Marconi A., Gnerucci A. A fundamental relation between mass, star formation rate and metallicity in local and high-redshift galaxies // . XI 2010. 408, 4. 2115–2127.
- Marino R. A., Rosales-Ortega F. F., Sánchez S. F., Gil de Paz A., Vílchez J., Miralles-Caballero D., Kehrig C., Pérez-Montero E., Stanishev V., Iglesias-Páramo J., Díaz A. I., Castillo-Morales A., Kennicutt R., López-Sánchez A. R., Galbany L., García-Benito R., Mast D., Mendez-Abreu J., Monreal-Ibero A., Husemann B., Walcher C. J., García-Lorenzo B., Masegosa J., Del Olmo Orozco A., Mourão A. M., Ziegler B., Mollá M., Papaderos P., Sánchez-Blázquez P., González Delgado R. M., Falcón-Barroso J., Roth M. M., van de Ven G., CALIFA Team . The O3N2 and N2 abundance indicators revisited: improved calibrations based on CALIFA and T_e -based literature data // . XI 2013. 559. A114.
- Martin Crystal L. Mapping Large-Scale Gaseous Outflows in Ultraluminous Galaxies with Keck II ESI Spectra: Variations in Outflow Velocity with Galactic Mass // . III 2005. 621, 1. 227–245.
- Mathis John S., Liu X.-W. Observations of the [O III] 4931/4959 Line Ratio and O+2 Abundances in Ionized Nebulae // The Astrophysical Journal. aug 1999. 521, 1. 212.
- Matsuura M., Dwek E., Barlow M. J., Babler B., Baes M., Meixner M., Cernicharo José, Clayton Geoff C., Dunne L., Fransson C., Fritz Jacopo, Gear Walter, Gomez H. L., Groenewegen M. A. T., Indebetouw R., Ivison R. J., Jerkstrand A., Leboutteiller V., Lim T. L., Lundqvist P., Pearson C. P., Roman-Duval J., Royer P., Staveley-Smith Lister, Swinyard B. M., Hoof P. A. M. van, Loon J. Th. van, Verstappen Joris, Wesson Roger, Zanardo Giovanna, Blommaert Joris A. D. L., Decin Leen, Reach W. T., Sonneborn George, Steene Griet C. Van de, Yates Jeremy A. A STUBBORNLY LARGE MASS OF COLD DUST IN THE EJECTA OF SUPERNOVA 1987A* // The Astrophysical Journal. feb 2015. 800, 1. 50.
- McConnell Nicholas J., Ma Chung-Pei. Revisiting the Scaling Relations of Black Hole Masses and Host Galaxy Properties // . II 2013. 764, 2. 184.
- McGaugh Stacy S. H II Region Abundances: Model Oxygen Line Ratios // . X 1991. 380. 140.
- Méndez-Delgado J. E., Amayo A., Arellano-Córdova K. Z., Esteban C., García-Rojas J., Carigi L., Delgado-Inglada G. Gradients of chemical abundances in the Milky Way from H II regions: distances derived from Gaia EDR3 parallaxes and temperature inhomogeneities // . III 2022. 510, 3. 4436–4455.

- Mingozi M., Belfiore F., Cresci G., Bundy K., Bershadly M., Bizyaev D., Blanc G., Boquien M., Drory N., Fu H., Maiolino R., Riffel R., Schaefer A., Storchi-Bergmann T., Telles E., Tremonti C., Zakamska N., Zhang K. SDSS IV MaNGA: Metallicity and ionisation parameter in local star-forming galaxies from Bayesian fitting to photoionisation models // . IV 2020a. 636. A42.
- Mingozi M., Belfiore F., Cresci G., Bundy K., Bershadly M., Bizyaev D., Blanc G., Boquien M., Drory N., Fu H., Maiolino R., Riffel R., Schaefer A., Storchi-Bergmann T., Telles E., Tremonti C., Zakamska N., Zhang K. SDSS IV MaNGA: Metallicity and ionisation parameter in local star-forming galaxies from Bayesian fitting to photoionisation models // . IV 2020b. 636. A42.
- Mo Houjun, Bosch Frank van den, White Simon. Galaxy Formation and Evolution. 2010.
- Mollá M., Díaz Á. I., Cavichia O., Gibson B. K., Maciel W. J., Costa R. D. D., Ascasibar Y., Few C. G. The time evolution of the Milky Way's oxygen abundance gradient // . I 2019. 482, 3. 3071–3088.
- Morgan H. L., Edmunds M. G. Dust formation in early galaxies // . VIII 2003. 343, 2. 427–442.
- Morisset C., Delgado-Inglada G., Sánchez S. F., Galbany L., García-Benito R., Husemann B., Marino R. A., Mast D., Roth M. M. Photoionization models of the CALIFA H II regions. I. Hybrid models // . X 2016. 594. A37.
- Morisset Christophe. pyCloudy: Tools to manage astronomical Cloudy photoionization code. IV 2013. ascl:1304.020.
- Mouri Hideaki, Taniguchi Yoshiaki. Grain Survival in Supernova Remnants and Herbig-Haro Objects // . V 2000. 534, 1. L63–L66.
- Moustakas John, Kennicutt Jr. Robert C., Tremonti Christy A., Dale Daniel A., Smith John-David T., Calzetti Daniela. Optical Spectroscopy and Nebular Oxygen Abundances of the Spitzer/SINGS Galaxies // . X 2010. 190, 2. 233–266.
- Nagao T., Maiolino R., Marconi A. Gas metallicity diagnostics in star-forming galaxies // . XI 2006a. 459, 1. 85–101.
- Nagao T., Maiolino R., Marconi A. Gas metallicity diagnostics in star-forming galaxies // . XI 2006b. 459, 1. 85–101.
- Nakajima Kimihiko, Ouchi Masami, Xu Yi, Rauch Michael, Harikane Yuichi, Nishigaki Moka, Isobe Yuki, Kusakabe Haruka, Nagao Tohru, Ono Yoshiaki, Onodera Masato, Sugahara Yuma, Kim Ji Hoon, Komiyama Yutaka, Lee Chien-Hsiu, Zahedy Fakhri S. EMPRESS. V. Metallicity Diagnostics of Galaxies over $12 + \log(\text{O}/\text{H})$ 6.9–8.9 Established by a Local Galaxy Census: Preparing for JWST Spectroscopy // . IX 2022. 262, 1. 3.
- Netzer Hagai. Testing broad-line region models with reverberation mapping // . V 2020. 494, 2. 1611–1621.
- Nicholls David C., Sutherland Ralph S., Dopita Michael A., Kewley Lisa J., Groves Brent A. Abundance scaling in stars, nebulae and galaxies // . IV 2017. 466, 4. 4403–4422.

- Nozawa Takaya, Kozasa Takashi, Habe Asao.* Dust Destruction in the High-Velocity Shocks Driven by Supernovae in the Early Universe // *The Astrophysical Journal*. sep 2006. 648, 1. 435.
- Nozawa Takaya, Maeda Keiichi, Kozasa Takashi, Tanaka Masaomi, Nomoto Ken'ichi, Umeda Hideyuki.* FORMATION OF DUST IN THE EJECTA OF TYPE Ia SUPERNOVAE // *The Astrophysical Journal*. jul 2011. 736, 1. 45.
- O'Donnell James E.* R v-dependent Optical and Near-Ultraviolet Extinction // . II 1994. 422. 158.
- Omukai K., Tsuribe T., Schneider R., Ferrara A.* Thermal and Fragmentation Properties of Star-forming Clouds in Low-Metallicity Environments // . VI 2005. 626, 2. 627–643.
- Onaka T., Kamijo F.* Destruction of interstellar grains by sputtering. // . III 1978. 64, 1-2. 53–60.
- Pagel B. E. J., Edmunds M. G., Blackwell D. E., Chun M. S., Smith G.* On the composition of H II regions in southern galaxies - I. NGC 300 and 1365. // . X 1979. 189. 95–113.
- Peimbert Antonio, Peimbert Manuel.* DENSITIES, TEMPERATURES, PRESSURES, AND ABUNDANCES DERIVED FROM Oii RECOMBINATION LINES IN Hii REGIONS AND THEIR IMPLICATIONS // *The Astrophysical Journal*. nov 2013. 778, 2. 89.
- Peimbert M., Storey P. J., Torres-Peimbert S.* The O ++/H + Abundance Ratio in Gaseous Nebulae Derived from Recombination Lines // . IX 1993. 414. 626.
- Peimbert Manuel.* Temperature Determinations of H II Regions // . XII 1967. 150. 825.
- Pérez-Montero E., Amorín R., Sánchez Almeida J., Vílchez J. M., García-Benito R., Kehrig C.* Extreme emission-line galaxies in SDSS - I. Empirical and model-based calibrations of chemical abundances // . VI 2021. 504, 1. 1237–1252.
- Pérez-Montero Enrique, Díaz Angeles I.* Line temperatures and elemental abundances in H II galaxies // . XI 2003. 346, 1. 105–118.
- Pettini Max, Pagel Bernard E. J.* [O iii]/[N ii] as an abundance indicator at high redshift. 03 2004. L59–L63.
- Pettini Max, Pagel Bernard E. J.* [OIII]/[NII] as an abundance indicator at high redshift // . III 2004. 348, 3. L59–L63.
- Pilyugin L. S.* On the relationship between auroral and nebular oxygen line intensities in spectra of H II regions // . VI 2005. 436, 1. L1–L4.
- Pilyugin L. S., Mattsson L., Vílchez J. M., Cedrés B.* On the electron temperatures in high-metallicity HII regions // . IX 2009. 398, 1. 485–496.
- Pilyugin L. S., Vílchez J. M., Cedrés B., Thuan T. X.* The electron temperatures of SDSS high-metallicity giant extragalactic H ii regions // . IV 2010. 403, 2. 896–905.
- Pilyugin Leonid S., Thuan Trinh X., Vílchez José M.* Oxygen abundances in the most oxygen-rich spiral galaxies // . IV 2006a. 367, 3. 1139–1146.

- Pilyugin Leonid S., Thuan Trinh X., Vílchez José M.* Oxygen abundances in the most oxygen-rich spiral galaxies // . IV 2006b. 367, 3. 1139–1146.
- Poetrodjojo Henry, D'Agostino Joshua J, Groves Brent, Kewley Lisa, Ho I-Ting, Rich Jeff, Madore Barry F, Seibert Mark.* The effects of diffuse ionized gas and spatial resolution on metallicity gradients: TYPHOON two-dimensional spectrophotometry of M83 // *Monthly Notices of the Royal Astronomical Society.* 05 2019. 487, 1. 79–96.
- Rogers Noah S. J., Skillman Evan D., Pogge Richard W., Berg Danielle A., Croxall Kevin V., Bartlett Jordan, Arellano-Córdova Karla Z., Moustakas John.* CHAOS. VII. A Large-scale Direct Abundance Study in M33 // . XI 2022. 939, 1. 44.
- Rogers Noah S. J., Skillman Evan D., Pogge Richard W., Berg Danielle A., Moustakas John, Croxall Kevin V., Sun Jiayi.* CHAOS. VI. Direct Abundances in NGC 2403 // . VII 2021. 915, 1. 21.
- SIEGEL ANDREW F.* Robust regression using repeated medians // *Biometrika.* 04 1982. 69, 1. 242–244.
- Sanders Ryan L., Shapley Alice E., Jones Tucker, Reddy Naveen A., Kriek Mariska, Siana Brian, Coil Alison L., Mobasher Bahram, Shivaiei Irene, Davé Romeel, Azadi Mojegan, Price Sedona H., Leung Gene, Freeman William R., Fetherolf Tara, de Groot Laura, Zick Tom, Barro Guillermo.* The MOSDEF Survey: The Evolution of the Mass-Metallicity Relation from $z = 0$ to $z 3.3$ // . VI 2021. 914, 1. 19.
- Savage Blair D., Sembach Kenneth R.* Interstellar Abundances from Absorption-Line Observations with the Hubble Space Telescope // . I 1996. 34. 279–330.
- Schneider N., Bontemps S., Simon R., Jakob H., Motte F., Miller M., Kramer C., Stutzki J.* A new view of the Cygnus X region. KOSMA ^{13}CO 2 to 1, 3 to 2, and ^{12}CO 3 to 2 imaging // . XI 2006. 458, 3. 855–871.
- Silvia Devin W., Smith Britton D., Shull J. Michael.* Numerical Simulations of Supernova Dust Destruction. I. Cloud-crushing and Post-processed Grain Sputtering // . VI 2010. 715, 2. 1575–1590.
- Skillman Evan D., Kennicutt R. C., Hodge P. W.* Oxygen Abundances in Nearby Dwarf Irregular Galaxies // . XII 1989. 347. 875.
- Stanway E. R., Eldridge J. J.* Re-evaluating old stellar populations // . IX 2018. 479, 1. 75–93.
- Stanway Elizabeth R., Eldridge J. J., Becker George D.* Stellar population effects on the inferred photon density at reionization // *Monthly Notices of the Royal Astronomical Society.* 12 2015. 456, 1. 485–499.
- Stasińska Grażyna, Cid Fernandes Roberto, Mateus Abílio, Sodr e Laerte, Asari Natalia V.* Semi-empirical analysis of Sloan Digital Sky Survey galaxies - III. How to distinguish AGN hosts // . IX 2006. 371, 2. 972–982.

- Storchi-Bergmann Thaisa, Calzetti Daniela, Kinney Anne L.* Ultraviolet to Near-Infrared Spectral Distributions of Star-forming Galaxies: Metallicity and Age Effects // . VII 1994. 429. 572.
- Strömberg Bengt.* The Physical State of Interstellar Hydrogen. // . V 1939. 89. 526.
- Tarter C. Bruce, Tucker Wallace H., Salpeter Edwin E.* The Interaction of X-Ray Sources with Optically Thin Environments // . VI 1969. 156. 943.
- Thompson Ian J., Nunes Filomena M.* Nuclear Reactions for Astrophysics: Principles, Calculation and Applications of Low-Energy Reactions. 2009.
- Thuan Trinh X., Izotov Yuri I., Lipovetsky Valentin A.* Heavy Element Abundances in a New Sample of Low-Metallicity Blue Compact Galaxies // . V 1995. 445. 108.
- Todini Paolo, Ferrara Andrea.* Dust formation in primordial Type II supernovae // . VIII 2001. 325, 2. 726–736.
- Tomkin J., Lambert D. L.* Nitrogen abundances in disk and halo dwarfs. // . IV 1984. 279. 220–224.
- Tremonti Christy A., Heckman Timothy M., Kauffmann Guinevere, Brinchmann Jarle, Charlot Stéphane, White Simon D. M., Seibert Mark, Peng Eric W., Schlegel David J., Uomoto Alan, Fukugita Masataka, Brinkmann Jon.* The Origin of the Mass-Metallicity Relation: Insights from 53,000 Star-forming Galaxies in the Sloan Digital Sky Survey // . X 2004. 613, 2. 898–913.
- Tumlinson Jason, Peebles Molly S., Werk Jessica K.* The Circumgalactic Medium // . VIII 2017. 55, 1. 389–432.
- Vazdekis A., Casuso E., Peletier R. F., Beckman J. E.* A New Chemo-evolutionary Population Synthesis Model for Early-Type Galaxies. I. Theoretical Basis // . X 1996. 106. 307.
- Vazdekis A., Koleva M., Ricciardelli E., Röck B., Falcón-Barroso J.* UV-extended E-MILES stellar population models: young components in massive early-type galaxies // . XII 2016. 463, 4. 3409–3436.
- Vila-Costas M. B., Edmunds M. G.* The nitrogen-to-oxygen ratio in galaxies and its implications for the origin of nitrogen. // . XI 1993. 265. 199–212.
- Vincenzo F., Belfiore F., Maiolino R., Matteucci F., Ventura P.* Nitrogen and oxygen abundances in the Local Universe // . VI 2016. 458, 4. 3466–3477.
- Vílchez J. M., Esteban C.* The chemical composition of H ii regions in the outer Galaxy // Monthly Notices of the Royal Astronomical Society. 06 1996. 280, 3. 720–734.
- Weinberg David H., Hernquist Lars, Katz Neal.* Photoionization, Numerical Resolution, and Galaxy Formation // . III 1997. 477, 1. 8–20.
- Yamamoto Tetsuo, Hasegawa Hiroichi.* Grain Formation through Nucleation Process in Astrophysical Environment // Progress of Theoretical Physics. 09 1977. 58, 3. 816–828.

- Yeh Sherry C. C., Matzner Christopher D. Ionization Parameter as a Diagnostic of Radiation and Wind Pressures in H II Regions and Starburst Galaxies // . X 2012. 757, 2. 108.
- Yin J., Matteucci F., Vladilo G. Chemical evolution of dwarf irregular and blue compact galaxies // . VII 2011. 531. A136.
- York Donald G., Adelman J., Anderson Jr. John E., Anderson Scott F., Annis James, Bahcall Neta A., Bakken J. A., Barkhouser Robert, Bastian Steven, Berman Eileen, Boroski William N., Bracker Steve, Briegel Charlie, Briggs John W., Brinkmann J., Brunner Robert, Burles Scott, Carey Larry, Carr Michael A., Castander Francisco J., Chen Bing, Colestock Patrick L., Connolly A. J., Crocker J. H., Csabai István, Czarapata Paul C., Davis John Eric, Doi Mamoru, Dombeck Tom, Eisenstein Daniel, Ellman Nancy, Elms Brian R., Evans Michael L., Fan Xiaohui, Federwitz Glenn R., Fiscelli Larry, Friedman Scott, Frieman Joshua A., Fukugita Masataka, Gillespie Bruce, Gunn James E., Gurbani Vijay K., de Haas Ernst, Haldeman Merle, Harris Frederick H., Hayes J., Heckman Timothy M., Hennessy G. S., Hindsley Robert B., Holm Scott, Holmgren Donald J., Huang Chi-hao, Hull Charles, Husby Don, Ichikawa Shin-Ichi, Ichikawa Takashi, Ivezić Željko, Kent Stephen, Kim Rita S. J., Kinney E., Klaene Mark, Kleinman A. N., Kleinman S., Knapp G. R., Korienek John, Kron Richard G., Kunszt Peter Z., Lamb D. Q., Lee B., Leger R. French, Limmongkol Siriluk, Lindenmeyer Carl, Long Daniel C., Loomis Craig, Loveday Jon, Lucinio Rich, Lupton Robert H., MacKinnon Bryan, Mannery Edward J., Mantsch P. M., Margon Bruce, McGehee Peregrine, McKay Timothy A., Meiksin Avery, Merelli Aronne, Monet David G., Munn Jeffrey A., Narayanan Vijay K., Nash Thomas, Neilsen Eric, Neswold Rich, Newberg Heidi Jo, Nichol R. C., Nicinski Tom, Nonino Mario, Okada Norio, Okamura Sadanori, Ostriker Jeremiah P., Owen Russell, Pauls A. George, Peoples John, Peterson R. L., Petravick Donald, Pier Jeffrey R., Pope Adrian, Pordes Ruth, Protopopescu Angela, Rechenmacher Ron, Quinn Thomas R., Richards Gordon T., Richmond Michael W., Rivetta Claudio H., Rockosi Constance M., Ruthmansdorfer Kurt, Sandford Dale, Schlegel David J., Schneider Donald P., Sekiguchi Maki, Sergey Gary, Shimasaku Kazuhiro, Siegmund Walter A., Smee Stephen, Smith J. Allyn, Snedden S., Stone R., Stoughton Chris, Strauss Michael A., Stubbs Christopher, SubbaRao Mark, Szalay Alexander S., Szapudi Istvan, Szokoly Gyula P., Thakar Anirudda R., Tremonti Christy, Tucker Douglas L., Uomoto Alan, Vanden Berk Dan, Vogeley Michael S., Waddell Patrick, Wang Shu-i., Watanabe Masaru, Weinberg David H., Yanny Brian, Yasuda Naoki, SDSS Collaboration . The Sloan Digital Sky Survey: Technical Summary // . IX 2000. 120, 3. 1579–1587.
- Zhang F., Li L., Cheng L., Wang L., Kang X., Zhuang Y., Han Z. Radiation fields of intermediate-age stellar populations with binaries as ionizing sources of H II regions. // . II 2015. 447. L21–L25.
- Zinchenko I. A., Dors O. L., Hägele G. F., Cardaci M. V., Krabbe A. C. Effective temperature of ionizing stars in extragalactic H II regions - II. Nebular parameter relationships based on CALIFA data // . II 2019. 483, 2. 1901–1911.
- Zurita A., Florido E., Bresolin F., Pérez-Montero E., Pérez I. Bar effect on gas-phase abundance gradients. I. Data sample and chemical abundances // . I 2021. 500, 2. 2359–2379.